



Max-Planck-Institut  
für Kolloid- und Grenzflächenforschung



---

# On structural properties of magnetosome chains

Dissertation

zur Erlangung des akademischen Grades  
doctor rerum naturalium  
(Dr. rer. nat.)  
in der Wissenschaftsdisziplin Theoretische Physik

eingereicht an der  
Mathematisch-Naturwissenschaftlichen Fakultät  
der Universität Potsdam

von  
Bahareh Kiani Alibagheri

Potsdam, den 31.01.2017

This work is licensed under a Creative Commons License:  
Attribution International  
To view a copy of this license visit  
<http://creativecommons.org/licenses/by/4.0/>

Published online at the  
Institutional Repository of the University of Potsdam:  
URN [urn:nbn:de:kobv:517-opus4-398849](http://nbn-resolving.de/urn:nbn:de:kobv:517-opus4-398849)  
<http://nbn-resolving.de/urn:nbn:de:kobv:517-opus4-398849>

*"The greatest achievement  
was at first and for a time  
a dream.*

*The oak sleeps in the acorn;  
the bird waits in the egg;  
and in the highest vision of the soul  
a waking angel stirs.*

*Dreams are  
the seedlings of  
reality."*

*James Allen*



## Zusammenfassung

Magnetotaktische Bakterien besitzen eine intrazelluläre Struktur, die Magnetosomenkette genannt wird. Magnetosomenketten enthalten Nanopartikel von Eisenkristallen, die von einer Membran umschlossen und entlang eines Zytoskelettfilaments ausgerichtet sind. Dank der Magnetosomenkette ist es magnetotaktischen Bakterien möglich sich in Magnetfeldern auszurichten und entlang magnetischer Feldlinien zu schwimmen. Die ausführliche Untersuchung der strukturellen Eigenschaften der Magnetosomenkette in magnetotaktischen Bakterien sind von grundlegendem wissenschaftlichen Interesse, weil sie Einblicke in die Anordnung des Zytoskeletts von Bakterien erlauben. In dieser Studie haben wir ein neues theoretisches Modell entwickelt, das sich dazu eignet, die strukturellen Eigenschaften der Magnetosomenketten in magnetotaktischen Bakterien zu erforschen.

Zuerst wenden wir uns der Biegesteifigkeit von Magnetosomenketten zu, die von zwei Faktoren beeinflusst wird: Die magnetische Wechselwirkung der Magnetosomenpartikel und der Biegesteifigkeit des Zytoskelettfilaments auf welchem die Magnetosome verankert sind. Unsere Analyse zeigt, dass sich die lineare Konfiguration von Magnetosomenpartikeln ohne die Stabilisierung durch das Zytoskelett zu einer ringförmigen Struktur biegen würde, die kein magnetisches Moment aufweist und daher nicht die Funktion eines Kompass in der zellulären Navigation einnehmen könnte. Wir schlussfolgern, dass das Zytoskelettfilament eine stabilisierende Wirkung auf die lineare Konfiguration hat und eine ringförmige Anordnung verhindert.

Wir untersuchen weiter die Gleichgewichtskonfiguration der Magnetosomenpartikel in einer linearen Kette und in einer geschlossenen ringförmigen Struktur. Dabei beobachteten wir ebenfalls, dass für eine stabile lineare Anordnung eine Bindung an ein Zytoskelettfilament notwendig ist. In einem externen magnetischen Feld wird die Stabilität der Magnetosomenketten durch die Dipol-Dipol-Wechselwirkung, über die Steifheit und die Bindungsenergie der Proteinstruktur, die die Partikel des Magnetosomen mit dem Filament verbinden, erreicht. Durch Beobachtungen während und nach der Behandlung einer Magnetosomenkette mit einem externen magnetischen Feld, lässt sich begründen, dass die Stabilisierung von Magnetosomenketten durch Zytoskelettfilamente über proteinhaltige Bindeglieder und die dynamischen Eigenschaften dieser Strukturen realisiert wird.

Abschließend wenden wir unser Modell bei der Untersuchung von ferromagnetischen Resonanz-Spektren von Magnetosomenketten in einzelnen Zellen von magnetotaktischen Bakterien an. Wir erforschen den Effekt der magnetokristallinen Anisotropie in ihrer dreifach-Symmetrie, die in ferromagnetischen Resonanz-Spektren beobachtet wurden und die Besonderheit von verschiedenen Spektren, die bei Mutanten dieser Bakterien auftreten.



# Abstract

Magnetotactic bacteria possess an intracellular structure called the magnetosome chain. Magnetosome chains contain nano-particles of iron crystals enclosed by a membrane and aligned on a cytoskeletal filament. Due to the presence of the magnetosome chains, magnetotactic bacteria are able to orient and swim along the magnetic field lines. A detailed study of structural properties of magnetosome chains in magnetotactic bacteria has primary scientific interests. It can provide more insight into the formation of the cytoskeleton in bacteria. In this thesis, we develop a new framework to study the structural properties of magnetosome chains in magnetotactic bacteria.

First, we address the bending stiffness of magnetosome chains resulting from two main contributions: the magnetic interactions of magnetosome particles and the bending stiffness of the cytoskeletal filament to which the magnetosomes are anchored. Our analysis indicates that the linear configuration of magnetosome particles without the stabilisation to the cytoskeleton may close to ring-like structures, with no net magnetic moment, which thus can not perform as a compass in cellular navigation. As a result we think that one of the roles of the filament is to stabilize the linear configuration against ring closure.

We then investigate the equilibrium configurations of magnetosome particles including linear chain and closed-ring structures. We notably observe that for the formation of a stable linear structure on the cytoskeletal filament, presence of a binding energy is needed. In the presence of external stimuli the stability of the magnetosome chain is due to the internal dipole-dipole interactions, the stiffness and the binding energy of the protein structure connecting the magnetosome particles to the filament. Our observations, during and after the treatment of the magnetosome chain with the external magnetic field substantiates the stabilisation of magnetosome chains to the cytoskeletal filament by proteinous linkers and the dynamic feature of these structures.

Finally, we employ our model to study the FMR spectra of magnetosome chains in a single cell of magnetotactic bacteria. We explore the effect of magnetocrystalline anisotropy in three-fold symmetry observed in FMR spectra and the peculiarity of different spectra arisen from different mutants of these bacteria.





# Contents

<b>1</b>	<b>Introduction</b>	<b>1</b>
1.1	Discovery of magnetotactic bacteria . . . . .	3
1.2	General characteristics of magnetotactic bacteria . . . . .	4
1.3	Detection and natural abundance of magnetotactic bacteria . . . . .	7
1.4	Magnetosomes . . . . .	10
1.5	Stability of magnetosome chain linear structure . . . . .	11
1.6	A model for magnetosome chains . . . . .	12
1.7	List of publications . . . . .	13
<b>2</b>	<b>Elastic properties of magnetosome chains</b>	<b>15</b>
2.1	Introduction . . . . .	15
2.2	A model for the elasticity of magnetosome chains . . . . .	16
2.3	Magnetic contribution to the elasticity . . . . .	18
2.3.1	Straight chain . . . . .	18
2.3.2	Bent chain . . . . .	19
2.3.3	Closed–ring configuration . . . . .	23
2.4	Including the filament . . . . .	25
2.5	Concluding remarks . . . . .	29
<b>3</b>	<b>A theoretical framework for magnetosome chains</b>	<b>31</b>
3.1	Introduction . . . . .	31
3.2	Models and methods . . . . .	32
3.2.1	Model . . . . .	32

3.2.2	Computer simulation . . . . .	34
3.3	Equilibrium configurations of magnetosome particles . . . . .	35
3.4	Probing magnetosome mechanics by rotating an external field . . . . .	39
3.4.1	Mechanical properties of the linkers . . . . .	39
3.4.2	Dynamics of rupture . . . . .	41
3.4.3	Recovery: Chain reassembly after disruption . . . . .	45
3.5	Concluding remarks . . . . .	47
<b>4</b>	<b>Application of the magnetosome chain model to FMR spectroscopy</b>	<b>51</b>
4.1	Introduction . . . . .	51
4.2	Models and methods . . . . .	54
4.2.1	Model . . . . .	54
4.2.2	Computer simulation . . . . .	55
4.2.3	Resonance spectrum . . . . .	56
4.3	Resonance field of magnetosome particles . . . . .	57
4.4	Magnetocrystalline anisotropy effect . . . . .	58
4.5	Effect of the magnetosome chain configuration on the resonance field	62
4.5.1	Linear magnetosome chain with defects . . . . .	63
4.5.2	A Cluster of magnetosome particles . . . . .	65
4.6	Concluding remarks . . . . .	65
<b>5</b>	<b>Summary, Conclusion and Outlook</b>	<b>69</b>
<b>A</b>	<b>supplementary discussions of chapter 2</b>	<b>73</b>
A.1	Derivations of the equations discussed in chapter 2 . . . . .	73
A.1.1	Straight chain energy . . . . .	73
A.1.2	Magnetic bending rigidity . . . . .	74
A.1.3	Nearest-neighbor Interactions . . . . .	78
A.1.4	Energy difference between linear chain and closed ring . . . . .	78
A.2	Effect of the temperature on the rigidity of magnetosome chains . . . . .	79

<b>B</b>	<b>Supplementary discussions of chapter 3</b>	<b>81</b>
B.1	Critical angle of rupture . . . . .	81
B.2	Magnetosome chains under weak external fields . . . . .	82
B.3	Dipole–dipole magnetic force . . . . .	83
B.4	Energy contributions in a magnetosome chain of greigite particles . .	85
<b>C</b>	<b>Supplementary discussions of chapter 4</b>	<b>87</b>
C.1	Derivatives of the total energy . . . . .	87
C.2	Resonance field at different orientations of the applied field . . . . .	88
C.3	Effect of dipole–dipole interactions on the resonance field . . . . .	89



# Abbreviations and Symbols

---

## Abbreviations

$\Delta mamj$  MAMJ protein deleted mutants of magnetotactic bacteria.

**FMR** Ferromagnetic Resonance.

**MMP** Many-Celled Magnetotactic Prokaryotes.

**MTB** Magnetotactic Bacteria.

**NS** North-Seeking Bacteria.

**OAI** Oxic–Anoxic Interface.

**OATZ** Oxic–Anoxic Transition Zone.

**SD** Single Magnetic Domain.

**SS** South-Seeking Bacteria.

## Symbols

$\mu_0$  Vacuum permeability,  $4\pi \times 10^{-7} \text{N A}^{-2}$ .

## Chapter 1

$d$  Gap distance between the magnetic particles, 10 nm.

- $\epsilon$  The dipole-dipole interaction of neighboring dipoles in the chain,  $\frac{\mu_0}{4\pi} \frac{2m^2}{l^3}$ .
- $E_{\text{fil}}$  Bending elasticity of the filament.
- $E_{\text{lin}}$  Equilibrium energy of a straight chain of magnetic dipoles.
- $E_{\text{magn}}$  Dipole-dipole interactions between the magnetic dipoles.
- $E_{\text{ring}}$  Equilibrium energy of a closed-ring of magnetic dipoles.
- $\kappa$  Total bending rigidity.
- $\kappa_{\text{fil}}$  Elastic bending rigidity.
- $\kappa_{\text{magn}}$  Magnetic bending rigidity.
- $l$  Distance between neighboring magnetosomes,  $2r + d$ .
- $\ell_{\text{p,magn}}$  Magnetic persistence length.
- $\mathbf{m}_i$  Dipole moment of magnetic dipole  $i$ .
- $r$  Magnetosome particle radius, 25 nm.
- $R$  Curvature radius of a bent chain of dipoles.

## Chapter 2

- $\mathbf{B}$  External magnetic field.
- $d$  Gap distance between the magnetic particles, 10 nm.
- $d_n$  Distance between neighbouring magnetosomes,  $d_n = 2R + d \simeq 50$  nm.
- $E_{\text{elasticity}}$  Elastic energy of the spring-like linkers.
- $E_{\text{b}}$  Binding energy,  $-2k_{\text{B}}T$ .

- $E_{bound}$  Bound configuration energy.
- $E_B$  External magnetic field–dipole interaction energy.
- $E_{dd}$  Dipole-dipole interaction energy.
- $E_{hc}$  Hard-sphere potential.
- $E_{unbound}$  Unbound configuration energy.
- $k_l$  Spring constant of the linkers,  $0.106 \text{ pNnm}^{-1}$ .
- $l$  Length of the linkers.
- $l_0$  Rest length of the linkers, 5 nm.
- $\mathbf{m}_i$  Dipole moment of magnetic dipole  $i$ .
- $R$  Magnetosome particle radius, 20 nm.

### Chapter 3

- $d$  Gap distance between the magnetic particles, 10 nm.
- $B_{res}$  Resonance field, External magnetic field at which resonance occurs.
- $E$  Total energy.
- $E_B$  External magnetic field–dipole interaction energy.
- $B_{ext}$  Applied field.
- $E_{crystal}$  Magnetocrystalline anisotropy energy.
- $E_{dd}$  Dipole–dipole interactions energy.
- $\gamma$  Gyromagnetic ratio,  $1.76 \times 10^{11} \text{ rad s}^{-1}\text{T}^{-1}$ .

$K_1$  First-order anisotropy constant,  $-1.1 \times 10^{+5} \text{Jm}^{-3}$ .

$R$  Magnetosome particle radius, 20 nm.

$\theta$  Polar angle.

$\varphi$  Azimuthal angle.

$\omega_{exp}$  Experimental resonance frequency,  $5.8936 \times 10^{+10} \frac{rad}{s}$ .

$\omega_i$  Resonance frequency of magnetosome particle  $i$ .

$\omega_{res}$  Analytical resonance frequency.



# Chapter 1

## Introduction

For decades, fundamental differences such as the absence of a cytoskeletal structure and the lack of membrane bound organelles resulted in bacteria to be considered less developed than eukaryotic cells with lower degree of sub-cellular compartmentalisation and domain specific functionality. Recent advances in biology of prokaryotes changed this traditional view dramatically. It was demonstrated that bacteria, like their eukaryotic counterparts, are actually highly organised and dynamic [1]. Until the early 1990s, it was believed that one fundamental difference between eukaryotes and bacteria is that bacteria do not have a cytoskeleton. But then a series of staggering discoveries overturned this view, identifying bacterial homologues of filamentous actin, tubulin and intermediate filaments that organise the eukaryotic cytoskeleton [2]. In addition to a dynamic cytoskeletal structure, it was also shown that remarkably some bacteria possess membrane bound organelles [3, 4].

Among the (few) bacteria with membranous organelles and cytoskeletal structure, are fascinating magnetotactic bacteria. These bacteria possess an intracellular structure called the magnetosome chain. Magnetosome chains contain nano-particles of iron crystals wrapped in a lipid bilayer membrane aligned by a network of cytoskeletal filaments mainly composed of a bacterial actin-like protein, called MamK [5]. The distinct properties of magnetotactic bacteria make them an ideal system for the study of bacterial cytoskeletal structure by means of both physics and biology.

In this thesis, we develop and apply a theoretical framework for the study of the struc-

ture of magnetosome chains. We start with an introduction on the discovery, general characteristics and structure of magnetotactic bacteria. The introductory chapter is followed by two chapters on the mechanical properties of magnetosome chains. In the first chapter, we address the bending stiffness of a magnetosome chain and we ask whether the bending stiffness is mostly caused by the cytoskeletal structure or by the magnetic interactions of magnetosome particles. In the second chapter, we develop a detailed model of magnetosome chains and explore the equilibrium configurations of magnetosome particles and investigate the sources stabilizing the magnetosome particles into stable linear arrangements on the cytoskeletal filament. Employing the model and the magnetic properties of magnetosome particles, we peer into the mechanical stability of magnetosome chain structure and analyse the chain responses to the mechanical stimuli. In the last chapter, we use our model equipped with parameters obtained from FMR spectroscopy experiments on magnetotactic bacteria to explore the resonance spectra of magnetosome chains in single cells of different strains and mutants. Understanding the behaviour of different spectra obtained from single cells of different mutants/strains can provide detailed information about the structure of magnetosome chains available in the sample. We explain that the narrow spectral linewidth is crucial for seeing structural features. In fact, the broad linewidth observed in FMR spectroscopy on bulk samples may not be able to provide us with fine details of the structure of the magnetosome chains. The potential of single cell FMR analysis to distinguish the structural differences suggests that the FMR spectroscopy could be used as an alternative tool to relate the spectrum with the structure of the magnetosome chain and ultimately to the strain/mutant, from which the spectrum was obtained meaning that we would be able to determine the strain available in the sample by FMR spectroscopy analysis.

## 1.1 Discovery of magnetotactic bacteria



Figure 1.1: *Aquaspirillum magnetotacticum* cell with one single chain of magnetite particles and one single flagellum at each pole of the cell. Scale bar represent  $1\mu\text{m}$ . Drawn after fig. 1(b) of [6].

Magnetotactic bacteria were first discovered in early 1970s by Richard P Blakemore. While studying microbial populations collected from the sediments of brackish marshes, he observed highly motile bacteria with swimming speed of the order of  $100\mu\text{m s}^{-1}$ . These bacteria were migrating persistently unidirectionally across the field of view and accumulating at one edge of the drop of the sediments. Despite exercising different controls over presumed stimuli of migration, the bacteria were swimming toward the same geographic direction, indicating the fact that the pervasive stimulus was possibly the Earth's magnetic field. That the behaviour of cells was truly magnetically directed was demonstrated by a magnet brought close to the microscope; astonishingly, the hundreds of swimming cells swerved in unison and swam toward the north pole of the magnet and conversely, by rotating the magnet, cells instantly turned and rushed away from the opposite end of the magnet [7, 8].

Blakemore's observation was not the first discovery of magnetotactic bacteria. In

1963, the observation of "magnetosensitivity" in aquatic bacteria has been documented by Salvatore Bellini while examining water samples for pathogens. But as not published in any peer-reviewed scientific journal, his discovery was never recognised till the latest discovery by Blakemore which introduced a whole new field of scientific study [9, 10]. The unexpected discovery has been proven to be a fruitful subject that crosses the established disciplines boundaries and requires thinking across them. Study of magnetotactic bacteria seems to have roused the collaborations and discussions among microbiologists, evolutionary biologists, biochemists, physicists and paleogeologist. It has been also offering thought-provoking possibilities for bionanotechnology applications.

## 1.2 General characteristics of magnetotactic bacteria

Magnetotactic bacteria are predominantly found at the oxic-anoxic interface (OAI) and the anoxic regions of water columns or sediments in natural aquatic habitats with layered concentration of chemical elements including oxygen, nitrogen and sulphur [11, 12]. Magnetotactic bacteria are not characterised as a new taxonomic classification, but are a diverse group of bacteria that show magnetotactic behaviour. Magnetotactic bacteria seem to use magnetotaxis in combination with chemotaxis in environments with chemical stratification along the magnetic field lines to find and maintain their preferred habitat. This reduces their random three-dimensional excursions to one dimension and presumably increases their efficiency in chemotaxis [13]. Despite all the similarities that those examined magnetotactic bacteria share, within the group they represent a copiousness of cellular morphologies including coccoid *Magnetococcus marinus* MC-1, *Desulfovibrio magneticus* RS-1, vibrioid marine *Magnetovibrio* MV-1, spirilloid *Magnetospirillum* species and even the multicellular many-celled magnetotactic prokaryotes (MMPs) [14, 13]. MMPs exhibit extraordinary morphotypes. They comprise 20 cells in a roughly spherical arrangement

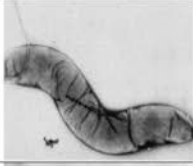

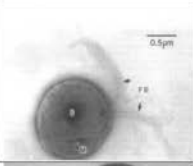
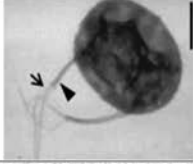
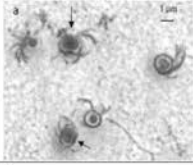
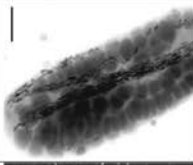
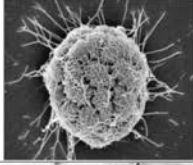
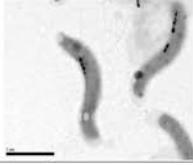
Strain	Cell morphology	Magnetosome mineral	Typical dimension of magnetosomes (nm)	Morphology of magnetosomes	Number of magnetosomes	Arrangement of magnetosomes	Arrangement of Flagella	Swimming velocity ( $\mu\text{m} \times \text{s}^{-1}$ )	
<i>Magnetospirillum gryphiswaldense</i> /MSR-1	Spirillum/ Spiral	Magnetite	30-50	Cuboctahedral	20-30	Single chain	Amphitrichous	10 - 30	
<i>Desulfovibrio magneticus</i> /RS-1	Vibrioid/ Rod-shaped	Magnetite	30-70	Tooth- or Bullet-shaped	5-15	Single chain	Monotrichous	10 - 30	
<i>Magnetococcus marinus</i> /MC-1	Coccus / Spherical	Magnetite	80-120	Truncated hexaoctahedral	10-15	Single chain	Peritrichous / Bilophotrichous	50 - 120	
Magneto-ovoid/MO-1	Ovoid	Magnetite	50-60	Elongated cubo- octahedral	15-25	Single chain	Peritrichous / Bilophotrichous	Up to 300	
<i>Magnetotactic cocci</i> (MC)/ARB-1	Coccus / Spherical to Ovoid	Magnetite	20-133	Hexagonal	10-30	Cluster, chain, or combination of both	Peritrichous / Bilophotrichous	1000	
<i>Magnetobacterium bavaricum</i>	Rod-shaped	Magnetite	110-150	Tooth- or Bullet- shaped	600-1000	Several parallel chains	Lophotrichous/ One polar tuft	40	
MMP	Spherical assemblies	Greigite/ Magnetite	85-90	Bullet-shaped or Equidimensional	300-1000	Several chains	Peritrichous	170	
<i>Magnetic vibrio</i> /MV-1	Vibrioid /Curved rod shape (comma shape)	Magnetite	40-60	Truncated hexaoctahedral	15	Single chain	Monotrichous	-	

Figure 1.2: General features of selected magnetotactic bacteria. Each species is designated with an image in front of its name.

with intercellular connections between outer membranes of smaller cells [15]. MMPs generally biomineralize crystals of iron sulphides. However, Lins et al., reported MMPs which mineralize either crystals of magnetite or together with greigite crystals



[16]. More examples on the morphology of magnetotactic bacteria are found in table 1.2. All magnetotactic bacteria studied to date possess flagella, usually positioned

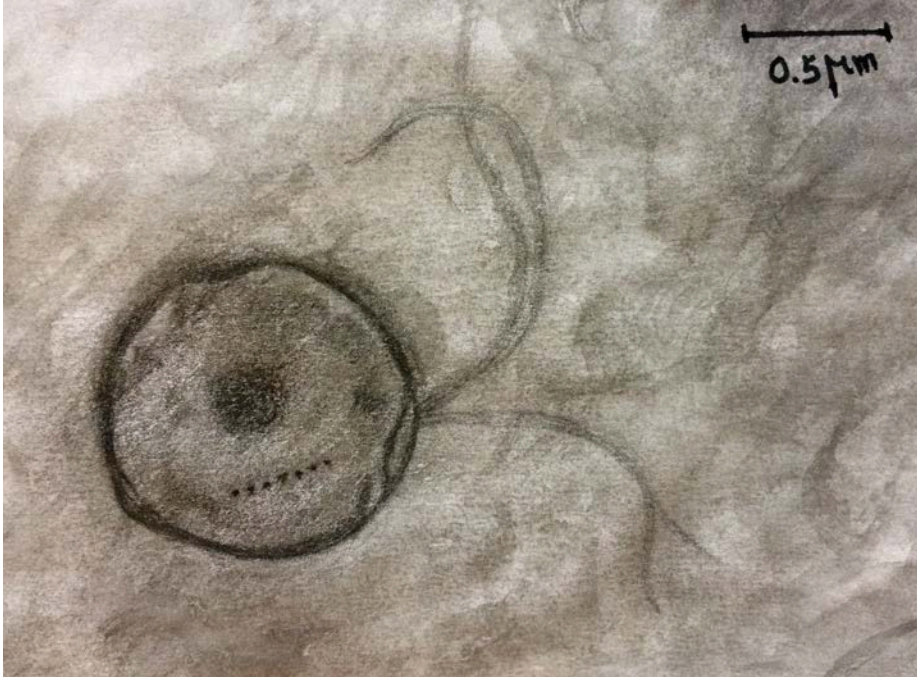


Figure 1.3: *Magnetococcus marinus* MC-1 with a single chain of magnetite particles and two tufts of flagella (bilophotrichous). Scale bar represents  $0.5 \mu\text{m}$ . Drawn after fig. 1(b) of [13].

at one side of the cell or at both poles. The arrangement of flagella varies between species/strains. In some cells it is monotrichous (a single flagellum at only one pole) as in coccoid cells with a single polar unsheathed flagellum [17]. In others, it can be either amphitrichous (single flagellum at both poles) as in curved, rod-shaped cells of *Magnetospirillum* with single bipolar flagella, or lophotrichous (a tuft of flagella at one pole) as in ovoid, rod-shaped cells of the marine Magneto-ovoid bacterium MO-1 with multiple sheathed flagella at one pole [18]. MMPs are peritrichously flagellated with asymmetrical distribution of flagella on each constituent cell, presumably reflecting a spatial distribution required for coordinated motility [19]. Cells of magnetotactic bacteria, like other flagellated organisms, swim by rotating their helical flagella. In addition, due to the presence of the magnetosome chains, they align with the local magnetic field lines, in natural environments the geomagnetic field lines. Swimming speeds vary among species and strains from  $20\text{-}65 \mu\text{m s}^{-1}$  in



Figure 1.4: *Magnetobacterium bavaricum* with several parallel chains of magnetite particles and one polar tuft of flagella. Scale bar represent 1  $\mu\text{m}$ . Drawn after fig. 1(b) of [20].

*M. gryphiswaldense* [21] to  $1000 \mu\text{m s}^{-1}$  in the coccus ARB-1 [22]. This is up to 500 times faster than *Escherichia coli* [23]. More examples of swimming speeds of different magnetotactic bacteria are found in table 1.2.

### 1.3 Detection and natural abundance of magnetotactic bacteria

Magnetotactic bacteria are ubiquitous, they have been found in a wide range of different aquatic habitats: in the Arctic, in Baltic Sea sediments, in South America (Brazil) [8, 24], Tasmania, in Australia and New Zealand [25], Germany [26], Mediterranean Sea, France [27] and throughout North America [7, 8, 28].



Figure 1.5: A bar magnet is placed close to the drop. The bacteria swim towards the magnet and accumulate at the edge of the drop.

Because of their magnetic behaviour, the bacteria can be easily collected from natural environments. Using their magnetically directed motility and applying a magnetic field, one can redirect them to swim out of the sediments and accumulate where they could be sampled. To detect bacteria in samples taken from muds and waters for further studies, light microscopy in combination with the standard hanging-drop technique are used [13, 29, 30, 18]: a drop of the sample is pipetted on a microscope slide placed on a rubber o-ring with the drop on the underside. A bar magnet is placed on the microscope stage near the drop. The magnetic axis is parallel to the plane of the slide and passes the drop radially. The bacteria will swim towards or away from the bar magnet to the edge of the drop close to the near pole of the bar magnet or to the other side of the drop to the edge farthest away from this pole and accumulate there. If the magnet is rotated by  $180^\circ$ , the bacteria will turn and swim in opposite direction, on the same axis relative to the external magnetic field lines. Another  $180^\circ$  rotation of the bar magnet will bring the bacteria back to the initial edge of the drop [18, 31]. In the absence of any experimental equipment and for samples with a high abundance of magnetotactic bacteria, one can easily detect the bacteria by bringing a bar magnet close to the bottle filled with the sample. A



small dark brown–gray accumulation consisting of MTB appears inside the sample bottle close to the magnet. The geomagnetic field is oriented in south–north direc-

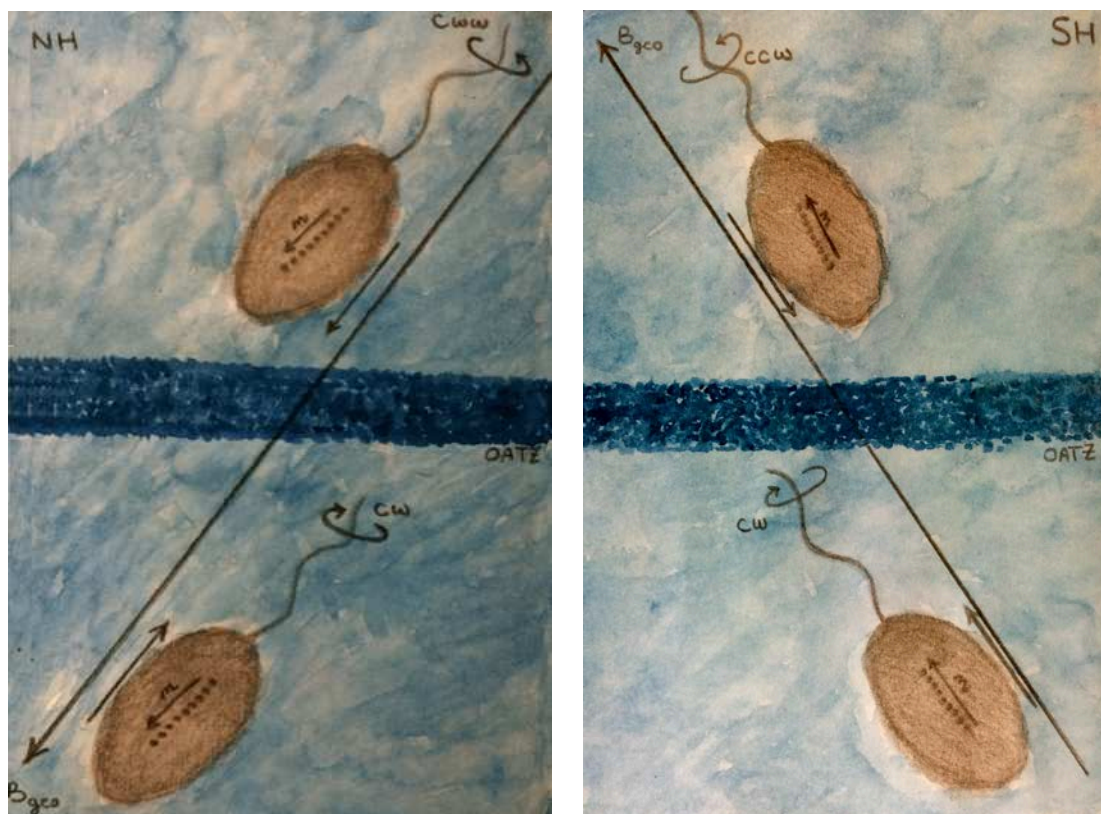


Figure 1.6: Schematic drawing of how polar magneto-aerotaxis directs cells to the preferred oxygen concentration at the oxo-anoxic interface (OATZ). NH, Northern hemisphere; SH, Southern hemisphere;  $B_{geo}$ , geomagnetic field.

tion. It also has a component normal to the surface of the globe, which is directed upward on the Southern Hemisphere, decreasing to a value of zero at the geomagnetic equator, and is inclined downward on the Northern Hemisphere, with a value increasing with latitude. Because of this inclination, bacteria found in the Northern Hemisphere swim downward toward the south magnetic pole and parallel to  $B$ . These Bacteria which swim parallel to  $B$  are called North-seeking (NS). Bacteria found in the Southern Hemisphere swim downward toward the north magnetic field and therefore antiparallel to  $B$ , South-seeking (SS) bacteria [17, 7, 8]. As a consequence of downward directed motion, which is an advantage for survival of these bacteria, in either hemisphere there is a prevalence of magnetotactic bacteria in sediments and

absence of them from surface waters. If the sole vertical component of the geomagnetic field selects the dominant cell polarity in nature then neither of the swimming polarities should exit at the geomagnetic equator at which the geomagnetic inclination is zero. However, Frankel et al., [24], reported the observation of magnetotactic bacteria in sediments at the equator and not in the surface waters, therefore there should be other chemotactic responses to oxygen which assists the bacteria in finding their right habitat.

## 1.4 Magnetosomes

One of the most striking features of magnetotactic bacteria is their capability to flawlessly produce and organise magnetosome crystals. Magnetosome chains, the unique organelles responsible for magnetic behaviour, are intracellular structures consisting of a well ordered linear structure [32] of single domain iron crystals [33, 34] enclosed by a lipid bilayer membrane [35], called the magnetosome vesicle. This vesicle is most likely an invagination of the cell membrane anchored by a proteinous linker to a network of cytoskeletal filaments [36]. It is also a compartment where highly controlled biomineralization of well ordered iron crystals proceeds [3]. The magnetosome iron crystals consist of magnetite ( $\text{Fe}_3\text{O}_4$ ) [37], greigite ( $\text{Fe}_3\text{S}_4$ ) or iron pyrite ( $\text{FeS}_2$ ) [38, 11]. The crystals are typically 35-120 nm long, within the stable, single-magnetic-domain (SD) size range [39, 40, 41], however, metastable, single-magnetic domain magnetosome crystals with length up to 250 nm were also observed [42, 43, 44]. In general, homogeneously magnetized single domain magnetosome particles have the maximal magnetic moment (per volume) because of the formation of magnetic domain walls in magnetic particles within the size range larger than SD size range and the effect of thermal fluctuations in particles within the size range smaller than SD size range. Therefore it seems that magnetotactic bacteria optimize their magnetic dipole by controlling the size of the magnetosome particles [45, 46]. Another example of the control over the magnetosome particles is the morphology of the crystals. Magnetosome crystal morphology varies between bacterial strains and species while remaining

consistent within each strain and species. Examples of different morphology include the most widespread cuboctahedral and equidimensional elongated crystals in *Magnetospirillum* species, truncated hexaoctahedral crystals in the magnetic vibrio and finally the tooth-shaped (bullet- or arrowhead-shaped) crystals found in *DesulfoVibrio magneticus* [31, 47].

In most magnetotactic bacteria, the magnetosomes are arranged in single or multiple chains. Magnetic interactions between the magnetosome particles in a chain orient their magnetic dipole moment parallel to each other and parallel to the axis of the chain. As a result, the magnitude of the total magnetic dipole moment of the cell is the sum of the permanent magnetic dipole moments of the individual magnetosome particles and the magnetosome chain functions as a single magnetic dipole. Studies of magnetotactic bacteria employing magnetic force microscopy [48] and electron holography [49] confirm this conclusion.

## 1.5 Stability of magnetosome chain linear structure

The linear arrangement of magnetic moments in the magnetosome chain maximizes the magnetic dipole of the cell. The simplest model for magnetotaxis assumes passive orientation of the swimming bacterium along the magnetic field lines due to the torque exerted by the field on the magnetic moment. Thermal energy, on the other hand, tends to disorient the bacterium during swimming. The magnetic moment of a chain of 20 magnetite particles with the length extension of 50 nm, similar to the magnetosome particles in the strain MSR-1, is  $6.02 \times 10^{-16} \text{ JT}^{-1}$ , using the magnetite magnetization per volume,  $0.48 \times 10^{+6} \text{ JT}^{-1} \text{ m}^{-3}$ . Since the magnetosome chain is fixed in the cell, this value is effectively the magnetic moment of the bacterium. Therefore the total magnetic energy of the cell in the geomagnetic field of  $50 \mu\text{T}$  is  $3.0 \times 10^{-20} \text{ J}$ . The time average of orientation of such a single dipole under thermal fluctuations, given by replacing the time average with ensemble average, is

$\langle \cos(\theta) \rangle = L(\frac{mB}{kT}) \simeq 0.9$ ,  $L(\frac{mB}{kT})$  is the Langevin function. This means, despite the thermal fluctuation, the magnetic interaction of the magnetosome chain with the geomagnetic field is enough to align the bacterium with the field [50, 46]. Recently, some evidence for much larger non-thermal noise in the environment has been reported. The observed effect may be explained by an effective temperature larger than the actual temperature [51, 52].

As discussed, the maximal magnetic moment in magnetotactic bacteria is due to the linear arrangement of the magnetic moments in the magnetosome chain. The linear arrangement of any system of magnetic nano particles has the maximum magnetic moment. However, this configuration is a metastable state and it may fold into a closed-ring structure or collapse into a cluster [53].

Along with the magnetosome chain, extends a network of cytoskeletal filaments composed of mainly the bacterial actin-like protein MamK [5]. Magnetotactic bacteria recruit these cytoskeletal filaments to, beside actively transporting the magnetosome particles, control the position of particles in the cell and therefore to maintain the cell magnetic orientation [54]. Further evidence of the stabilization of magnetosome particles to the filament by macromolecular complexes was recently shown in an in vivo experiment by Koernig et al., [55]. In their study, Koernig et al., examine the stability of magnetosome chains by causing structural changes in magnetosome chains of immobilized bacteria, using the magnetic interaction between magnetosome particles and an external magnetic field.

## 1.6 A model for magnetosome chains

In the course of this work, we develop a framework for the magnetosome chain structure that enables us to discuss the energetics, stability and mechanical properties of magnetosome chains.

Previously published works on systems of this type with the chain as either a chain of discrete particles or as continuous magnetic rod have some limitations. In most

of the discrete magnetosome chain models, the magnetostatic interactions between magnetic particles in their self-assembly [56] or in the fusion of two chains [53], have been discussed with no discussion on the elastic properties of the magnetosome chain. Elastic properties have been addressed by Scherbakov et al. In their study, the magnetosome chain is regarded as a long rod with interacting alternating elastic (organic substance) and non-elastic (magnetite particles) elements, far from the magnetosome chain structure that is known to date [57]. Continuous magnetic rod models are in part extensions of the Kirchhoff model of elastic rods by either including the orienting effect of the magnetic field on the filament or including permanent magnetic particles on the free end of an elastic cantilevered rod [58, 59]. The obtained bending rigidity in these models is without any correction due to the discrete distribution of magnetosome particles on the filament which is fixed at both its ends.

The presence of actin-like filaments, to which the particles are linked by organic linkers are known now. In addition, imaging reveals the connections between membranes of some of the magnetosome particles. Nevertheless, none of the aforementioned works is based on this current knowledge of magnetosome chain structure. At the same time, the discussion on the energetics of such a system is limited and recent progress in the field of magnetotactic bacteria focuses more on elucidating the microbiological aspects or biomineralization-biochemistry process in magnetotactic bacteria. As a result, there is a paucity of research that provides more information concerning the physics involved in the cytoskeletal structure of magnetotactic bacteria.

Our theoretical model for magnetosome chains takes into account all the mentioned issues that influence the equilibrium configurations, stability and mechanical properties of magnetosome chains.

## 1.7 List of publications

Part of the research carried out in the course of this thesis was published in the following articles:

- Bahareh Kiani, Damien Faivre, Stefan Klumpp (2017) A theoretical framework for

magnetosome chains structure, Manuscript in preparation

- Sara Ghaisari, Bahareh Kiani, Stefan Klumpp, Damien Faivre (2017) Study of resonance spectra in magnetosome chains, Manuscript in preparation
- B. Kiani, D. Faivre, and S. Klumpp, *New J. Phys.* 17 (2015).
- S. Klumpp, B. Kiani, P. Vach, and D. Faivre, *Phys. Scr.* T165 (2015).

# Chapter 2

## Elastic properties of magnetosome chains

1

### 2.1 Introduction

All magnetotactic bacteria contain single or multiple magnetosome chains and in the majority of them, magnetosome chains are organised into linear structures. The linear arrangement of magnetosome chains ensures the maximal magnetic moment of the chain and the maximal torque exerted by the earth magnetic field on the chain. Otherwise stated, the linear arrangement of magnetosome particles optimises the orientation of the cells and their migration along the field. Consequently, the linear arrangement of the magnetic particles in magnetotactic bacteria is crucial as it provides a sufficiently large magnetic moment for navigation of the cells.

However, in general chains of magnetic nanoparticles are typically rather fragile and may collapse into folded chains, closed–ring structures or clusters. In magnetotactic bacteria, it is suggested that along with the dynamic roles of the cytoskeletal filament in assembling and positioning the magnetosome particles [54, 60], the cytoskeletal fil-

---

<sup>1</sup>This chapter is an extended version of the results published in the following article: B. Kiani, D. Faivre, and S. Klumpp, *New J. Phys.* 17 (2015).

ament provides further stabilisation of the linear structure of magnetic particles, [5], which goes beyond the stabilising effect of magnetic interactions between magnetosome particles [55].

In this chapter, we address a related problem, namely the bending stiffness of magnetosome chains. We specifically ask whether the bending stiffness is mostly due to the cytoskeletal structure or to the magnetic interactions, as magnetic particles are known to form linear structures [53, 57] without a stabilizing filament and (short) chains have been seen in cells lacking the MamK protein [61, 62]. To that end, we consider a model of (permanent) magnetic dipoles fixed on a semiflexible filament. We calculate the magnetic contribution to the bending rigidity and the persistence length and compare it with the contribution due to the filament. For chains of magnetic particles, it is also known that magnetic particles form closed ring structures, so called flux-closure rings [63, 64, 65], thus we consider whether an actin-like semiflexible filament can stabilize a linear chain of magnetosomes against ring formation either thermodynamically or kinetically.

## 2.2 A model for the elasticity of magnetosome chains

To investigate the flexibility of a magnetosome chain, we describe it as a chain of permanent magnetic dipoles fixed along a semiflexible filament (Fig. 2.1). This magnetic and elastic energy is given by the dipole-dipole interactions between the magnetic dipoles and the bending elasticity of the filament,

$$E = E_{\text{magn}} + E_{\text{fil}}. \quad (2.1)$$

The magnetic contribution to the energy is given by

$$E_{\text{magn}} = - \sum_{i=1}^N \sum_{j>i}^N \frac{\mu_0}{4\pi} \frac{1}{r_{ij}^3} \left( \frac{3(\mathbf{m}_i \cdot \mathbf{r}_{ij})(\mathbf{m}_j \cdot \mathbf{r}_{ij})}{r_{ij}^2} - \mathbf{m}_i \cdot \mathbf{m}_j \right), \quad (2.2)$$



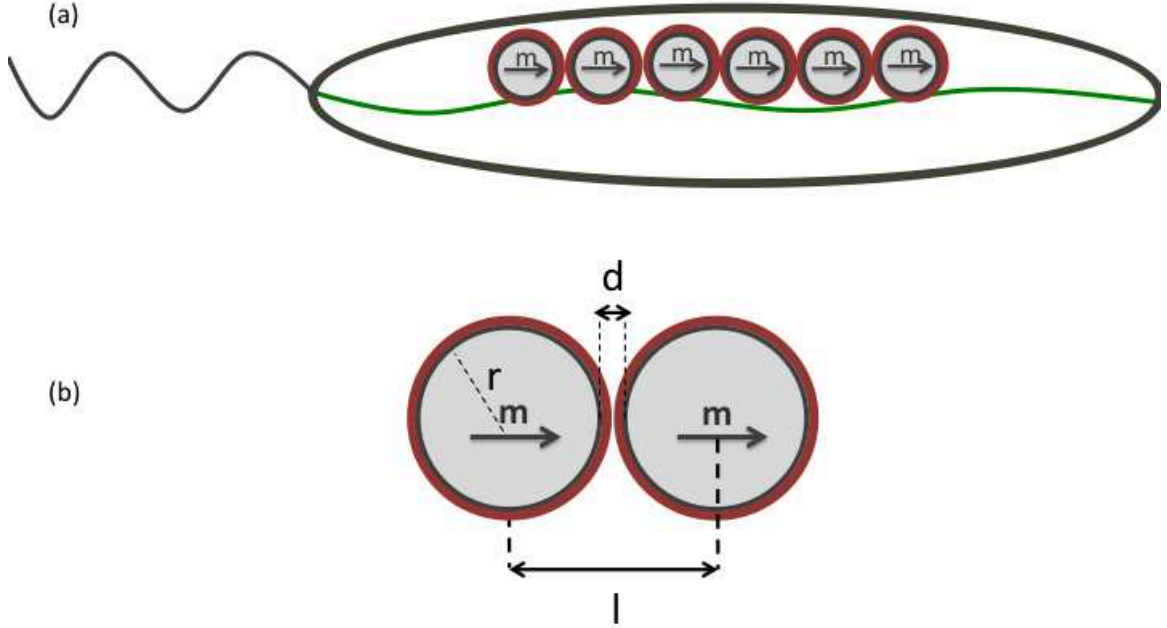


Figure 2.1: a) Sketch of the magnetosome chain in magnetotactic bacterium: magnetic nanoparticles (gray circles) are attached to a cytoskeletal filament (green line), enveloped in membrane (red lines). b) Geometric parameters of magnetosome particles with radius  $r$  and magnetic moment  $\mathbf{m}$ .

where  $\mu_0 = 4\pi \times 10^{-7} \text{N A}^{-2}$  is the vacuum permeability, the  $\mathbf{m}_i$  are the dipole moments of magnetic dipoles and the  $\mathbf{r}_{ij}$  are the distance vectors between them, with  $r_{ij} = |\mathbf{r}_{ij}|$ . In the following, we will assume that all dipoles have equal absolute value,  $|\mathbf{m}_i| = m$ . We will also take the distance between nearest neighbor dipoles as constant,  $r_{i,i+1} = l$ , due to either the stiffness of the filament or due to steric constraints such as touching magnetosomes (Fig. 2.1(b)). We want to emphasize that mature magnetosomes are in the single-domain regime, i.e. they have permanent magnetic dipoles with rather large magnetization due to the absence of magnetic domains [66]. As a consequence, our model is considerably simpler than models for chains of superparamagnetic particles [67, 68], where the magnetization and thus the magnetic interactions depend on the external field experienced by the particle.

The elastic properties of the filament are described by a bending energy which is a quadratic function of the local curvature [69],

$$E_{\text{fil}} = \frac{\kappa_{\text{fil}}}{2} \int_0^{L_{\text{fil}}} \left( \frac{\partial \mathbf{t}}{\partial s} \right)^2 ds. \quad (2.3)$$

Here  $s$  is a coordinate along the contour of the filament,  $\mathbf{t}(s)$  is the unit vector along the tangent of the filament, and  $\kappa_{\text{fil}}$  is the bending rigidity.  $L_{\text{fil}}$  is the filament length, which we take to be equal to  $L_{\text{fil}} = Nl$ .

## 2.3 Magnetic contribution to the elasticity

In this section, we consider the magnetic part of the energy function given by Eq. (3.3) separately, i.e. we omit the elastic contribution due to the filament and determine the sole contribution of the magnetic interactions to the elasticity of the chain.

### 2.3.1 Straight chain

We start by briefly considering the limiting case of a linear chain of magnetic dipoles. In the equilibrium state of such a chain, the dipoles orient parallel to each other and to the chain axis, thus the magnetic interaction energy is

$$E_{\text{lin}} = - \sum_{i=1}^N \sum_{j>i}^N \frac{\mu_0}{4\pi} \frac{2m^2}{r_{ij}^3} = -N\epsilon \sum_{n=1}^{N-1} \frac{(1 - \frac{n}{N})}{n^3}. \quad (2.4)$$

In the last expression, we have introduced a characteristic energy scale  $\epsilon = \frac{\mu_0}{4\pi} \frac{2m^2}{l^3}$ , which represents the dipole–dipole interaction of neighboring dipoles in the chain. Nearest neighbor interactions alone (given by the first term of the sum, with  $n = 1$ ) lead to  $E_{\text{lin}} = -N\epsilon(1 - 1/N)$ . Due to the rapid decay ( $\sim r^{-3}$ ) of the magnetic interactions, these nearest neighbor interactions dominate the total energy. Indeed, for long chains ( $N \rightarrow \infty$ ), the sum can be evaluated in terms of Riemann’s zeta function as  $\sum_{n=1}^{\infty} n^{-3} = \zeta(3) \simeq 1.2$ , thus one finds that the full energy is only 20 percent larger than the nearest–neighbor contributions alone. We note that the parameter  $\epsilon$  is related to the dipolar coupling parameter  $\lambda$  defined in earlier work [53] via  $2\lambda = \epsilon/k_B T$  with the thermal energy  $k_B T$ , provided that the distance  $l$  is the minimal distance (i.e. when the magnetic particles or their non–magnetic coating touch each other).

Next, we give an estimate of the characteristic energy  $\epsilon$ . For magnetite nanoparticles, the saturation magnetization (per volume) is  $0.48 \times 10^6 \text{ Jm}^{-3} \text{ T}^{-1}$  [47]. For a particle of radius  $r = 25 \text{ nm}$ , a typical value for magnetosomes in the well studied *Magnetospirilla* species [70], the magnetic moment is thus  $m = 3.14 \times 10^{-17} \text{ JT}^{-1}$ . The distance between neighboring magnetosomes can be estimated as  $l = 2r + d \simeq 60 \text{ nm}$ , where  $d \simeq 10 \text{ nm}$  is a gap distance between the magnetic particles accounting for the surrounding membranes. The characteristic energy  $\epsilon$  is then estimated as  $\epsilon \simeq 9.14 \times 10^{-19} \text{ J} = 221k_B T$ . This implies that the energy of a chain of 20 magnetosomes is  $\simeq -2.0 \times 10^{-17} \text{ J}$  or  $-4900k_B T$ .

### 2.3.2 Bent chain

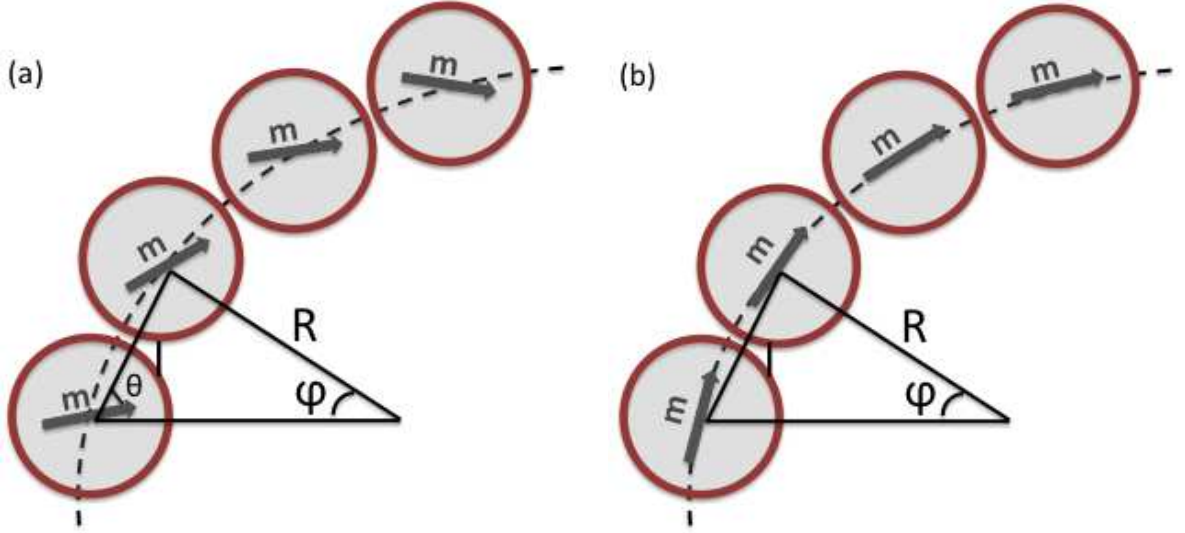


Figure 2.2: Bent magnetosome chain: (a) Sketch of the geometry: The chain is bent onto a circle with radius  $R$  and a corresponding bending angle  $\varphi$ . The magnetic moments are oriented in an angle  $\theta$  with respect to the line connecting neighboring magnetosomes. (b) In the equilibrium configuration,  $\theta = -\varphi/2$ , i.e., the magnetic moments align tangentially on the bending circle.

Next, we consider a bent chain and determine its bending rigidity and the corresponding persistence length. To that end, we consider a chain of dipoles on a (planar) circle with radius  $R$ . Thus two neighboring dipoles span a sector of the circle characterized by the bending angle  $\varphi = 2 \arcsin(\frac{l}{2R})$ .

In addition to the assumption of equal magnetic moments, we now also assume that all dipoles have the same orientation with respect to the distance vector connecting them to their neighbor and characterize their orientation by the angle  $\theta$  (Fig. 2.2). Since the magnetostatic interactions are short-ranged and dominated by the nearest-neighbor interactions, this assumption can be expected to be quite accurate except for the dipoles at the two ends of the chain. Minimization of the interaction energy with respect to  $\theta$  leads to a tangential orientation of the magnetic moments,  $\theta = -\varphi/2$ . Energy minimization is detailed in Appendix A.1.2.

The magnetic bending energy and thus the persistence lengths are obtained from a Taylor expansion of the energy in powers of  $l/R$ , i.e., for small curvature, which is described in the Appendix A.1.2 and A.1.3. This calculation is similar to the calculation of the electrostatic persistence length of a polyelectrolyte [71]. If only nearest neighbor interactions are included, the Taylor expansion leads to

$$E^{\text{nn}} \approx -N\epsilon \left(1 - \frac{1}{N}\right) + \frac{1}{8}N\epsilon \left(1 - \frac{1}{N}\right) \left(\frac{l}{R}\right)^2. \quad (2.5)$$

Here the first term is the linear chain energy and the second term represents the contribution from bending with a magnetic bending rigidity of

$$\kappa_{\text{magn}}^{\text{nn}} = \frac{\epsilon l}{4} \left(1 - \frac{1}{N}\right). \quad (2.6)$$

The same calculation can be done when including all magnetic interactions, see the Appendix A.1.2. In this case, we obtain the magnetic bending rigidity as

$$\kappa_{\text{magn}} = \frac{\epsilon l}{4} \sum_{n=1}^{N-1} \frac{\left(1 - \frac{n}{N}\right)}{n^3} \approx \frac{\epsilon l}{4} \zeta(3) \simeq 0.3\epsilon l. \quad (2.7)$$

As the sum in this expression is the same as in the expression for the energy of a linear chain, the bending energy is also dominated by the nearest neighbor interactions, with all other interactions contributing about 20 percent to the bending energy. We notice that our expression for the bending rigidity differs slightly,  $\simeq 14\%$ , from a result

reported in a recent study [72]. The two results show the same scaling behavior ( $\kappa_{\text{magn}} \sim \epsilon l$ , but different numerical prefactors,  $\zeta(3)/4 \simeq 0.30$  and  $(\zeta(3) + 1/6)/4 \simeq 0.34$ ). In that study, the bending rigidity was derived from the energy difference between a straight chain and a closed ring. We will therefore come back to that discrepancy in the next section, where we discuss the closed ring configuration.

Using a relation from polymer theory for semiflexible polymers [73], the bending rigidity can be converted into a persistence length,

$$\ell_{\text{p,magn}} = \frac{\kappa_{\text{magn}}}{kT} = \frac{\epsilon l}{4kT} \sum_{n=1}^{N-1} \frac{(1 - \frac{n}{N})}{n^3}. \quad (2.8)$$

This parameter characterizes the length scale over which such a chain is straight under the influence of thermal fluctuations. Thus for the chain of magnetosomes considered above, we obtain a bending rigidity of  $1.5 \times 10^{-20} \text{ J } \mu\text{m}$  or  $3.7k_B T \mu\text{m}$ . The corresponding magnetic persistence length at room temperature is  $3.7 \mu\text{m}$ , which is comparable to the cell size (and longer than the typical chain length). Thus even due to the magnetic interactions alone, magnetosome chains in magnetotactic bacteria can be expected to be essentially straight. We note however that several studies have shown that the alignment of magnetotactic bacteria in external fields is subject to non-thermal fluctuations described by a substantially higher effective temperature [52, 51], likely induced by the motility of the cells. If bending of the magnetosome chain is subject to similar fluctuations, the thermal persistence length may overestimate the length over which magnetosome chains are straight in cells.

The magnetic energy scale  $\epsilon$  is strongly dependent on the particle size, at least for particles in the single-domain size range (15-120 nm for magnetite [74]), where the magnetization is directly proportional to the volume and thus  $\epsilon \sim r^6/(2r + d)^3$ . As a consequence, the magnetic persistence length also increases strongly with particle size, as plotted in Fig. 2.3. We have plotted two cases in this figure: The circles are for magnetite particles that touch each other without gaps ( $d = 0$ ), i.e. the distance between nearest neighbors is  $l = 2r$ . For the squares, we have taken the gap size  $d = 10 \text{ nm}$  as constant to account for the presence of the magnetosome membrane

around the magnetic particles. For example, a doubling of the particle size, compared to the case considered above, leads to an increase of the magnetic persistence length to  $65 \mu\text{m}$ . Particles of such size are found in some magnetotactic bacteria including in extraordinarily large cell of *Magnetobacterium bavaricum* (cell size  $\sim 10 \mu\text{m}$  and particles size 110-140 nm)[20]. On the other end of the size spectrum, for small magnetosomes with radius 15-20 nm, persistence length is about  $1 \mu\text{m}$ , which is comparable with the chain length.

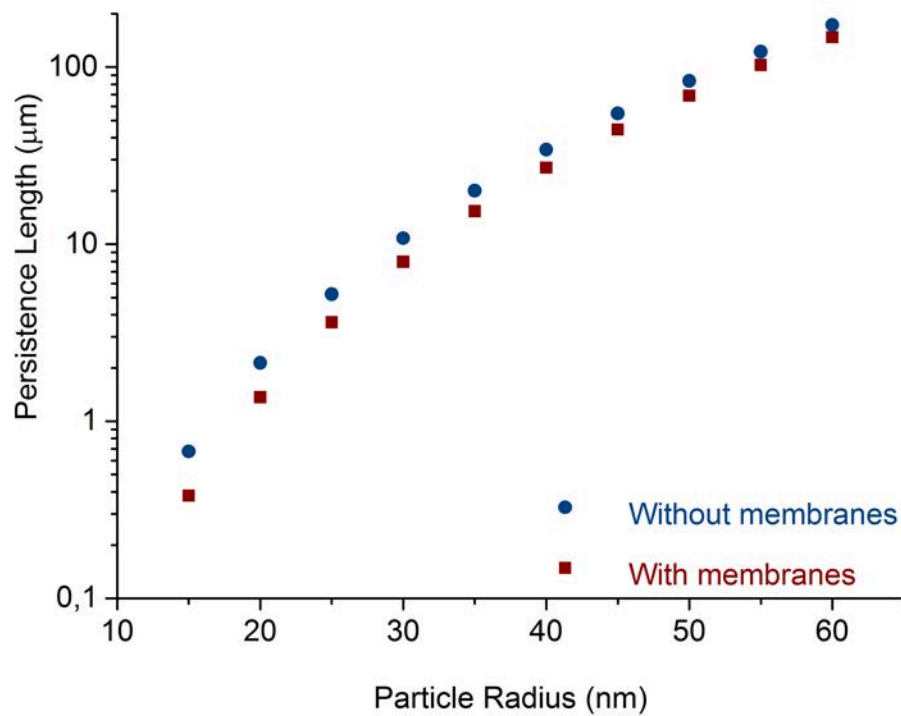


Figure 2.3: Persistence length as a function of particle size: Values are calculated for a magnetosome chain of 20 spherical magnetite particles at minimal distances ( $\ell = 2r + d$ ) with or without an enclosing membrane. Squares are for the case with a membrane of thickness 5 nm ( $d = 10\text{nm}$ ), circles for the case without a membrane ( $d = 0$ ).

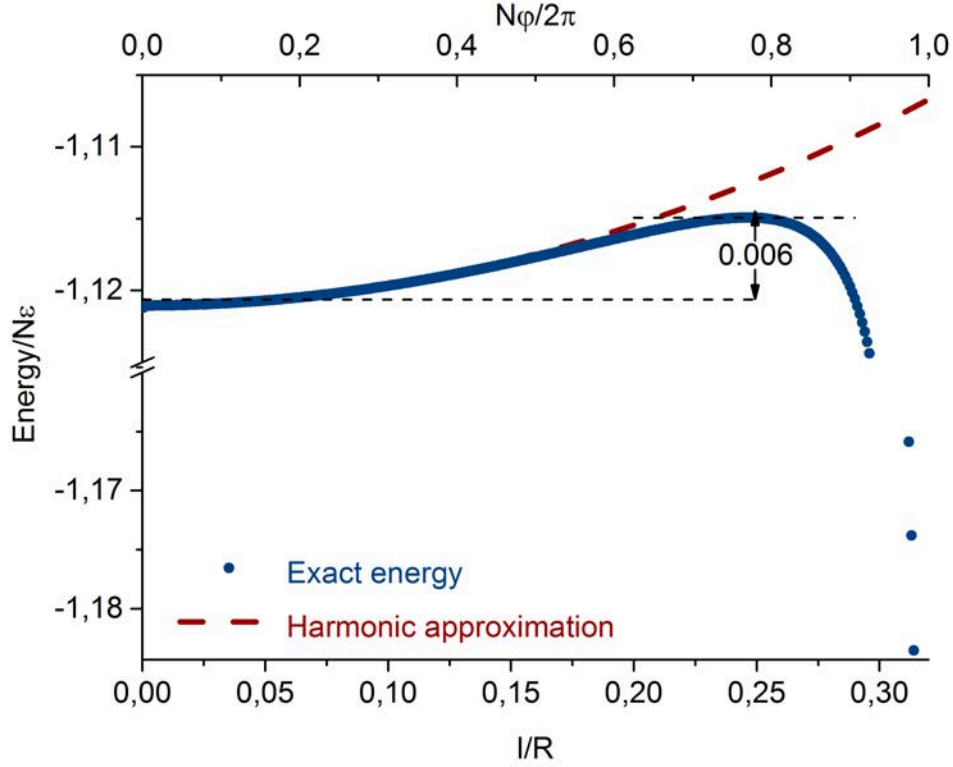


Figure 2.4: Magnetic energy of a chain as a function of the bending curvature given by the inverse of the ratio of the distance between nearest neighbors and the curvature radius ( $l/R$ ) or equivalently, the curvature angle  $\varphi$  (normalized to the angle for the closed ring configuration). The larger circle at the highest curvature shown indicates the closed ring configuration. The dashed line indicates the harmonic approximation, the arrows marks the barrier between the linear and close–ring configuration. The results shown here are for a chain of 20 particles.

### 2.3.3 Closed–ring configuration

Fig. 2.4 shows the full expression for energy as well as the harmonic approximation given by Eq. (A.8), as a function of chain curvature. Good agreement is seen for small curvatures, but for large  $l/R$ , the energy decreases again. In fact, the linear chain is not the configuration corresponding to the global energy minimum. The global energy minimum is found for a closed–ring configuration (also know as flux closure ring [75]), which has the maximal curvature possible. Assuming that the distance between neighboring magnetic dipoles is defined by steric constraints on the magnetosomes that the dipoles represent, the distance between the first and last

particle (i.e. the dipoles with  $i = 1$  and  $i = N$ ) in the ring configuration will be  $l$ , i.e. the same as the distance of nearest neighbors in the interior of the chain. Thus, the closed ring is a configuration with the maximal bending angle  $\varphi = 2\pi/N$ , see Fig. 2.5 (larger angles would result in overlap of the first and last particle), and its equilibrium energy is given by

$$E_{\text{ring}} = - N\epsilon \sum_{n=1}^{N-1} \frac{(1 - \frac{n}{N})}{4 \left( \frac{\sin(n\pi/N)}{\sin(\pi/N)} \right)^3} \left( 3 + \cos \frac{2\pi n}{N} \right). \quad (2.9)$$

That the closed ring is energetically favorable can be seen by the following estimate: The closed ring is stabilized by the additional nearest neighbor interaction between the first and last particle, which can be estimated as  $\epsilon$ , but needs to overcome the bending energy,  $\sim \epsilon/(8N) \times (Nl/R)^2 \sim \epsilon\pi^2/(2N)$ . Thus, for sufficiently large  $N$  the interaction between the dipoles with  $i = 1$  and  $i = N$  overcompensates the effect of bending. This crude estimate indicates that the closed ring is the minimal energy configuration for chains of 5 or more particles, while a comparison of the exact energies for the linear chain and the closed ring (plotted in Fig. 2.5) shows that this is true for chains with 4 or more particles, as has already been shown in several earlier studies [76, 77, 78, 53, 79]. We also note that the closed ring configuration with tangential orientation of the magnetization has been demonstrated experimentally using electron holography for cobalt nanoparticles [80]. For large  $N$ , the energy difference between straight chain and closed ring is small, as it decays as

$$E_{\text{ring}} - E_{\text{lin}} \approx -\frac{\pi^2\epsilon}{2N} \sum_{n=1}^{N-1} \frac{1 - \frac{n}{N}}{n}, \quad (2.10)$$

For detail calculation, see Appendix A.1.4. These considerations show that the relative stability of the straight chain and closed ring configuration depends not only on bending, but also on the additional interaction energies due to bringing the ends of the chain together. In a finite straight chain, the outermost particles contribute less to the total interaction energy than the particles in the chain interior, because of the smaller number of nearest neighbors, next nearest neighbors etc. In the recent



paper by Vella et al. [72], the bending rigidity was calculated by identifying the bending energy with the energy difference between a closed ring of  $N$  particles and a straight chain of the same length, embedded within an infinitely long chain (and thus without finite size corrections to the energy). The rationale for this approach is that embedding has the same effect on the energy as ring closure and that in this way the contributions due to bending and due to ring closure can be separated. This approach is exact for the dominant nearest neighbor interactions, and a good approximation for the full set of interactions. As mentioned, it leads to the same scaling behavior of the bending rigidity, but a slightly higher numerical prefactor. We note that, as the energy difference between ring and embedded chain reflects only bending and not ring closure, it cannot be used to determine the relative stability of these structures.

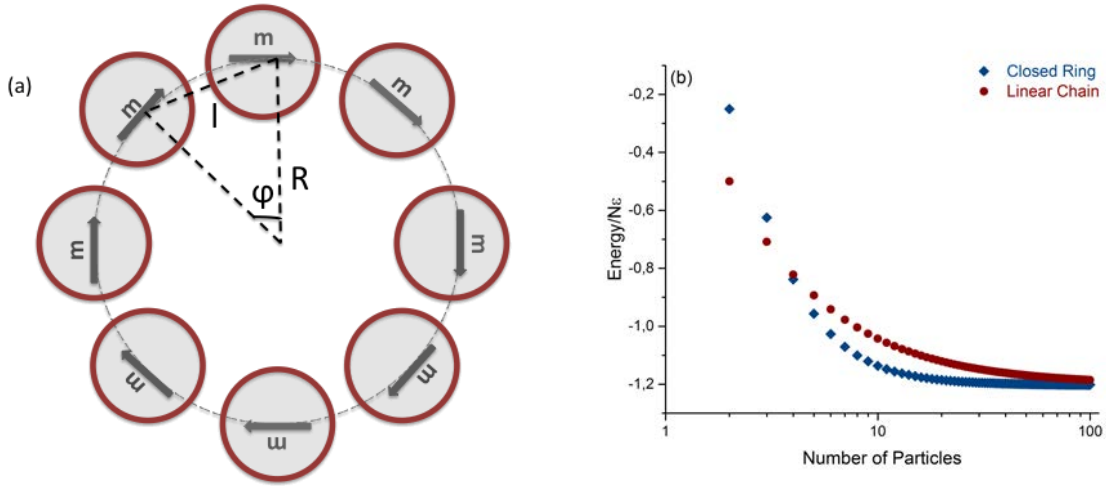


Figure 2.5: Linear and closed ring configurations of a chain of magnetic nanoparticles interacting only magnetically (no filament): (a) Sketch of the closed ring geometry. (b) Magnetic energy for the linear and the closed–ring configurations as functions of the number of particles. The closed ring configuration has lower energy for chains with four and more particles.

## 2.4 Including the filament

Now we include the elasticity of the filament and consider the full model with the energy given by Eq. (3.2). For the magnetosome chain on a circle with radius  $R$ ,

we can write the filament bending energy as  $E_{\text{fil}} = \kappa_{\text{fil}} Nl / (2R^2)$ . The total bending rigidity is obtained as the sum of the magnetic and elastic contributions,

$$\kappa = \kappa_{\text{magn}} + \kappa_{\text{fil}}. \quad (2.11)$$

Likewise the persistence length of the magnetosome chain is also obtained by summing the two contributions,  $\ell_p = \ell_{p,\text{magn}} + \ell_{p,\text{fil}}$ , and is thus essentially determined by the larger contribution. Above, we have estimated the magnetic persistence length for a typical magnetosome chain to be in the range of a few microns, with a strong dependence on particle sizes. The persistence length of a MamK filament is not known, but since MamK is a homolog of actin, we can compare this value with the persistence length of actin filaments, which has been measured to be 15-17  $\mu\text{m}$  [81, 82, 83]. If we take this value as an estimate for the persistence lengths of the MamK filament, we can conclude that both contributions to the bending rigidity are of the same order of magnitude, but the filament contribution is the dominant one with  $\kappa_{\text{fil}}/\kappa_{\text{magn}} \simeq 3\text{--}5$ . However, this estimate is subject to some uncertainty, as the magnetosome filament may be a bundle of MamK filaments rather than a single filament and the details of its structure are unknown. Filament bundles can have even higher bending rigidities and persistence lengths; for example up to 100-fold larger bending rigidities have been reported for actin bundles, depending on the number of filaments in a bundle and the type of crosslinker [84]. Likewise, due to the strong dependence of the magnetic contribution part on size, the magnetic bending rigidity could be dominant in species with large particles.

As mentioned before, for chains with more than four magnetic particles the closed-ring configuration is more stable than a straight chain. Ring closure, however, does not confer any energetic advantage to the filament, only the cost due to bending, so the presence of the filament can be expected to stabilize the linear chain against ring closure. We thus ask, whether the bending rigidity of an actin-like filament is sufficient to stabilize a linear magnetosome chain either thermodynamically, by making the linear configuration the global energy minimum, or kinetically, by increasing the

energy barrier between the linear and the ring configuration. Fig. 2.6(a) shows the total energy of the magnetosome chain as a function of curvature for different values of  $\kappa_{\text{fil}}$ . One can see that both the energy of the closed ring and the height increase as the bending rigidity of the filament is increased. The dashed line on top shows the case, where  $\kappa_{\text{fil}}$  is chosen such that the energy of the straight chain and of the closed ring are the same. This critical value  $\kappa_{\text{fil}}^*$  is given by

$$\kappa_{\text{fil}}^* = \frac{l\epsilon}{4 \sin^2(\pi/N)} \left( \frac{\sin^3(\pi/N)}{2} \sum_{n=1}^{N-1} \frac{1 - \frac{n}{N}}{\sin^3(n\pi/N)} (3 + \cos(2\pi \frac{n}{N})) - 2 \sum_{n=1}^{N-1} \frac{1 - \frac{n}{N}}{n^3} \right) \quad (2.12)$$

For a chain of 20 magnetosomes, this condition is met for  $\kappa_{\text{fil}}^*/\kappa_{\text{magn}} \simeq 4.68$ . Calculating this critical value of  $\kappa_{\text{fil}}$  for different numbers of particles allows us to determine a morphological diagram as a function of the ratio of bending rigidities  $\kappa_{\text{fil}}/\kappa_{\text{magn}}$  and the particle number. This diagram (Fig. 2.6(b)) exhibits two regimes, one in which the ring configuration is the globally most stable one and another where the straight chain is the most stable configuration. Not surprisingly, an increasing  $\kappa_{\text{fil}}$  extends the linear chain region.

Assuming a bending rigidity of the filament similar to a single actin filament will bring the system close to the transition, but typically the closed ring will still be the most stable configuration (for  $\kappa_{\text{fil}}/\kappa_{\text{magn}} \simeq 4$  and  $N \simeq 20$ ). Thus, a bending rigidity only slightly higher than actin's (about 1.6-fold) or a small bundle of a few actin-like filament would stabilize the straight chain thermodynamically, i.e. making it the globally stable configuration. However, even lower values of the filament stiffness than for a single actin filament may have an important impact in the cell, as they are sufficient to destabilize small rings. Within the spatial confinement of the cell, small rings and clusters containing small rings may be the dominant competing assemblies as the confinement makes large rings are rather unlikely.

In addition, a ratio of the bending rigidities of  $\kappa_{\text{fil}}/\kappa_{\text{magn}} \simeq 4$  leads to an increase in the barrier height of almost an order of magnitude (Fig. 2.6(a)), so that even lower filament bending rigidities should be sufficient to stabilize the linear configuration kinetically. In the cell, additional stabilization is provided by the confinement due to

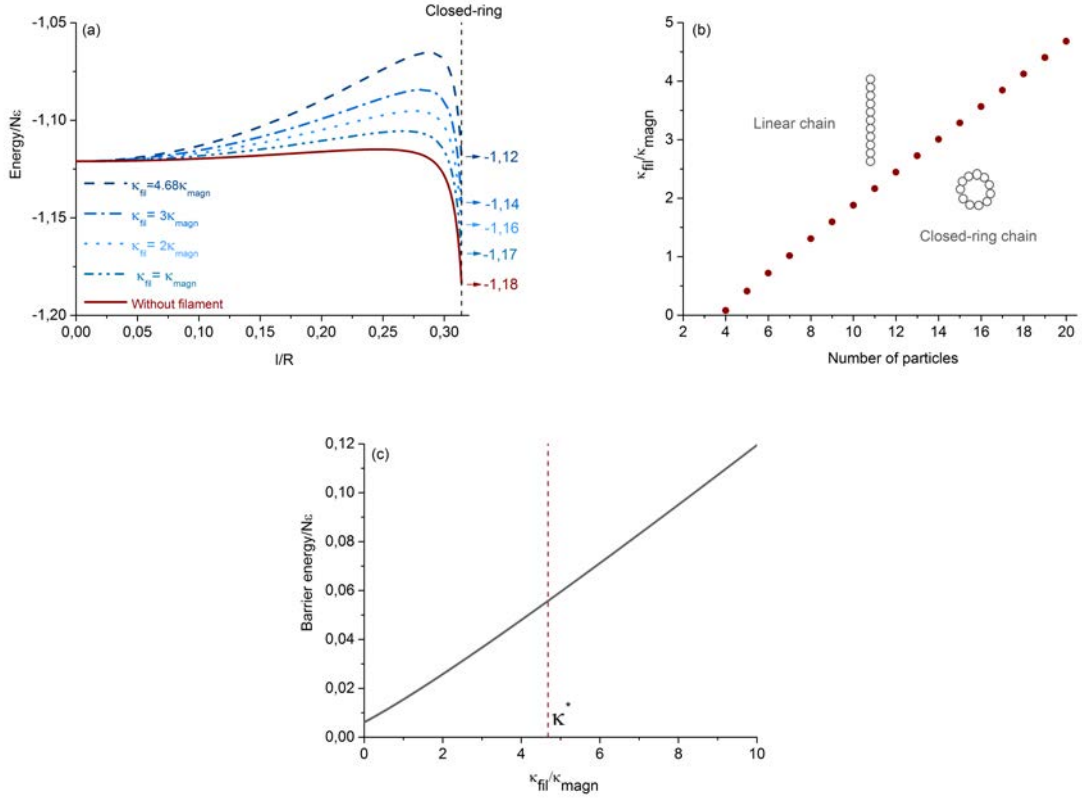


Figure 2.6: Bending of a magnetosome chain: (a) Magnetic and elastic bending energy as a function of the curvature  $\ell/R$  for different values of the filament bending stiffness  $\kappa_{fil}$ . The uppermost curve is for the critical value of  $\kappa_{fil}$ , for which the linear and the closed–ring configuration have the same energy. (b) State diagram indicating the lowest–energy configuration as a function of the ratio of the elastic and magnetic bending rigidities,  $\kappa_{fil}/\kappa_{magn}$ , and the number of magnetic particles. (c) Height of the energy barrier separating the linear–chain and closed–ring configuration as a function of the ratio of the bending rigidities. The vertical red line indicates the critical bending rigidity,  $\kappa_{fil}^*$ , above which the linear chain is the most stable configuration.

the cell’s membrane, which will prevent large ring structures.

To summarize these considerations, Fig. 2.7 shows three possible structures of the magnetosome filament, a single filament spanning the whole cell, a bundle of filaments individually spanning the whole cell, and a bundle of shorter filaments. In the first case, the filament stabilizes the linear chain kinetically by increasing the barrier to ring closure, but most likely, the closed ring is still the configuration with the globally lowest energy. In the second case, the linear chain corresponds to the global energy minimum, and the third case remains somewhat unclear. As thermodynamic

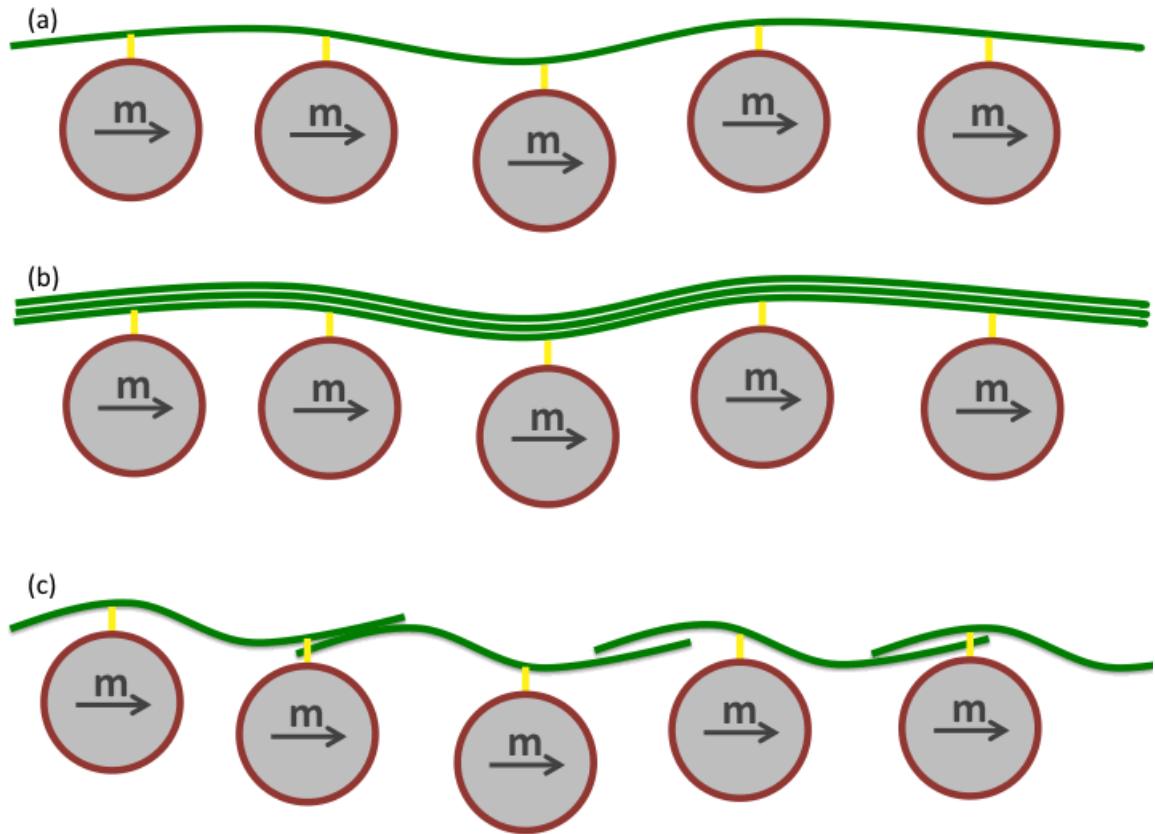


Figure 2.7: Schematic picture for possible structures of magnetosome filaments: a) A single long filament extending from one cell pole to the other, b) a bundle of long filaments, c) a long bundle consisting of shorter filaments.

stabilization requires a filament stiffness only 1.6–fold larger than actin’s, such a bundle may be strong enough if the bundle consists of at least two filaments along its full length. On the other hand, such a structure may be locally less stiff and thus be prone to bending at specific points.

## 2.5 Concluding remarks

In this chapter, we have address the bending stiffness of magnetosome chains, which results from two main contributions, a magnetic one due to the magnetic interactions between magnetosomes that favor straight chain orientation, and an elastic contribution due to the bending stiffness of the actin–like cytoskeletal filament to which

the magnetosomes are attached. Our analysis shows that while both contributions are relevant, the bending stiffness of the filament can usually be expected to be the dominant part, with an about 4-fold longer persistence length than due to magnetic interactions alone. However, even the magnetic interactions alone can be expected to result in a straight chain, as the persistence length exceeds the chain length. This conclusion should however be taken with the caveat that it relies on the assumption of thermal fluctuations of the magnetosome chain, while at least for the alignment of the bacteria in external fields there is some evidence for non-thermal fluctuations, as the alignment could be described by an elevated effective temperature [51, 52]. More importantly, for a chain of magnetic particles without a stabilizing filament, the linear configuration is not the configuration of lowest energy. Rather such a chain can be closed to a ring configuration, as seen experimentally [53]. Such rings have lower energy than straight chains for chains of 4 or more particles, so one can imagine them forming even despite the confinement in an elongated cell which should provide some stabilization to the linear configuration. Of course, closure of a ring is detrimental for the function of the chain, as the ring has no net magnetic moment. As a result of our analysis, we think that one of the roles of the filament is to stabilize the linear configuration against ring closure. That such stabilization is needed is suggested by observations of clusters of magnetosomes in mutants lacking the MamJ protein that links the magnetosomes to the filament (the situation is less clear for mutants lacking the filament protein MamK, as these cells exhibit multiple short linear chains). For a single actin-like filament, such stabilization is likely kinetic, i.e. by the increase of the barrier between the straight and ring configurations. For small bundles of such filaments, we expect the stabilization to be thermodynamic, i.e., in these cases, the linear configuration corresponds to the global energy minimum. Unfortunately, the finer internal structure of the magnetosome filament remains to be resolved and it also remains a possibility that some aspects of chain stability are different in different species of magnetotactic bacteria.

# Chapter 3

## A theoretical framework for magnetosome chains

### 3.1 Introduction

In eukaryotic cells, the cytoskeleton provides the cell with stiffness and structure and it is a key player in organising the cellular component during cell division [85]. It is no exception in magnetotactic bacteria with the cytoskeleton being at the helm of structuring the magnetosome chain and reorganising it, while duplicated, during cell division in emerging daughter cells. As an example, we showed in chapter 2, how the cytoskeleton filament in magnetotactic bacteria stabilises the chain against ring closure which is detrimental for the function of the cell. In other words, how the mechanics and structure of the cytoskeleton in magnetotactic bacteria is tied to the functionality of the magnetosome chain in these bacteria. Moreover, as discussed in the last chapter, in the case of magnetotactic bacteria, along with the cytoskeleton, the internal dipole–dipole interactions are also stabilising the magnetosome chain structure. This stabilisation of the magnetosome chain upon the cytoskeleton structure has been long a source of curiosity. In a study, Koernig et al., investigated the magnetosome chain stabilisation in magnetotactic bacteria *in vivo*. They use the magnetic properties of the magnetosomes to apply a force on the linkers of the par-

ticles to the filament in the immobilised living bacteria [55].

In this chapter, we develop and apply a framework for the study of the structure of magnetosome chains. Our model includes the magnetostatic interactions between magnetosome particles which are enclosed in a membrane and are allowed for binding to the cytoskeletal filament. We also take into consideration the presence of an external magnetic field as an external stimulus which acts upon the magnetic particles. In the first part of this chapter, we explore the equilibrium configurations of magnetosome particles and investigate whether the assembly of magnetosome particles into stable linear arrangements is due to the dipole–dipole interactions between particles or to the presence of the binding potential between membrane of magnetosome particles and the cytoskeletal filament which anchors the particles to the filament. In the second part, we employ the magnetic properties of magnetosome particles to study the mechanical stability of the magnetosome chains. We gain more insight into the chain’s responses to the mechanical stimuli and try to understand the dynamics of chain rupture seen in the aforementioned work [55]. In the last part of this chapter, we give close attention to the activity of magnetosome chain after rupture and explore its dynamic constitution.

## 3.2 Models and methods

### 3.2.1 Model

In our modelling approach, the magnetosome chain is described by a linear chain of  $N$  spherical magnetic particles which are connected to a rigid filament by elastic connections. The magnetic nano–particles are taken to consist of magnetite with the saturation magnetisation (per volume) at room temperature of  $0.48 \times 10^6 \text{ Jm}^{-3} \text{ T}^{-1}$  [47]. For a particle of radius  $R = 20 \text{ nm}$ , a typical value for magnetosomes in the well studied *Magnetospirilla* species [70], the magnetic moment is thus  $m = 1.61 \times 10^{-17} \text{ JT}^{-1}$ . Magnetosome particles in this size domain are in the single–domain regime, i.e. they have permanent magnetic dipoles with rather a large magnetisation due to the



absence of magnetic domains [66]. The distance between neighbouring magnetosomes can be estimated as  $d_n = 2R + d \simeq 50$  nm, where  $d \simeq 10$  nm is a gap distance between the magnetic particles accounting for the surrounding membranes. Two particles  $i$  and  $j$  interact through the potential

$$E = E_{\text{dd}} + E_{\text{hc}}, \quad (3.1)$$

where  $E_{\text{hc}}$  is the hard-sphere potential given by

$$E_{\text{hc}} = \begin{cases} 0 & \text{if } r_{ij} \geq d_n, \\ \infty & \text{if } r_{ij} < d_n. \end{cases} \quad (3.2)$$

where  $r_{ij}$  is the inter-particle distance.  $E_{\text{dd}}$  is the dipole-dipole interaction, defined as follows:

$$E_{\text{dd}} = -\frac{\mu_0}{4\pi} \frac{1}{r_{ij}^3} \left( \frac{3(\mathbf{m}_i \cdot \mathbf{r}_{ij})(\mathbf{m}_j \cdot \mathbf{r}_{ij})}{r_{ij}^2} - \mathbf{m}_i \cdot \mathbf{m}_j \right), \quad (3.3)$$

where  $\mu_0 = 4\pi \times 10^{-7} \text{NA}^{-2}$  is the vacuum permeability, the  $\mathbf{m}_i$  and  $\mathbf{m}_j$  are the magnetic moments of the dipoles and the  $\mathbf{r}_{ij}$  are the distance vectors between them, with  $r_{ij} = |\mathbf{r}_{ij}|$ . In the following, we will assume that all dipoles have equal absolute value,  $|\mathbf{m}_i| = m$ . They are linked to the filament through cable-like, semi-linear springs with elastic energy

$$E_{\text{elasticity}} = \begin{cases} +\frac{1}{2}k_l(l - l_0)^2 & \text{if } l > l_0, \\ 0 & \text{if } l \leq l_0. \end{cases} \quad (3.4)$$

The rest length  $l_0$  is taken to be 5 nm throughout this work and the spring constant is set to  $k_l = 0.106 \text{ pNnm}^{-1}$ . In addition, the linkers have a discrete degree of freedom indicating their bound or unbound state. At any position in the cell, particles can thus be in two states, bound to the filament or unbound. Switching to the bound state, a particle gains a negative binding energy  $E_b$  (with a default value of  $-2k_B T$ ) plus the (typically positive) elastic energy of the cable at length  $l$ , given by the distance of the particle surface to the filament. And finally,  $l$  is the distance between the

attachment points of the linker on the surface of the particle and on the filament. In addition, the magnetosome particles may interact with an external magnetic field,  $\mathbf{B}$ , with interaction energy

$$\begin{aligned}
 E_B &= - \sum_{i=1}^{i=N} \mathbf{m}_i \cdot \mathbf{B} \\
 &= - \sum_{i=1}^{i=N} mB \cos(\theta_B - \theta_i),
 \end{aligned}
 \tag{3.5}$$

where the second expression is valid for a field under an angle  $\theta_B$  with the axis of the magnetosome chain.

### 3.2.2 Computer simulation

We carry out Monte Carlo simulation for  $N = 20$  magnetosome particles in a cylindrical simulation box, in which the filament extends along the main axis of the cylinder. At every time step of the simulation, we perform a Monte Carlo move for a randomly chosen magnetosome particle. Three types of moves are possible: a spatial move, a change in orientation of its magnetic moment or a change in its attachment state (bound to unbound or vice versa). The moves are accepted according to a Metropolis criterion [86].

The spatial movements of magnetosome particles are performed by changing the position of magnetosome particles with a random vector whose  $x$ ,  $y$ ,  $z$  components attain random values between  $-d_n$  to  $d_n$ . To simulate the magnetic moment, we attribute to each magnetosome particle a vector with the fixed absolute value  $m$  and an orientation which undergoes random polar and azimuthal changes between  $-5$  and  $5$  degrees. We assume that the dipole moment of a magnetosome has a fixed orientation with respect to the inner coordinate system of the particle, any change in the orientation of the dipole causes a rotation of the corresponding particle.

### 3.3 Equilibrium configurations of magnetosome particles

We first consider magnetic particles in the absence of an external magnetic field. We start with the case where magnetosome particles are randomly distributed and particles are not allowed to bind to the cytoskeletal filament, similar to the case of  $\Delta mamJ$  mutants. One of the difficulties in the simulation of self-assembly of magnetic particles is the fact that the structures that are formed are located in the local minima of the energy landscape and once these structures are formed, the breaking of their magnetic bonds becomes very unlikely, which prevents the finding of the global minimum structure. This problem is most cumbersome when we are looking for structures at low temperature for which the thermal fluctuations are several orders of magnitude weaker than the magnetic interactions (in our case, typically 1000-fold) so that at this temperature a structure in the local minimum could become frozen. To overcome this difficulty, we apply simulated annealing, a simulation method in which, starting from a large value, the temperature is slowly reduced during the course of a simulation in order to reach the global minimum [87]. Simulated annealing is not guaranteed to converge to the exact minimum of the energy and if we want to extend the algorithm to finite temperature different runs will give different results [88], but it can be used to overcome the problem of frozen structures. At the same time, by moving the system into and out of different regions of the phase space, more diverse configurations are sampled, increasing the probability of finding the true minimum. We apply simulated annealing to systems of 20 magnetosome particles, initially randomly distributed in the simulation box without a magnetic field and without binding to the filament. The local minima found in this way exhibit a variety of structures, such as linear chains, closed rings and handle like structures, as shown in Fig. 3.1(a–f). Among those, chains and rings are the most common structures found in our simulations. A transition between these two types of structures is characterised by an interplay between the energetic gain of closing the rings, the energetic cost of chain bending

[89] and the higher entropy of the linear structures (a minor contribution because of the low temperature). However, the energy difference between the two structures is rather small. Our results suggest that the handle like structures are a combination of a linear chain and a ring sharing one of the particles at the end of the linear chain. Other combinations such as two chains or a chain and a ring are also found (Fig. 3.1).

To quantify the frequency of the different structures, we performed 100 runs of the Monte Carlo simulation with simulated annealing. The results are shown in Fig. 3.2 and confirm the predominance of the formation of chain and ring structures with nearly the same frequencies while handle-like structures cover only 3% of the structures observed.

Somewhat surprisingly, we do not obtain random clusters of magnetosomes, as seen for the  $\Delta mamJ$  mutant [36]. It is possible that these clusters form because of a combination of magnetic interactions and direct contact interactions between the membranes (or mediated by proteins in the membranes). Indeed, our simulations show cluster when such additional interactions are included.

Now we take the binding of particles to the filament into account. In that case, we predominantly obtain one single linear chain of magnetosome particles formed along the filament with magnetic moments in the direction of the chain. Some representative examples are shown in Fig. 3.1(f–h). We quantify the frequency of the different structures in Fig. 3.2 for different values of the particle–filament binding energy. Chains and rings are found to be the dominant structures formed. With increasing binding energy, more chains (up to about 2/3 of the cases) and fewer rings are observed. For the highest binding energies we simulated,  $E_b = 8.0k_B T$  and  $E_b = 16.0k_B T$ , all the ring and handle-like structures are assembled around the filament. In the case of  $E_b = 16.0k_B T$ , these structures are typically formed by two antiparallel chains which are bound to two sides of the filament and converge at their ends into a ring or handle-like structure.

Next, we consider the effect of an external magnetic field. If the external field has a non-zero angle relative to the direction of the filament, alignment of the dipoles with the field competes with the alignment with other dipoles bound to the filament. The

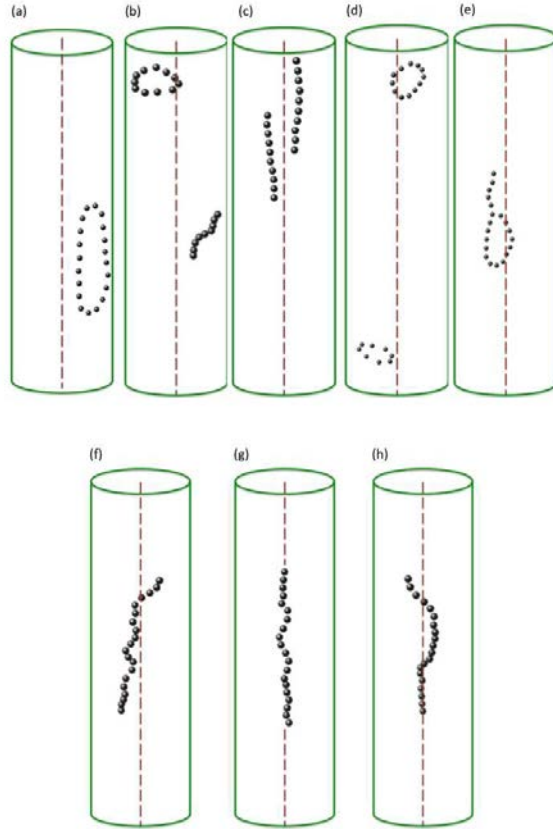


Figure 3.1: Local minimum structures observed in the Monte Carlo computer simulation of 20 randomly distributed magnetosome particles with no binding energy to the filament (a–e). Observed structures include chains (b, c), rings (a, b and d) and handle (e). In the presence of the binding energy to the filament, particles form semi-linear structures along the filament (f–h).

binding energy favours configurations with all particles close to the filament, while the external magnetic field–dipole interaction favours alignment of the magnetic dipoles with the external field, rotating them and increasing their elastic energy. For strong fields or strong magnetic interactions, one may even expect chains of particles in the direction of the field and detached from the filament. Thus, dependent on the strength and angle of the external field, and on the binding energy and stiffness of the linkers, the magnetosomes will adopt new configurations. In fact, we mostly observed configurations with multiple chains that are tilted away from the filament in the direction of the field but are attached to the filament via their middle particles.

Focusing on the competition between the binding energy and the external field,

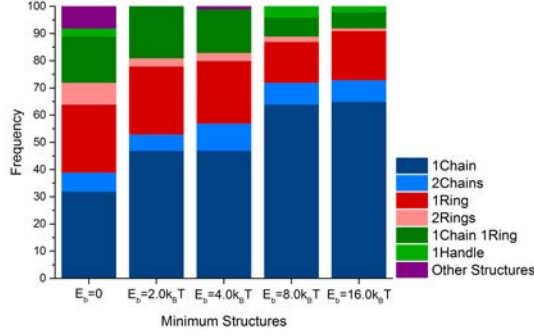


Figure 3.2: Fraction of configurations observed in the Monte Carlo computer simulations in the absence and presence of different values of the binding potential to the filament.

In each case configurations were extracted from 100 runs of the simulations. Simulations classified as Other structures include open rings (observed in the case of  $E_b = 0k_B T$ ) and a single ring accompanied by two chains (in the case of  $E_b = 4.0k_B T$ ).

we performed systematic Monte Carlo simulations for different values of the binding energy and the external magnetic field strength under a fixed angle of  $90^\circ$  relative to the direction of the filament. For each combination of the binding energy and the external magnetic field strength, we measured the number of chains formed and the number of magnetosome particles that are bound to the filament. The results of these simulations are presented in Fig. 3.3. For low external field ( $B = 1$  mT) we typically observe a single chain. The average number of bound particles (that connect the chain to the filament) increases with increasing binding energy to the point that for  $E_b = 16k_B T$  all the particles of the chain are bound to the filament. For the opposite limit of the high external field ( $B = 125$  mT), we always observe multiple chains, oriented in the direction of the field and either not attached to the filament or attached via particle(s) in the middle of the chains, depending on the binding energy. The latter configuration reflects a competition between several energy contributions: The presence of multiple chains is favored by the additional binding energy of their middle particles to the filament and the alignment of the magnetic moments with the external field, but a single chain configuration is favoured by the additional nearest neighbour interactions ( $\simeq 100k_B T$ ). In fact, parallel magnetic moments of the chains (in the multiple chain configuration) result in repulsive interactions be-

tween chains and build an energy barrier between two configurations which stabilises the multiple chain configuration kinetically. For weaker external fields, The nearest neighbor interactions become dominant over the alignment with the field, resulting in the formation of the single chain configuration. At the same time, it is less difficult to disorient the parallel magnetic moments resulting in a lower energy barrier to single chain formation.

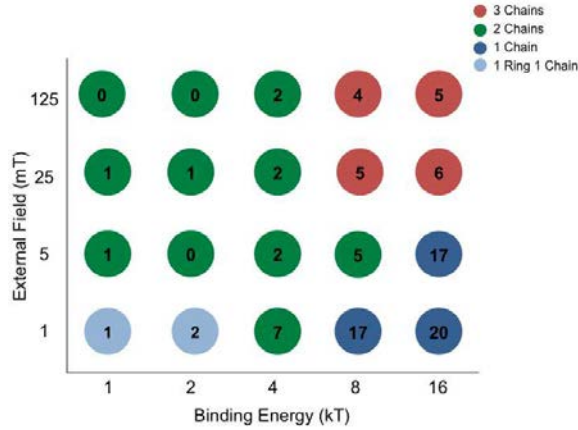


Figure 3.3: Final configuration of magnetosome particles for different values of the binding energy to the filament and the external magnetic field strength. The external field is fixed to an angle  $90^\circ$ , relative to the direction of the filament. The color coding indicates the magnetosome configuration quantified by the number of chains (average of 5 simulations, rounded to integers). The number in each circle indicates the number of particles bound to the filament (also averaged over 5 simulations and rounded to integers.)

## 3.4 Probing magnetosome mechanics by rotating an external field

### 3.4.1 Mechanical properties of the linkers

The mechanical stability of the magnetosome chain was probed in living magnetotactic bacteria by Koernig et al. [55] using a magnetic field rotated away from the chain axis. The experiment was done at the population level showing the average behaviour

of a large number of cells. With our simulations, we can perform the corresponding *in silico* probe for individual magnetosome chains. Thus we consider a magnetosome chain in an external magnetic field at an angle  $\theta_B$  relative to the direction of the filament. This angle is rotated from  $0^\circ$  to  $90^\circ$  about an axis perpendicular to the plane of the magnetosome chain. By rotating the magnetosome chain, an external field at a non-zero angle with respect to the direction of the filament exerts a mechanical force on the linkers of the particles to the filament. This is illustrated in Fig. 3.4 for the case of two magnetosomes. Considering this simple scenario, we can obtain an estimate for the critical angle at which magnetosomes are pulled away from the filament and the links break. To that end, we compare the energy of one unbinding particle in the bound and unbound configuration as indicated in Fig. 3.4 (the other particle is considered as a provider of the dipole-dipole interactions). In the bound configuration, the energy is given by

$$E_{bound} = E_B + E_{dd} + E_{elasticity} + E_{binding}. \quad (3.6)$$

After unbinding the energy includes only the external magnetic field-dipole and dipole-dipole interactions,

$$E_{unbound} = E_{dd} + E_B. \quad (3.7)$$

We take the two magnetic moments to be parallel and aligned with the field and calculate both energies. Assuming that the linker breaks, when the bound energy exceeds the unbound one, we obtain the condition that the particle unbinds, when  $E_{binding} > E_{elasticity}$ . For the geometry shown in Fig. 3.4 this results in

$$\cos \theta \geq \frac{R + \frac{d}{2}}{2(R + \frac{d}{2} + l_0)} + \frac{R + \frac{d}{2} + l_0}{2(R + \frac{d}{2})} - \frac{(\sqrt{-\frac{2E_{binding}}{k_l}} + l_0)^2}{2(R + \frac{d}{2}) \times (R + \frac{d}{2} + l_0)} \quad (3.8)$$

Using the values from section 3.2.1, this leads to  $\theta \gtrsim 27^\circ$ . We present the detailed calculation of the Eq. (A.6) in Appendix B.1.



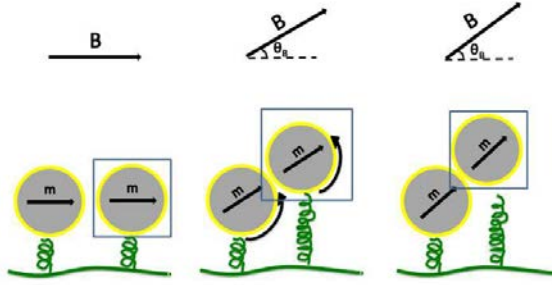


Figure 3.4: Schematic view of a magnetosome particle (shown in blue frame) connected to the filament in the presence of dipole–dipole interaction and an external magnetic field with the angle  $\theta_B$  relative to the direction of the filament. At the threshold angle of  $\theta_B \simeq 27^\circ$ , the binding energy rises higher than the elastic energy and therefore the binding to the filament is not anymore an advantage.

### 3.4.2 Dynamics of rupture

For more detailed study of the chain stability, we performed Monte Carlo simulations for different field strengths (20 mT, 50 mT, 150 mT) and changed the orientation of the field (angle  $\theta_B$ ) in a stepwise manner, increasing the angle by  $1^\circ$  every  $10^{+7}$  Monte Carlo steps, from  $0^\circ$  to  $90^\circ$  relative to the direction of the filament. We measured the orientation of the magnetic moment (angle  $\theta_m$ ) of the magnetosome chain, the number of bound particles as a function of the angle.

In our simulations, rupture of particles from the filament is seen for the field strength of 50 mT and higher. For weak field strength (20 mT), the magnetic moment of the chain follows the external field only weakly, reaching a maximal deflection of  $\theta_m \sim 20^\circ$ . This change in the angle results mostly from the particles at both ends of the chain. These are pulled away from the filament by the rotation of the field, detach from the filament and orient in the direction of the field. Unbinding of the particles at the end occurs at the critical angle,  $\theta_B \sim 20^\circ$ . Other than that, the linear arrangement of the particles on the filament is not disrupted.

For the field strength of 50 mT and higher, rupture occurs through two discrete events at different critical values of the angle between the field and the filament. At

the first critical angle,  $\sim 10^\circ$  for the field strength of 50 mT, the two ends of the chain unbind from the cytoskeletal filament and tilt away from the chain axis toward the direction of the external field as seen for the case of 20 mT. At the second critical angle,  $\sim 77^\circ$  for the field strength of 50 mT, the chain fragments into smaller pieces that are oriented in the direction of the field and are bound to the filament through their two middle particles. When a stronger field is used the magnetosome particles are rotated to larger angles which increases their linkage pull in early steps. Therefore rupture occurs at smaller angles of the external field (smaller critical angles) and at the rupture point the transition in the angle of the chain magnetic moment is smaller. The shift of the two critical angles as a function of the field strength is shown in Fig. 3.6. While the first (lower) critical angle is present for all field strengths we simulated, the second critical angle is only seen for fields of 50 mT and higher.

The rupture process is stochastic and shows some variation between different runs of the simulation, in particular for the intermediate field strength of 50 mT, where the second rupture step occurs in a window of approximately  $7^\circ$ . We tested whether this variability is due to dynamic competition between the rate at which the angle  $\theta_B$  increases and the rate of the rupture process, but simulations in which the angle was varied two-fold faster or slower showed very similar results. The key role in the chain rupture is played by the competition between the dipole–dipole interactions and the interactions of the dipoles with the external field. If the field direction is parallel to the chain, both these interactions will have the minimum energy. By rotating the external field, relative to the direction of the filament, the interaction with the external field drives the dipoles toward an alignment with the external field, while the dipole–dipole interactions favour a dipole orientation along the chain axis. Rotating the dipoles, thus increases the dipole–dipole energy, up to the point, where the attractive dipole–dipole force becomes repulsive. At this point, the magnetosome chain breaks into pieces. The conversion of the dipole–dipole interactions from attraction to repulsion for two fixed dipoles at zero temperature are detailed in Appendix B.3. However, the two particles at the two ends, due to the weaker dipole–dipole stabilisation, follow the external field more freely, giving rise to the first critical angle. As

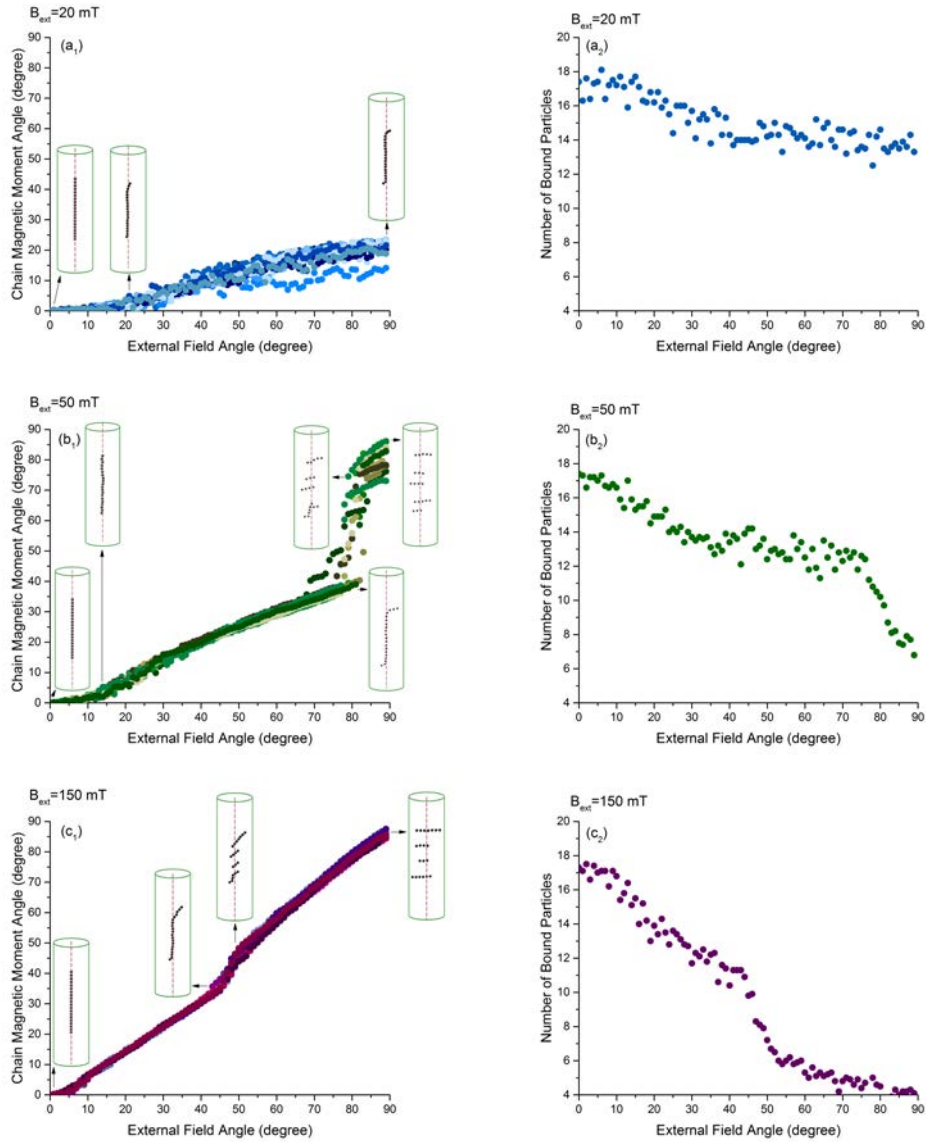


Figure 3.5: Response of the chain magnetisation to a rotation of the external field:  $a_1$ ,  $b_1$  and  $c_1$  show the change in the orientation of the chain magnetic moment in different angles and strengths of the external field. How the average number of magnetosome particles bound to the filament changes during the rupture is presented for each field strength in  $a_2$ ,  $b_2$  and  $c_2$ . In each plot, different colours represent 10 trajectories extracted from Monte Carlo simulations.

Fig. 3.6(b), indicates the angle of the chain magnetic moment at the critical angles of the external field is independent of the external field strength and it arises from the dipole–dipole interactions. Losing the linkers of the particles to the filament can be followed more closely at each state of the rupture by looking at the change in the

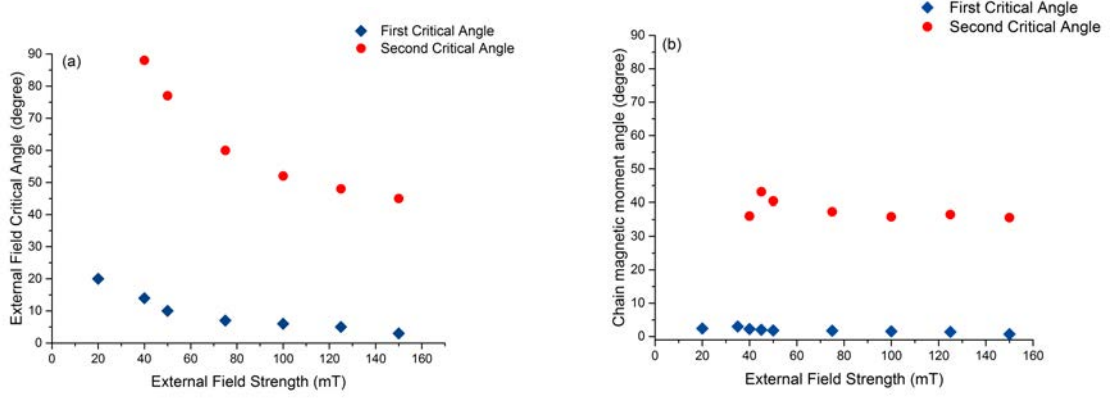


Figure 3.6: (a) The external field critical angles for chain rupture: As field strength increases, the magnetosome chain ruptures at lower values of the external field angle. (b) Chain magnetic moment angle at first and second critical angles of the external field as a function of the field strength. The figure shows the independence of this angle from the field strength.

number of bound particles to the filament. Steep changes in the number of bound particles at critical angles are observed, Fig. 3.5(a<sub>2</sub>, b<sub>2</sub> and c<sub>2</sub>).

Fig. 3.8 shows how the individual energy contributions change during the rupture process. After rupture, the dipoles in each smaller chain are aligned with each other, but from one chain to the other they are parallel. Therefore the dipole–dipole interaction decreases but not to the initial minimum, as shown in Fig. 3.8(a). However, as the dipoles in the smaller pieces are all aligned with the external field, their interactions with external magnetic field decreases to its minimum value, see Fig. 3.8(b). The non–zero values of binding and elastic energies are due to the attachments of particles in the middle of the chains to the filament (Fig. 3.8(c,d)). The observation of a slowdown in the sharpness of the binding and elastic energy after the first critical point is explained by the fact that the detached particles do not contribute any longer to the binding and elastic energies.

In case the dipole–dipole interactions are too weak to preserve the linear arrangement of dipoles, the dipoles follow the external field after the first critical point without restraint. This starts from both ends of the magnetosome chain and leads to a single chain along the external field than multiple fragmented chains. Fig. 3.7, presents the chain rupture for a magnetosome chain with  $N = 20$  particles with the saturation

magnetisation (per volume) of greigite particles at room temperature of  $0.24 \times 10^6 \text{ Jm}^{-3} \text{ T}^{-1}$  [90]. By reducing the magnetic moment of the particles, the dipole–dipole interactions are weakened ( $\propto m^2$ ) more than the magnetic field–dipole interactions ( $\propto m$ ). In fact, the field–dipole interactions are similar to the interactions of the magnetite particles with a stronger field while the internal interactions between particles are weaker than those between magnetite particles. More details on the disruption of the chain of greigite particles are reported in Appendix B.4.

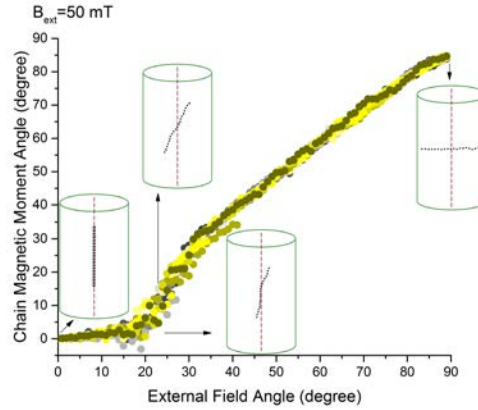


Figure 3.7: Figure shows the change in the orientation of the magnetic moment of a magnetosome chain with  $N = 20$  greigite particles in different angles of an external magnetic field of 50mT.

### 3.4.3 Recovery: Chain reassembly after disruption

Finally, we consider the chain dynamics after rupture. As above, we perform simulations in which the angle of the external field with respect to the filament is increased from  $0^\circ$  to  $90^\circ$ . After reaching  $90^\circ$ , the external magnetic field is turned off. The results of these simulations are plotted in Fig. 3.9. This figure shows that after the chain rupture and removal of the magnetic field, the small magnetosome chains reassemble on the filament. Eventually, the magnetosome chain regains its linear structure along the filament. The full recovery of the magnetosome chain takes about  $50 \times 10^{+7}$  Monte Carlo steps. If we transform this to the unit of the relaxation time for a free magnetosome particle, we obtain  $75 \times 10^{+7}$ .

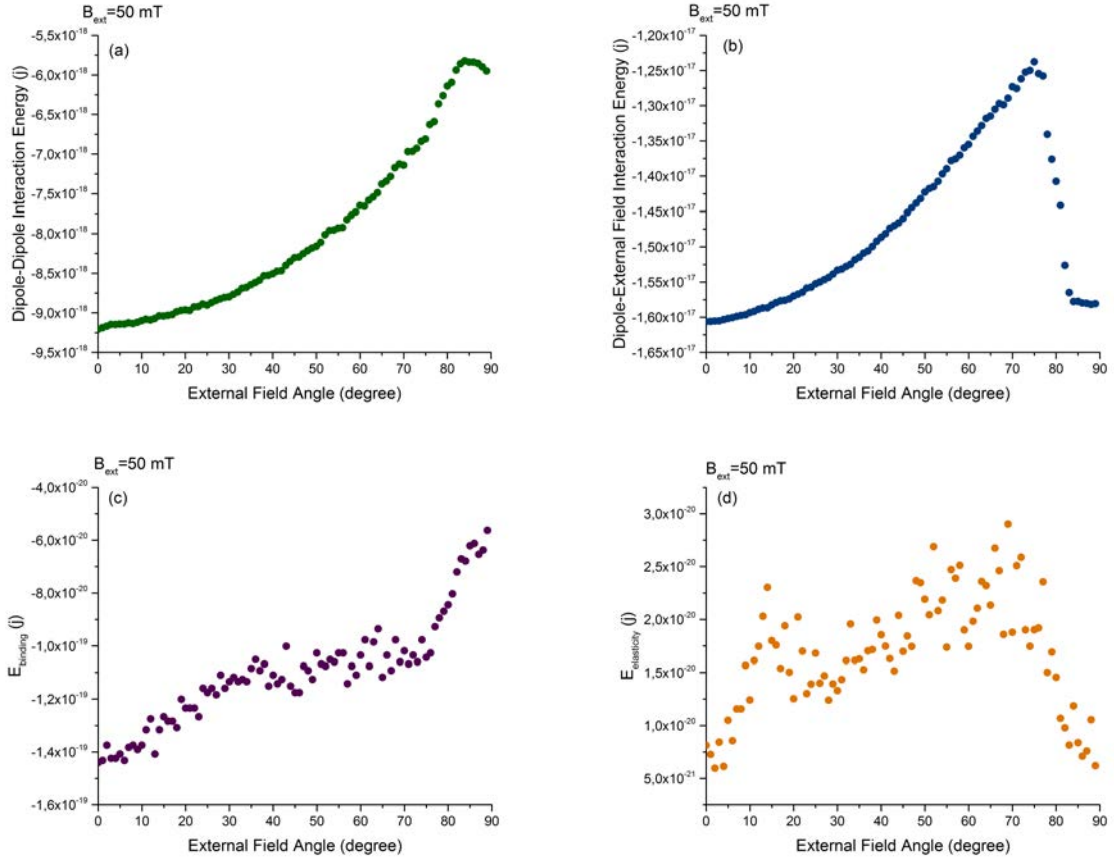


Figure 3.8: Behaviour of the dipole–dipole interactions energy between magnetosome particles (a), the external magnetic field–dipole interaction energy (b) interaction energies of magnetosome particles, the binding (c) and elastic energies (d) of the linkers of the particles to the filament in the magnetosome chain under an external magnetic field of 50mT for different angles of the external magnetic field relative to the direction of the filament.

The reassembled structure of magnetosome chain ensues as well under the condition that after chain disrapture the external field is set back to zero, so that it is aligned with the direction of the filament, see Fig. 3.10. In this case, the chain reforms very rapidly, within  $10^{+7}$  Monte Carlo Steps, which is much faster than the previous case. This observation can be tested experimentally.

These observations together with the results of the electron microscopy images after chain rapture, [55], showing wild–type–like chains rather than fragmented ones when the cells were after rapture, provide support for the rather dynamic nature of the magnetosome chain.

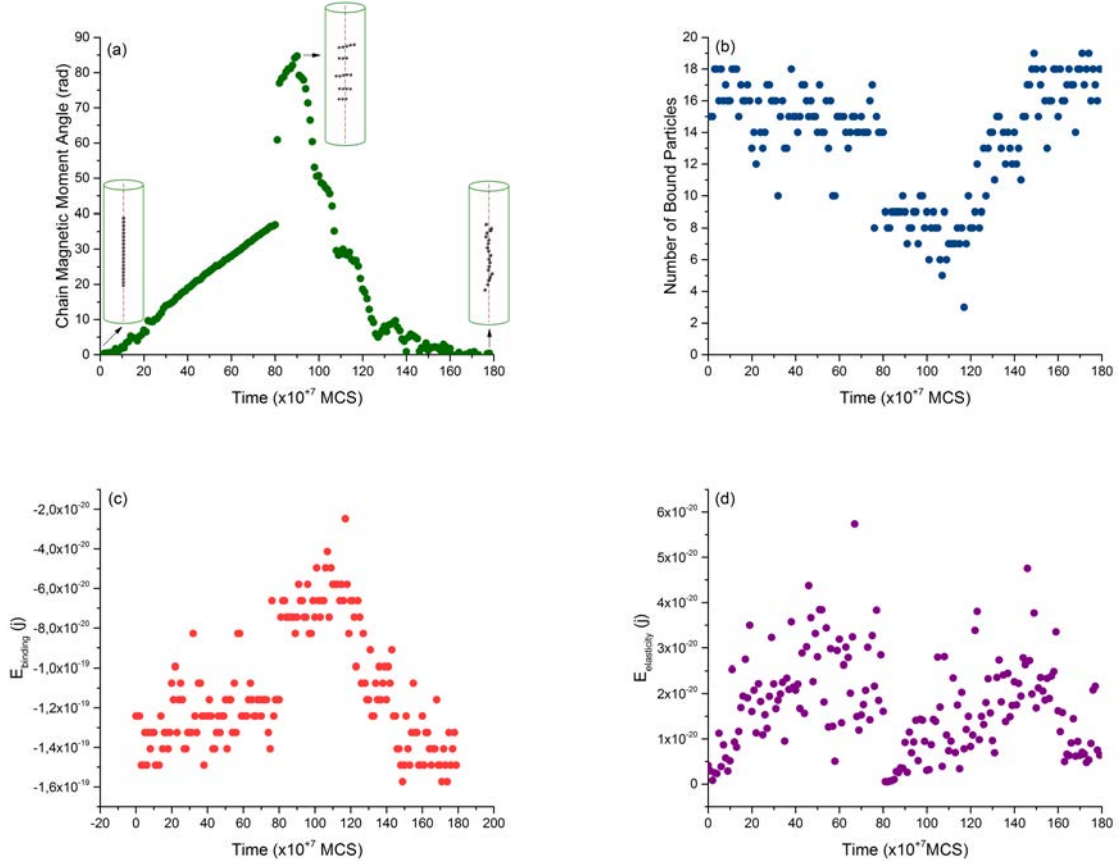


Figure 3.9: Plots represent the change in the behaviour of the magnetosome chain during the disruption with an external magnetic field, from  $0$  to  $90 \times 10^7$  MCS, and after elimination of the external field, from  $90 \times 10^7$  MCS to  $180 \times 10^7$  MCS. While the magnetosome chain regains its linear structure on the filament, the magnetic moments of the particles align to the direction of the filament (a) and particles rebind to the filament therefore the number of particles bound to the filament increases again (b) and the binding energy falls to its minimum values (c). Decrease in the elastic energy to the initial value (d) indicates that the linkers of the particles to the filaments reform with their relaxed length. MCS refers to Monte Carlo Steps.

### 3.5 Concluding remarks

We have developed a theoretical framework to study the structure of magnetosome chains in magnetotactic bacteria which enables us to discuss the energetics, stability



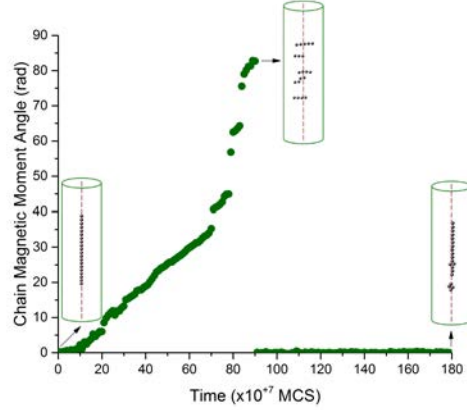


Figure 3.10: The plot depicts the recovery of the magnetosome chain after treatment with an external field aligned with the direction of the filament. MCS refers to Monte Carlo Steps.

and mechanical properties of magnetosome chains. Our model has taken into account magnetostatic interactions between magnetosome particles and between magnetosome particles and an external magnetic field. Also, magnetosome particles in our model were allowed to bind to the cytoskeletal filament via elastic linkers.

First, we investigated the equilibrium configurations and assembly of randomly distributed magnetosome particles. Our results presented a variety of different equilibrium configurations including linear chains, closed-rings and handle-like structures with chain and ring structures most widely occurring. We showed that in the transition from a chain structure to a ring structure, there is an energy cost due to the bending of the linear chain. However, in closing into a ring, the structure loses entropy and also gains an additional dipole-dipole interaction.

We observed that in the presence of the binding potential to the filament, as the binding energy rises more chains and fewer rings form and at highest binding energies ( $E_b = 8K_B T$ ,  $E_b = 16K_B T$ ) the structures assemble around the filament with all their particles bound to it. Most importantly, our simulation shows that for assembly of magnetosome particles into a stable linear structure, presence of a binding energy to the cytoskeletal filament is needed.

We looked at the effect of the external field. Dependent on the strength of the external field and binding energy, single or multiple chains attached to the filament in



the middle of the chain were observed. For the multiple chain structure, we found the repulsive dipole–dipole interactions between smaller chains as a source which is kinetically stabilising this configuration.

In the next step, we employed our model to explore the mechanical structure of magnetosome chains. Our analysis indicates that in the presence of external stimuli the stability of the magnetosome chain is due to the internal dipole–dipole interactions, the stiffness and the binding energy of the protein structure connecting the magnetosome particles to the filament. Nevertheless, the cardinal element of the chain stability is the dipole–dipole interaction. We elucidated that, after a threshold of the magnetic field strength, the rotation of the dipoles alter the attraction dipole–dipole interactions with the repulsion interactions and this leads to the rupture of the magnetosome chain into the fragmented pieces. In contrary to that, in the case of inadequate dipole–dipole interactions, external field–dipole interactions play the major role and rotates the dipoles to a single chain aligned with the direction of the external field. Comparing our observations, during and after the treatment of the magnetosome chain with the external magnetic field, with the results of the experimental work carried out by Koernig et al., [55] substantiates the stabilisation of magnetosome chains to the cytoskeletal filament by MamJ linkers and the dynamic feature of these structures in magnetotactic bacteria.



# Chapter 4

## Application of the magnetosome chain model to FMR spectroscopy

### 4.1 Introduction

The total magnetic moment of ferromagnetic materials subjected to a static external magnetic field is quantized which results in discrete energy states. This effect is known as Zeeman effect. The difference between energy levels is equal to the energy of a photon absorbed or emitted for a transition from one energy level to the other meaning that it is proportional to the frequency of the photon. This frequency is known as the precessional frequency. In the presence of a radio–frequency (RF) transverse field, if the frequency of the RF field is equal to the precessional frequency the energy absorption occurs. In this case, the RF field frequency is the resonance frequency [91]. The magnetic resonance frequency,  $\omega$ , is connected to the free energy of the system and its general form for anisotropic ferromagnets with magnetisation per volume,  $M$ , is

$$\left(\frac{\omega}{\gamma}\right)^2 = \frac{1}{M^2} \left[ \partial_{\theta\theta} E \left( \frac{\partial_{\varphi\varphi} E}{\sin^2(\theta)} + \frac{\cos(\theta)}{\sin(\theta)} \partial_{\theta} E \right) - \left( \frac{\partial_{\theta\varphi} E}{\sin(\theta)} - \frac{\cos(\theta)}{\sin(\theta)} \frac{\partial_{\varphi} E}{\sin(\theta)} \right)^2 \right], \quad (4.1)$$

where  $\partial_\theta E$ ,  $\partial_\varphi E$  and  $\partial_{\theta\theta} E$ ,  $\partial_{\varphi\varphi} E$  are the first and second derivatives of the energy  $E$  with respect to the polar ( $\theta$ ) and azimuthal ( $\varphi$ ) angles of magnetic moment, see Fig. 4.1.  $\gamma = 1.76 \times 10^{11} \text{ rad s}^{-1}\text{T}^{-1}$  is the gyromagnetic ratio [92].

Ferromagnetic resonance (FMR) represents this response of ferromagnetic materials

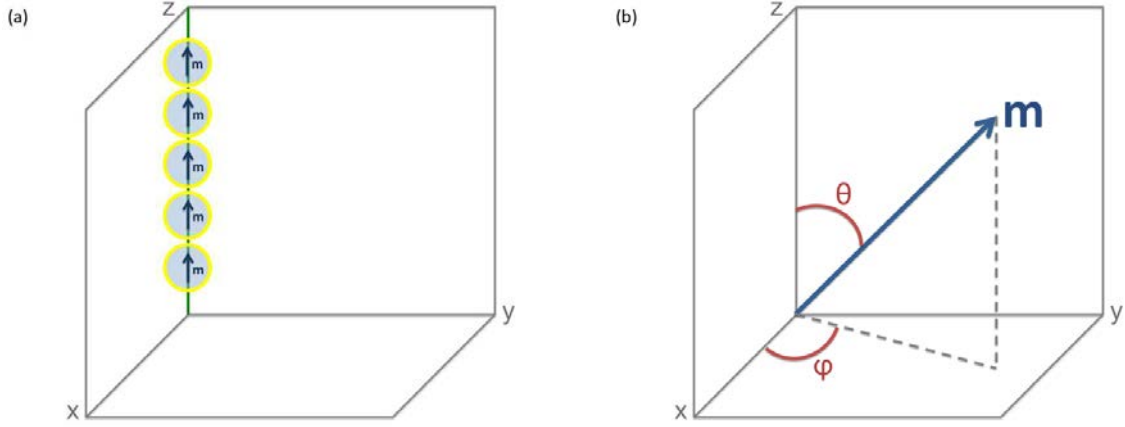


Figure 4.1: Schematic view of (a) the magnetosome chain and (b) the cartesian coordinate system.

to excitations caused by electromagnetic radiation in the GHz range. As the excitation by microwave radiation has low energy, it allows for the study of the ground state properties of ferromagnetic materials such as magnetisation,  $g$  factor [93] and magnetic anisotropy [94]. FMR offers a polar and angular investigation of the specimen in nanoscale and therefore the spectra obtained can be employed to extrapolate the features such as shape and anisotropy of the magnetic crystals. While other techniques to determine these quantities are limited. For example, coercivity analysis is time-consuming and becomes unstable with increasing numbers of magnetic components [95].

The FMR spectroscopy has attracted interest in studying magnetic properties of magnetosome particles produced in magnetotactic bacteria. The FMR spectra of magnetotactic bacteria have been widely investigated for the effect of magnetosome chains structure and crystal morphology. In 2006, Kopp et al. showed that sediments containing bacterial magnetite, as well as those containing magnetofossils, exhibit characteristic FMR spectra that provide a useful tool in the search for samples likely

to comprise these materials [96]. In samples containing bacterial magnetite, their FMR measurements allowed for rapid assessment of the degree of disruption of the magnetosome chains in the sample. In another study, FMR spectroscopy of different strains and mutants of magnetotactic bacteria was used to show that the positive magnetic anisotropy observed in these bacteria is a product of chain alignment and particle elongation [97]. FMR measurements on different strains of magnetotactic bacteria demonstrated that the spectrum obtained from each strain has a form which is distinct from the spectra of all the other strains and results from the unique arrangements of magnetosome particles in that strain [98]. Charilaou et al. [99] presented a computer model to simulate the FMR spectra of magnetosome chains. In their modelling approach, they approximate the linear arrangement of the magnetosome chain with a prolate ellipsoid. This approximation is valuable for long intact magnetosome chains but it is limited in some cases such as magnetosomes structure in  $\Delta mamJ$  mutant where the linear assembly of particles on the filament is disrupted.

All the aforementioned measurements were carried out on bulk samples. Very recently people have started to develop techniques to obtain FMR spectra from individual single cell of magnetotactic bacteria. In one experiment, Terwey et al. could distinguish different spin excitations in nanoparticles of a chain within a single bacterium [100]. In general, FMR measurements on a single chain are expected to convey more information on the magnetic characteristics of magnetosome particles. It also allows the investigation of the shape (morphology) and the arrangement of particles in the chain and their effect on the observed spectra.

In this chapter, we employ our theoretical model for magnetosome chains that was introduced in chapter 3 to simulate FMR spectra for a single cell of magnetotactic bacteria. We explain how the spectra obtained from FMR measurements on single cells provide details about the structure of the magnetosome chains which can not be differentiated in FMR analysis of bulk samples. In addition, we propose the application of the FMR spectroscopy as an additional tool for probing the type of the magnetosome chain contained in unidentified samples.

## 4.2 Models and methods

### 4.2.1 Model

We employ the model developed in chapter 3 for magnetosome chains. In our model, a magnetosome chain has been described as a linear chain of  $N$  spherical magnetosome particles connected to the rigid filament by elastic connections. The full energy of the system includes the dipole–dipole interactions energy  $E_{\text{dd}}$  and the external magnetic field–dipole interaction energy  $E_{\text{B}}$ .

$$\begin{aligned}
 E &= E_{\text{dd}} + E_{\text{B}} \\
 &= -\frac{\mu_0}{4\pi} \sum_{i,j=1,j>i}^N \frac{1}{r_{ij}^3} \left( \frac{3(\mathbf{m}_i \cdot \mathbf{r}_{ij})(\mathbf{m}_j \cdot \mathbf{r}_{ij})}{r_{ij}^2} - \mathbf{m}_i \cdot \mathbf{m}_j \right) \\
 &\quad - \sum_{i=1}^{i=N} \mathbf{m}_i \cdot \mathbf{B},
 \end{aligned} \tag{4.2}$$

$\mu_0 = 4\pi \times 10^{-7} \text{NA}^{-2}$  is the vacuum permeability, the  $\mathbf{m}_i$  and  $\mathbf{m}_j$  are the magnetic moments of the dipoles and the  $\mathbf{r}_{ij}$  is the distance vector between them, with  $r_{ij} = |\mathbf{r}_{ij}|$ . In the following, we will assume that all dipoles have equal absolute value  $|\mathbf{m}_i| = m$ . Since frozen bacteria are used in the experiment, we assume that the magnetosome particles are fixed in their location in the bacteria and also the linkers connecting the particles are fixed resulting in the absence of the binding energy, elastic energy and hard–core potential in the energy Eq. (4.2).

To obtain the resonance frequency of the magnetosome chain, we use Eq. (4.1) to calculate the resonance frequency for each particle  $i$ . Derivatives of the total energy of the particle  $i$  in respect to its polar and azimuthal angles  $\theta_i$  and  $\varphi_i$  are found in the Appendix C.1.

Using the first and second derivatives of the energy  $E$ , we obtain the resonance

equation for each magnetosome particle in our model,

$$\begin{aligned}
\left(\frac{\omega_i}{\gamma}\right)^2 = \frac{1}{M^2} & \left[ \left( -\frac{\mu_0}{4\pi} \sum_{j=1}^N \frac{m^2}{r_{ij}^3} (-2 \cos(\theta_i) \cos(\theta_j) + \cos(\varphi_i \varphi_j) \sin(\theta_i) \sin(\theta_j)) \right. \right. \\
& \left. \left. - mB (-\cos(\theta_B) \cos(\theta_i) - \cos(\varphi_B - \varphi_i) \sin(\theta_B) \sin(\theta_i)) \right) \right. \\
& \times \left( \frac{1}{\sin^2(\theta_i)} \times \left( -\frac{\mu_0}{4\pi} \sum_{j=1}^N \frac{m^2}{r_{ij}^3} (\cos(\varphi_i - \varphi_j) \sin(\theta_i) \sin(\theta_j)) \right. \right. \\
& \quad \left. \left. + mB (\cos(\varphi_i - \varphi_j) \sin(\theta_B) \sin(\theta_i)) \right) \right. \\
& \quad \left. + \frac{\cos(\theta_i)}{\sin(\theta_i)} \times \left( -\frac{\mu_0}{4\pi} \sum_{j=1}^N \frac{m^2}{r_{ij}^3} (-2 \cos(\theta_j) \sin(\theta_i) - \cos(\theta_i) \cos(\varphi_i - \varphi_j) \sin(\theta_j)) \right. \right. \\
& \quad \left. \left. - mB (\cos(\theta_i) \cos(\varphi_B - \varphi_i) \sin(\theta_B) - \cos(\theta_B) \sin(\theta_i)) \right) \right) \\
& - \left( \frac{1}{\sin(\theta_i)} \times \left( -\frac{\mu_0}{4\pi} \sum_{j=1}^N \frac{m^2}{r_{ij}^3} (\cos(\theta_i) \sin(\theta_j) \sin(\varphi_i - \varphi_j)) \right. \right. \\
& \quad \left. \left. - mB (\cos(\theta_i) \sin(\theta_B) \sin(\varphi_B - \varphi_i)) \right) \right. \\
& \quad \left. - \frac{\cos(\theta_i)}{\sin^2(\theta_i)} \times \left( -\frac{\mu_0}{4\pi} \sum_{j=1}^N \frac{m^2}{r_{ij}^3} (\sin(\theta_i) \sin(\theta_j) \sin(\varphi_i - \varphi_j)) \right. \right. \\
& \quad \left. \left. - mB (\sin(\theta_B) \sin(\theta_i) \sin(\varphi_B - \varphi_i)) \right) \right)^2 \Big].
\end{aligned} \tag{4.3}$$

## 4.2.2 Computer simulation

We carry out the Monte Carlo simulation for  $N = 20$  magnetosome particles in a cylindrical box in which magnetosome particles are fixed on the filament and are under an external magnetic field with fixed strength value and orientation at room temperature. Since we assume that particles are fixed in their location, each Monte Carlo step includes only a random change between  $-5$  to  $+5$  degree in the polar and azimuthal orientation of the magnetic moment for a random particle. The total number of steps in the simulation is  $10^{+5}$ . For more detail on the simulation approach see section 3.2.2.

Obtaining the equilibrium orientation of the magnetic moments of the particles from Monte Carlo simulation, we calculate the resonance frequency of the magnetosome particles given by Eq. (4.3). In this way, the equilibrium orientations of the magnetic moments and the resonance frequency of magnetosome particles,  $\omega_i$ , are obtained for different values of the external field strength and orientation.

In experiments, often the frequency is kept constant and the field strength is varied. This leads to a resonance field which is obtained by solving Eq. (4.3) for the external field strength. Therefore, in the next step, for each orientation of the external field we search among all field strengths and extract the angles of magnetic moments which for their corresponding resonance frequency  $\omega_i - \omega_{exp} < 0.01\omega_{exp}$  and  $\omega_i - \omega_{exp}$  is the smallest among all the frequencies obtained for this field orientation, we call this value  $\omega_{res}$ .  $\omega_{exp} = 5.8936 \times 10^{10}$  Hz is the resonance frequency obtained from the experimental study [101]. Next, we place the extracted orientations of magnetic moments of particles, the orientation of the external field and the value of the experimental frequency in the Eq. (4.3) and we solve the equation again but for the field values and derive the field strength which fits in this equation, these values are called  $B_{res}$ . By performing the same procedure for all the azimuthal and polar orientations, we obtain the resonance field value,  $B_{res}$ , at all the directions.

### 4.2.3 Resonance spectrum

The absorption spectra are then determined by assuming a gaussian line shape around the resonance field,

$$F_i(B_{ext}) = a_1 e^{-\frac{|B_{ext} - B_{res}^{(i)}|^2}{a_2}}. \quad (4.4)$$

Here  $a_1$  is a measure of the absorption intensity. For the rest of our discussion we use  $a_1 = 1$ . The parameter  $a_2$  characterises the width of the gaussian function. The gaussian function describes the absorption observed for one magnetosome particle. The full spectrum for a chain of magnetosome particles is obtained as a sum of these



peaks,

$$F(B_{ext}) = \sum_{i=i}^{i=N} F_i(B_{ext}). \quad (4.5)$$

In experiments, the first-order derivative of this absorption is determined.

### 4.3 Resonance field of magnetosome particles

We perform our simulations and calculate the resonance field at room temperature  $T = 300^\circ K$  for the middle particle in a linear arrangement of spherical magnetosome particles with radius  $R = 20$  nm, the gap distance of  $d = 10$  nm between adjacent particles and saturation magnetisation of  $M = 0.48 \times 10^{+6} JT^{-1}m^{-3}$ . The map of the resonance field,  $B_{res}$ , for different orientations of the external field relative to the direction of the chain,  $z$ -axis is shown in Fig. 4.2. The resonance field for magnetosome particles in a chain along the  $z$ -axis shows an uniaxial symmetry around the  $z$ -axis.

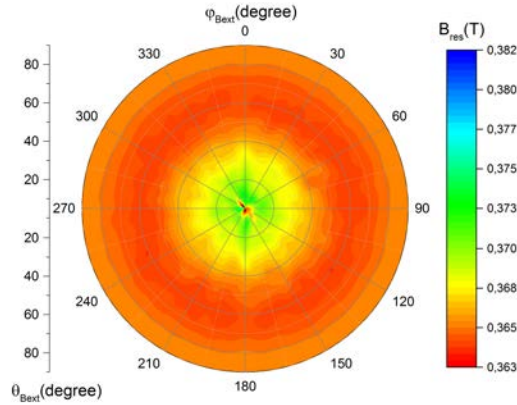


Figure 4.2: Map of resonance field for  $0^\circ < \theta_{B_{ext}} < 90^\circ$  and  $0^\circ < \varphi_{B_{ext}} < 360^\circ$  for a magnetosome particle in the middle of a magnetosome chain with  $N = 20$  particles.  $\theta_{B_{ext}}$  and  $\varphi_{B_{ext}}$  are polar and azimuthal angles of the applied field relative to the direction of the chain,  $z$ -axis. The resonance field shows an uniaxial symmetry around the  $z$ -axis.

Fig. 4.3 shows the absorption spectrum of the magnetosome chain for two widths of the gaussian function, 5 mT and 30 mT. The peaks in the absorption plot present the value of the applied field, at fixed orientation of  $\theta_{B_{ext}} = 45^\circ$  and  $\varphi_{B_{ext}} = 45^\circ$ , where the resonance occurs. The values of the applied field at which the absorption peaks are detected originate in the resonance of all the magnetosome particles in the chain. In fact, the resonance for two particles at two ends of the chain takes place at the applied field of  $B_{ext} = 350$  mT and for the particles in the middle of the chain at  $B_{ext} = 366$  mT. We elaborate on the emergence of resonance at two different field values for particles at two ends and for particles in the middle of the chain in Appendix C.3.

If the difference between field values is smaller than the width of the absorption function, the resonance of the particles at two ends is not detected. In fact, the right choice of linewidth can reveal structural details about the magnetosome chain. The results of Alexandra shows that the random orientations of chains in bulk samples give rise to a broad spectrum which can be greatly improved in FMR measurements on single cells of bacteria.

## 4.4 Magnetocrystalline anisotropy effect

In ferromagnetic materials, the orbits of the electrons are tied to the structure of the crystal therefore due to the spin–orbit interaction the spins favour to align along the well–defined crystallographic axis called the easy axis of the magnetisation [45]. As a result, it is easier to magnetise the crystal in the direction of its easy axis than in other directions. The difference between energies of different directions can be expressed in an energy term called magnetocrystalline anisotropy energy which for a cubic lattice oriented with the [111] axis in the direction of the easy–axis is given by

$$E_{crystal} = K_1 \left( \frac{1}{4} \sin^4(\theta) + \frac{1}{4} \cos^4(\theta) + \frac{\sqrt{2}}{3} \sin^3(\theta) \cos(\theta) \cos(3\varphi) \right), \quad (4.6)$$

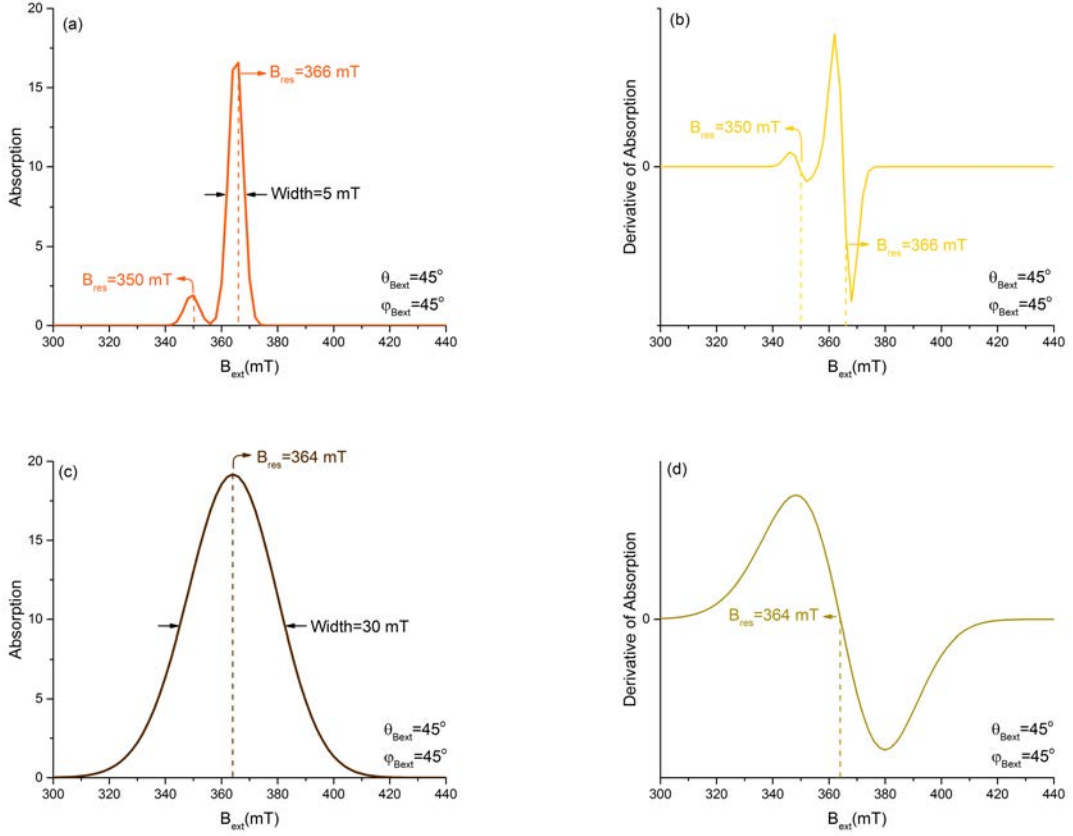


Figure 4.3: Calculated FMR spectra for magnetosome chains: (a, c) show the absorption spectra. (b, d) Derivatives of the absorption spectra as measured experimentally. Upper and lower plots show the same spectra but with different linewidth. Y axis in both plots has an arbitrary unit.

$K_1$  is the first-order anisotropy constant which is  $-1.1 \times 10^5 \text{ Jm}^{-3}$  for magnetite at room temperature [102]. The direction dependence of the magnetocrystalline anisotropy energy can be seen in the angles  $\theta$  and  $\varphi$  between magnetic moment and the direction of the easy magnetisation axis. For magnetite the direction of the easy magnetisation is indeed the body diagonal [111]. In magnetotactic bacteria, the direction of the chain axis (filament) overlaps with the easy axis for most crystals [103].

To investigate the effect of magnetocrystalline anisotropy on the resonance spectra, the magnetocrystalline anisotropy energy term is added to the full energy equation of the system, Eq. (4.2). With the approach presented before, we derive the resonance

field values for all the orientations of the external field. The resonance field map

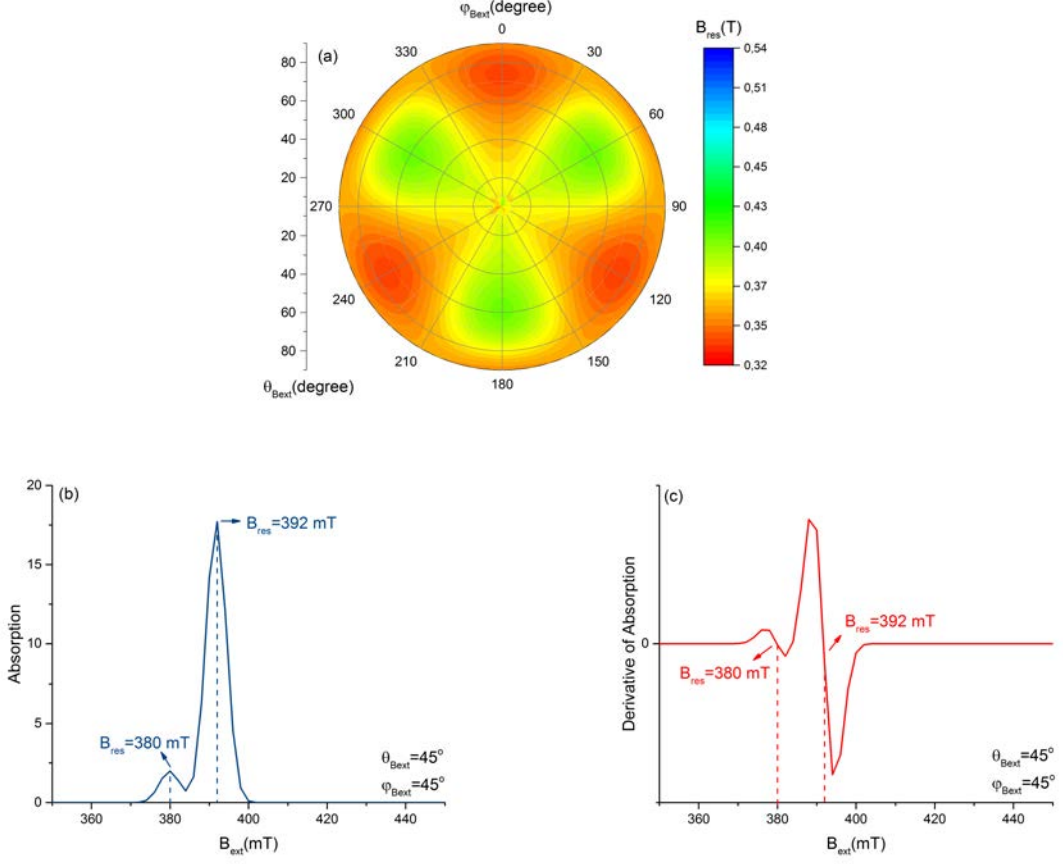


Figure 4.4: (a) The map of the resonance field for  $0^\circ < \theta_{B_{ext}} < 90^\circ$  and  $0^\circ < \varphi_{B_{ext}} < 360^\circ$  for a magnetosome particle with magnetocrystalline anisotropy. The map shows the formation of a three–fold symmetry after incorporating the magnetocrystalline anisotropy energy into the system. The plot present the data for the particle in the middle of a magnetosome chain with  $N = 20$  particles. (b, c) Applying the gaussian function, absorption peaks at  $B_{ext} = 380$  mT and at  $B_{ext} = 392$  mT are observed.

shows a three–fold symmetry with maximum resonance field values at  $\theta_{B_{ext}} = 45^\circ$  and  $\varphi_{B_{ext}} = 60^\circ, 180^\circ$  and  $300^\circ$ . This observation of the three–fold symmetry was reported before in [99, 104]. To illustrate the origin of the three–fold symmetry, which arises due to the magnetocrystalline anisotropy, we show in Fig. 4.5 the individual energy contributions in equilibrium for a magnetosome chain under an external field of  $B_{ext} = 280$  mT with and without the anisotropy term. (The field value of  $B_{ext} = 280$  mT was chosen with no preference.) The comparison between the behaviours of the energies and of the resonance field in different orientations of the external field relative

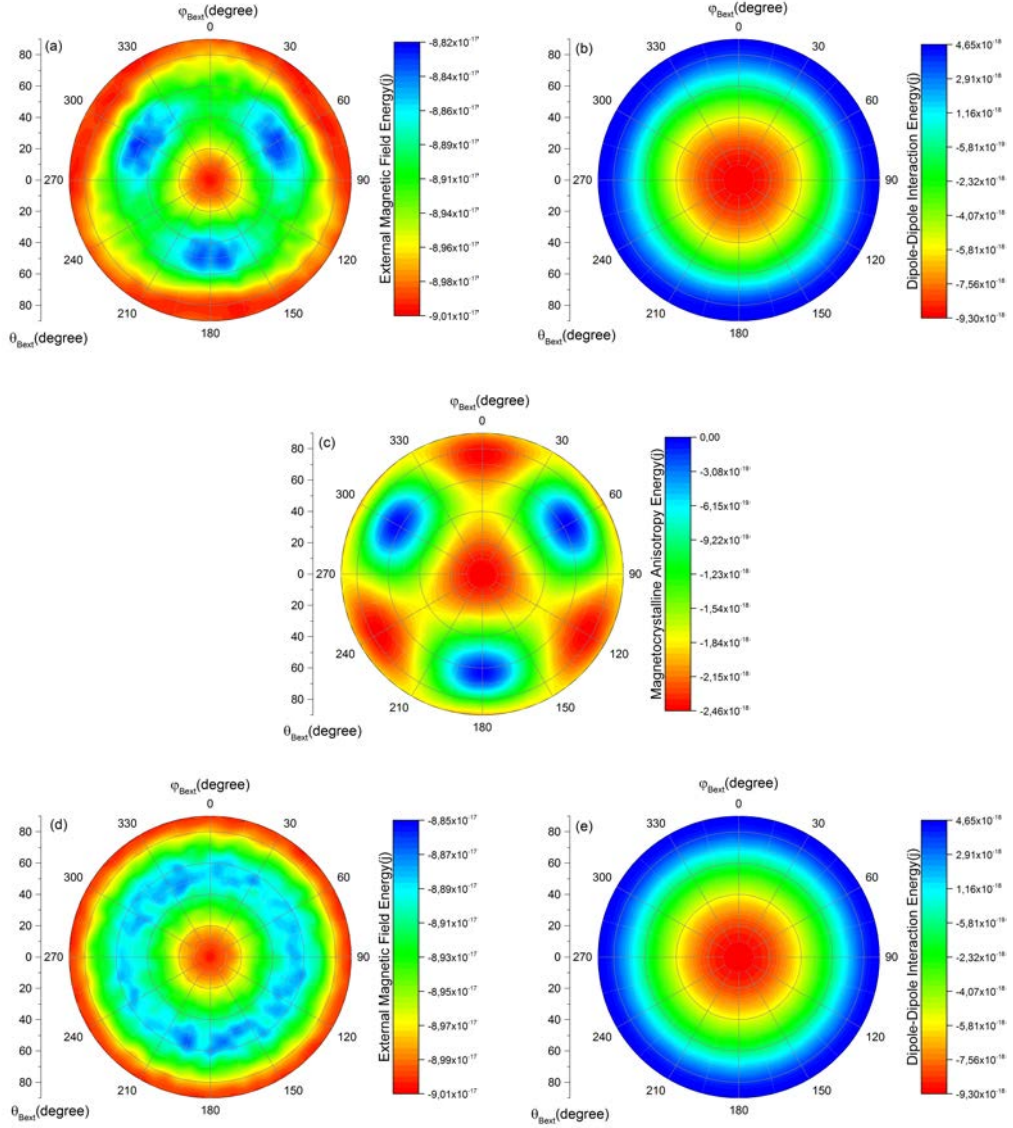


Figure 4.5: On top: (a) External magnetic field–dipole interactions energy, (b) dipole–dipole interactions energy and (c) magnetocrystalline anisotropy energy for a chain 20 magnetosome particles under an external field of 280 mT. On bottom: (d) External magnetic field–dipole interactions energy and (e) dipole–dipole interactions energy for a chain of 20 magnetosome particles without the magnetocrystalline anisotropy and under an external field of 280 mT.

In the presence of the magnetocrystalline anisotropy, the uniaxiality observed in the energies converts into a three–fold symmetry.

to the easy axis of the magnetosome particles suggests a direct relationship between the maximum and minimum values of the resonance field and the magnetocrystalline anisotropy energy.

We monitor the effect of magnetocrystalline anisotropy by comparing the behaviour of the resonance field with (Fig. 4.6(a)) and without (Fig. 4.6(b)) the magnetocrystalline anisotropy term in the energy of the system. Our results demonstrate the periodic (symmetrical) behaviour of the resonance field in the presence of the magnetocrystalline anisotropy. While, in the absence of the magnetocrystalline, no particular trend in the behaviour of the resonance field in connection to the azimuthal angle is observed. We can also demonstrate this effect in the behaviour of the resonance field in different polar angles,  $\theta_{B_{ext}}$ . The shift in the resonance field values with the azimuthal angle is evident in Fig. 4.6(d). As the figure demonstrates, the change in the resonance field with polar angle is also more pronounced with magnetocrystalline energy taken into account.

## 4.5 Effect of the magnetosome chain configuration on the resonance field

Recent progress in isolating individual cells for FMR studies allows us to study properties of a single chain of magnetosome particles in a particular bacterium and without the adverse effects of magnetosome chains of other cells as in bulk samples. One characteristic of magnetosome chains which might be misrepresented in bulk level studies is the arrangements of particles within the chain. Single cell measurements can help us to have a new insight into the impact of this characteristic on resonance spectra. In this section, we address a similar case and investigate the behaviour of the resonance field in two different arrangements of magnetosome particles: a linear magnetosome chain with vacant spaces between particles, similar to a magnetosome chain with defects in the arrangement of particles, and a cluster of magnetosome particles.



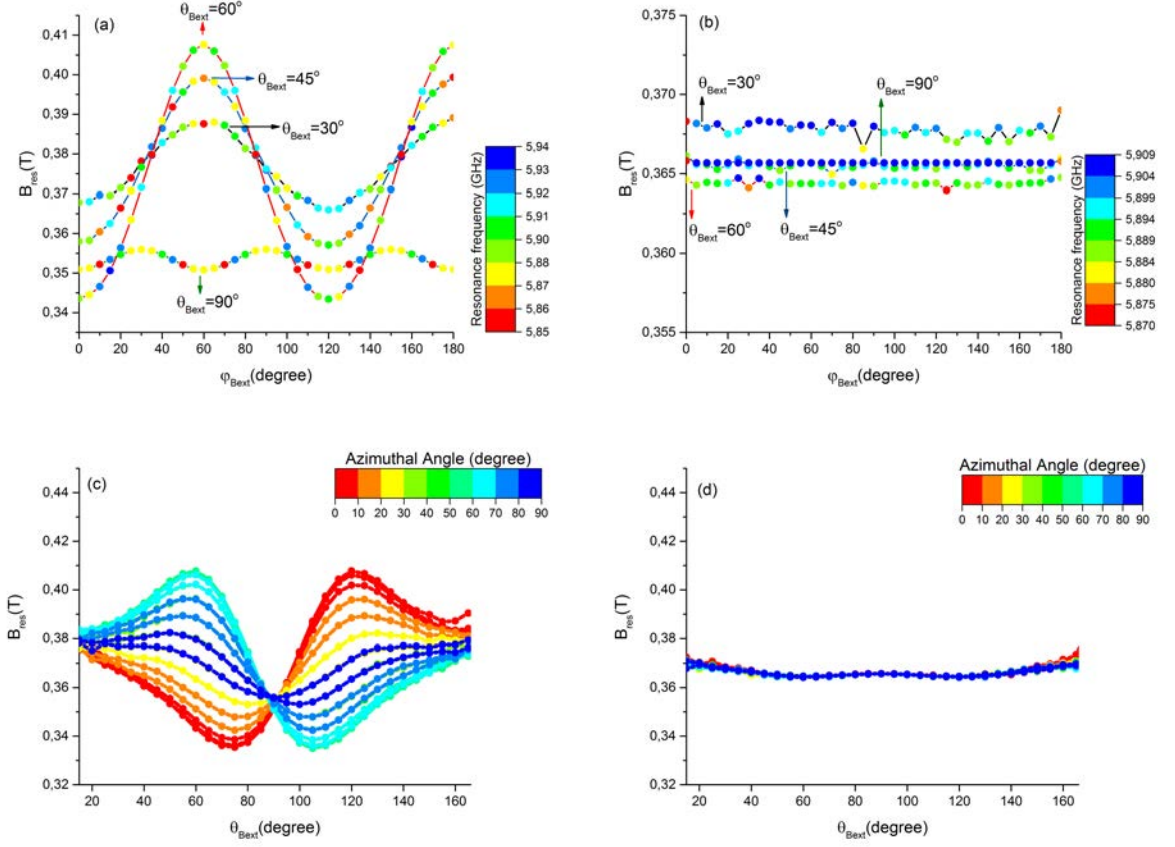


Figure 4.6: On top: Resonance field as a function of the azimuthal angle  $\varphi_{Bext}$  with (a) and without (b) the magnetocrystalline anisotropy. On bottom: Resonance field at different polar angles with (c) and without (d) magnetocrystalline anisotropy. Due to numerical limitations, Resonance field values at  $0^\circ$  and  $180^\circ$  are not calculated.

### 4.5.1 Linear magnetosome chain with defects

First, we study a linear arrangement of magnetosome particles with four particles left out in two different locations on the chain, Fig. 4.7(b). In the same manner, we calculate the resonance field in different orientations for particles with magnetocrystalline anisotropy. Fig. 4.7 shows the resonance field map for the particle in the middle of the lower piece in Fig. 4.7(b). The three-fold symmetry is due to the magnetocrystalline anisotropy.

The resonance appeared at applied fields of  $B_{ext} = 380$  mT and  $B_{ext} = 392$  mT for both intact magnetosome chain and the magnetosome chain with defects. The

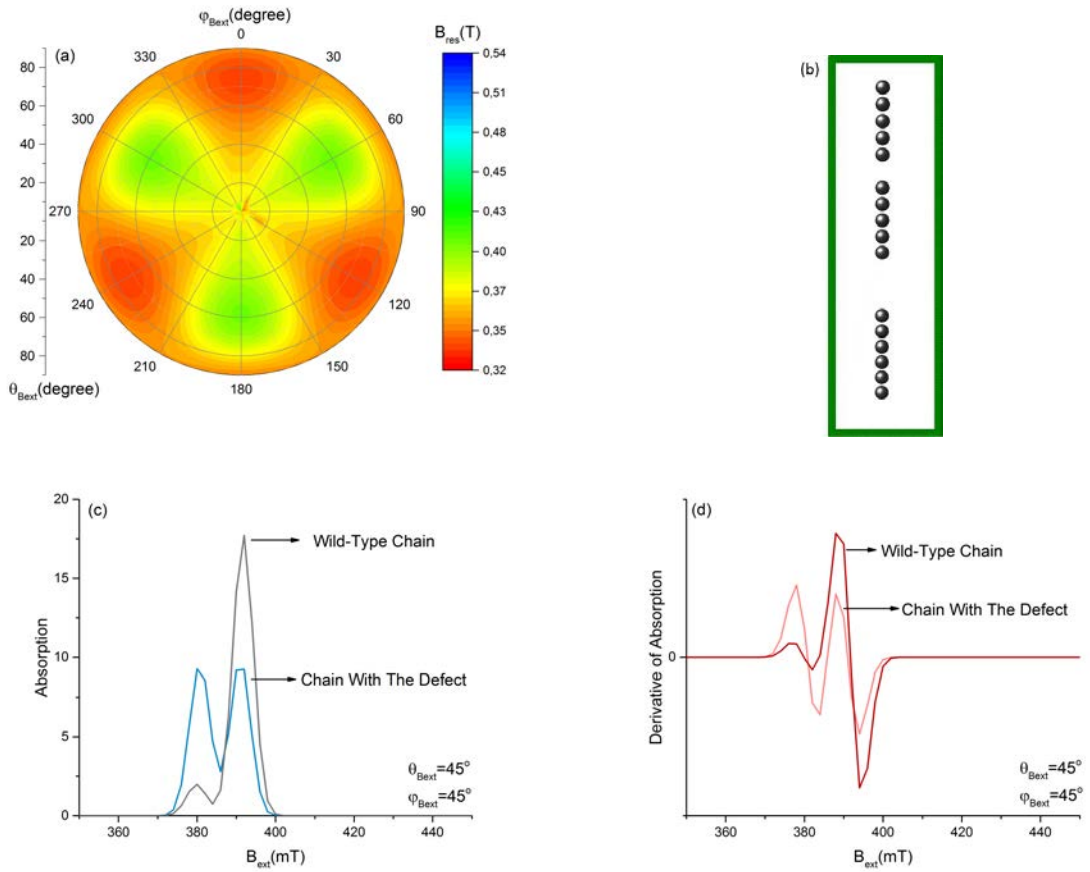


Figure 4.7: FMR spectra of a magnetosome chain with gaps in the arrangement of magnetosome particles: (a) Map of the resonance field for a magnetosome particle in a chain with gaps between particles. The corresponding arrangement is shown in (b). (c, d) Resonance spectra. For Comparison, the resonance spectra for a chain without gaps is also shown.

resonance absorptions, Fig. 4.7, show a clear difference between the spectra of the two structures. For the chain with defects, absorption intensities are the same but lower than the intensity of the major absorption peak in the intact chain. In fact, the comparison between spectra obtained from intact magnetosome chain and from the chain with defects indicates the capacity of the resonance spectra with sufficiently narrow linewidth to detect magnetosome chains with different structural properties.



## 4.5.2 A Cluster of magnetosome particles

We also look at the resonance field behaviour for a cluster of magnetosome particles, similar to the arrangement of magnetosome particles in  $\Delta mamJ$  mutants of magnetotactic bacteria, Fig. 4.8(b). We notice that the directional behaviour of the resonance field recurs. Particles interact via dipole–dipole interactions yet because of their random positions in the cluster these interactions differ from one particle to the other. We note that in the calculation of the crystalline anisotropy energy for particles in the cluster we take a simplifying assumption that the crystalline structure in all the magnetosome particles in the cluster is oriented along the  $z$ –axis. The differences in the absorption spectra of the three cases, an intact magnetosome chain, a magnetosome chain with a defect and a cluster of magnetosome particles, suggest specific footprints for each magnetosome chain which can be used to assess the structure of the chain under investigation.

## 4.6 Concluding remarks

In this chapter, we employed our theoretical model of magnetosome chains to study the FMR spectra of magnetosome chains in magnetotactic bacteria. For spherical magnetosome particles without the crystalline anisotropy, the uniaxial symmetry of the resonance field about the axis of the magnetosome chain was observed. We examined the effect of the crystalline anisotropy in ferromagnetic materials by taking into account the magnetocrystalline energy term and explored the relation between crystalline anisotropy and the three–fold symmetry identified in the resonance field under the presence of magnetocrystalline anisotropy. Absorption spectra were determined by assuming a gaussian line shape. The results of our analysis indicated that the resonance takes place at lower field values for directions where crystalline anisotropy energy is weaker. The shift observed in the value of the resonance field for individual particles is due to the exact calculation of the inter–particle dipole–dipole interactions in our model. The explicit consideration of individual particles in our

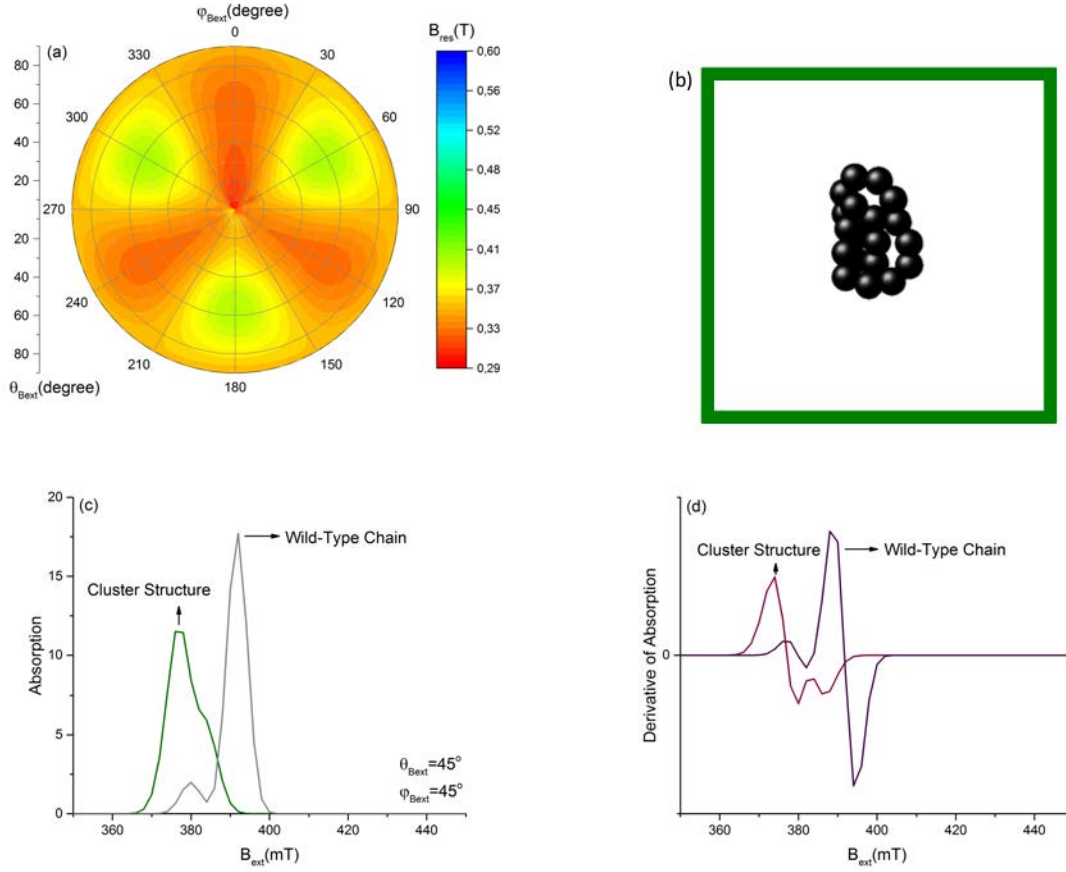


Figure 4.8: (a) The map of the resonance field for a random magnetosome particle in a cluster of  $N = 20$  magnetosome particles with magnetocrystalline anisotropy. (b) Resonance spectra for 20 magnetosome particles in a cluster configuration. The resonance occurs at  $B_{ext} = 376$  and  $B_{ext} = 384$  mT for the cluster configuration of magnetosome particle.

model is beneficial for the study of FMR resonance of magnetosome chains. It allows the investigation of the structural characteristics of magnetosome chains such as the shape and the arrangement of the particles in the chain. Moreover, it can be applied in cases, such as the  $\Delta mamJ$  mutant, where the previous models, including the ellipsoid model, are limited.

Single cell FMR analysis of magnetotactic bacteria promises to offer finer details of magnetosome chains which could not be distinguished in bulk-level FMR studies. With our model, we can investigate the spectra of magnetosome particles in single cells of magnetotactic bacteria. Therefore, we are able to interpret the peculiarity of

different spectra arisen from different mutants of these bacteria. For the observation of such features, a narrow linewidth is crucial which can indeed be achieved in FMR measurements on single cells. We analysed the effect of structural differences on FMR spectra by comparing spectra obtained from a magnetosome chain with defects and from a cluster of magnetosome particles, similar to those in  $\Delta mamJ$  mutants, with the spectrum obtained from a linear arrangement of magnetosome particles resembling their arrangement in wild-type magnetotactic bacteria. The resonance appeared at applied fields of  $B_{ext} = 380$  mT and  $B_{ext} = 392$  mT for the chain with defects and at  $B_{ext} = 376$  mT and  $B_{ext} = 384$  mT for the cluster configuration of magnetosome particles. In addition, for both configurations, the intensity of absorption was found to be lower than the intensity of the major absorption peak in the intact chain of magnetosome particles. These observations imply the sensitivity of the obtained ferromagnetic resonance to the structure of the chain. This capacity of our model to discriminate between different structures of magnetosome chains might also suggest that it might be used as a supplementary method for detection of the type of magnetosome chains present in obscure samples. In continuation of the project discussed in this chapter, we intend to combine our results with the FMR data obtained from experiments on in vivo bacteria to gain more understanding of the absorption spectra of different strains and mutants of magnetotactic bacteria.



# Chapter 5

## Summary, Conclusion and Outlook

Magnetotactic bacteria possess an intracellular magnetic dipole called the magnetosome chain. Magnetosome chains contain membrane–enclosed magnetic nanoparticles which are delicately organised into a linear structure on the cytoskeleton of the bacteria. As a result of the response to the external magnetic field, the torque exerted on the fixed magnetosome particles within the cell of magnetotactic bacteria orients the cell along the magnetic field. By reason of magnetostatic interactions the arrangement of magnetic particles in these “self–propelled compass needles” determines directly the cellular magnetic dipole and in case of majority of magnetotactic bacteria the fine arrangement of magnetosome particles into linear structure maximises the efficiency of the dipole and therefore it is of great relevance to study the stability and mechanical properties of magnetosome chains. With our theoretical framework based on the energetics of magnetosome chains, we investigated the bending rigidity, equilibrium structures and mechanical properties of magnetosome chains. First, we addressed the bending stiffness of magnetosome chains. The bending stiffness stems from magnetic interactions of magnetosome particles which drive the formation of linear chains and from the elastic stiffness of the cytoskeletal filament to which magnetosome particles are anchored. Our analysis indicated that whilst the bending stiffness of the filament can dominate the stiffness due to magnetic interactions, these interactions alone can form straight structures with a persistence length which exceeds the chain length. More crucially, our results showed that in case of a

chain of magnetosomes with four particles or more, the linear arrangement of particles is not the most stable configuration and despite the cellular confinement, without the attachment of particles to the cytoskeleton, such configurations may close to ring-like structures which have no net magnetic moment and thus can not perform the function of a compass in cellular navigation. From this analysis along with observations of clusters of magnetosome particles in magnetotactic bacteria, we reasoned that one of the roles of the filament is to stabilise the straight structure of magnetosome particles. We then investigated the equilibrium configuration of magnetosome particles. The structure formation in magnetic nano-particles has been the subject of numerous studies in other fields including colloidal fluids [105, 106], nanomechanics [58], materials chemistry [107], and micro-swimmers [108]. Our results presented a variety of structures such as linear chains, closed rings and handle-like structures. Among those, chains and rings were the most observed structures in our simulation. Despite the minor energy difference between the two structures, the transition from one to the other could be characterised by the interplay between energy gain and entropy loss of closing to a ring and the energy cost of bending the linear chain.

We allowed for binding of the particles to the cytoskeletal filament and notably we observed that for the assembly of magnetosome particles into linear structures on the filament, a binding potential to the filament is essential, further supporting our conclusion from the bending rigidity calculation. In the presence of an external magnetic field, dependent on the strength of the external field and of the binding energy, single or multiple straight chains linked to the filament through the particles in the middle of the chains were observed. Interestingly, we observed that due to the repulsive dipole-dipole interactions between smaller chains these configurations are kinetically more stable than the configuration of a single chain.

Next, we aimed at probing the mechanical structure of magnetosome chain. We realised that the stability of the magnetosome chain in the presence of external stimuli is a consequence of the interplay between the internal dipole-dipole interactions, the stiffness and the binding energy of the connectors of the particles to the cytoskeletal filament. Notwithstanding, the foremost role is played by dipole-dipole interactions.

As a main result, our analysis of the magnetosome chain rupture under an external magnetic field and of its recovery after disruption entail the stabilisation of the magnetosome chain structure to the cytoskeletal filament by the proteinous connectors and the dynamic nature of this structure. These conclusions are further supported by the results of the *in vivo* investigation of the magnetosome chain stability [55].

Finally, we applied our model to study the FMR spectra of magnetosome chains in magnetotactic bacteria. We simulated the spectra of magnetosome particles in a single magnetotactic bacterium which allowed us to study the distinctive features of individual spectra that arise from different structural properties of magnetosome chains in wild type and in mutants of magnetotactic bacteria. To distinguish the structural features, the right choice of the spectral linewidth is crucial. We explained how the spectra with narrow linewidth enable us to distinguish details which are not noticed in spectra with broad linewidth. Recent results on single cell FMR analysis hold out hope that in contrast to FMR measurements of bulk samples, the narrow linewidth is achievable in FMR measurements of single cells [100].

Magnetotactic bacteria construct a cellular magnetic dipole by exquisitely organising magnetic particles into linear structures on the filament. In this study, we laid a groundwork for studying the equilibrium configurations of magnetosome particles and the mechanical structure of magnetosome chains based on the current knowledge of the magnetosome chain structure: specifically, we have taken into consideration the presence of MamJ protein which interacts with the magnetosome membrane as well as cytoskeletal filament and connects the magnetosome particles to the filament [36]. We analysed the energetics involved in the magnetosome chain stability and tried to explain the dynamics of the *in vivo* chain rupture seen in experiments.

Experiments which can shed some light on the finer structure of the filament and of the connectors of the magnetosome particles to the filament can lead us to improve our model to a more elaborate model of magnetosome chain structure and amend our knowledge of the mechanics and stability of this structure. We hope that our model opens the way for more sophisticated models of the magnetosome chain in magnetotactic bacteria.

In addition, we aim to use the simulated spectra of magnetosome chains along with the spectra obtained from FMR spectroscopy experiments on bacteria *in vivo* to understand the origin of the ferromagnetic resonance spectra of magnetosome chains. The nano-size magnetosome particles can be extracted from disrupted cells of magnetotactic bacteria by application of an external magnetic field and because of their organic membrane, the magnetosome particles can be easily dispersed in aqueous solutions [109]. This quality along with their magnetic characteristic have been exploited in various biotechnological applications such as cell separation, immunoassays and drug delivery [110, 111]. We hope our study of magnetostatic interactions between magnetosome particles and between magnetosome particles and applied magnetic field facilitates the application of bacterial magnetic particles.



# Appendix A

## supplementary discussions of chapter 2

### A.1 Derivations of the equations discussed in chapter 2

#### A.1.1 Straight chain energy

We presented the equilibrium energy for a straight chain of magnetic dipoles in Eq. (3.4). Here, we obtain this equation in more detail.

$$\begin{aligned} E_{\text{lin}} &= - \sum_{i=1}^N \sum_{j>i}^N \frac{\mu_0 m^2}{4\pi r_{ij}^3} (3\cos^2(\theta) - 1) \Big|_{\theta=0} = - \sum_{i=1}^N \sum_{j>i}^N \frac{\mu_0 2m^2}{4\pi r_{ij}^3} \\ &= - \sum_{i=1}^N \sum_{j>i}^N \frac{\mu_0}{4\pi} \frac{2m^2}{|j-i|^3 l^3} \Big|_{|j-i|=n} \quad (\text{A.1}) \\ &= -N\epsilon \sum_{n=1}^{N-1} \frac{(1 - \frac{n}{N})}{n^3}. \end{aligned}$$

## A.1.2 Magnetic bending rigidity

In this appendix, we describe the calculation of the magnetic bending rigidity in more details. To evaluate the interaction energy, we express the angles between the dipole moments and between dipoles and their distance in terms of  $\phi$  and  $\theta$ ,

$$\begin{aligned}\angle(m_i, m_j) &= |i - j|\varphi, \\ \angle(m_i, r_{ij}) &= \theta - \frac{(|i - j| - 1)}{2}\varphi, \\ \angle(m_j, r_{ij}) &= \theta + \frac{(|i - j| + 1)}{2}\varphi.\end{aligned}\tag{A.2}$$

Likewise, the distances  $r_{ij}$  are expressed as

$$r_{ij} = 2R \sin \frac{|i - j|\varphi}{2}.\tag{A.3}$$

$$\begin{aligned}
E_{\text{magn}} &= - \sum_{i=1}^N \sum_{j>i}^N \frac{\mu_0}{4\pi} \frac{1}{r_{ij}^3} \left( \frac{3(\mathbf{m}_i \cdot \mathbf{r}_{ij})(\mathbf{m}_j \cdot \mathbf{r}_{ij})}{r_{ij}^2} - \mathbf{m}_i \cdot \mathbf{m}_j \right) \\
&= - \frac{\mu_0}{4\pi} \sum_{i=1}^N \sum_{j>i}^N \frac{m_i m_j}{(2R \sin \frac{|i-j|\varphi}{2})^3} \left( + 3 \cos\left(\theta - \frac{(|i-j|-1)\varphi}{2}\right) \cos\left(\theta + \frac{(|i-j|+1)\varphi}{2}\right) \right. \\
&\quad \left. - \cos(|i-j|\varphi) \right) \\
&= - \frac{\mu_0}{4\pi} \frac{m^2}{(2R)^3} \left( + \underbrace{\frac{1}{\sin^3(\frac{\varphi}{2})} (3 \cos(\theta) \cos(\theta + \varphi) - \cos(\varphi))}_{(N-1) \text{ times}} \right. \\
&\quad \left. + \underbrace{\frac{1}{\sin^3(\frac{2\varphi}{2})} (3 \cos(\theta - \frac{\varphi}{2}) \cos(\theta + \frac{3\varphi}{2}) - \cos(2\varphi))}_{(N-2) \text{ times}} \right. \\
&\quad \left. + \dots \right. \\
&\quad \left. + \underbrace{\frac{1}{\sin^3(\frac{(N-1)\varphi}{2})} (3 \cos(\theta - \frac{(N-2)\varphi}{2}) \cos(\theta + \frac{N\varphi}{2}) - \cos((N-1)\varphi))}_{(N-(N-1)) \text{ times}} \right) \\
&= - \frac{\mu_0}{4\pi} \frac{m^2}{(2R)^3} \left( \sum_n^{N-1} \frac{N-n}{\sin^3(\frac{n\varphi}{2})} \left( 3 \cos\left(\theta - \frac{(n-1)\varphi}{2}\right) \cos\left(\theta + \frac{(n+1)\varphi}{2}\right) - \cos(n\varphi) \right) \right) \\
\Rightarrow E_{\text{magn}}(\theta, \varphi) &= -N\epsilon \sum_{n=1}^{N-1} \frac{(1 - \frac{n}{N})}{4 \left( \frac{\sin(n\varphi/2)}{\sin(\varphi/2)} \right)^3} \left( 3 \cos(2\theta + \varphi) + \cos(n\varphi) \right), \tag{A.4}
\end{aligned}$$

In the equilibrium state, the orientation of the dipoles is such that the energy is minimal, thus we determine  $\theta$  as a function of  $\varphi$  and thus of the chain curvature, by minimizing the energy,

$$E_{\text{magn}}(\theta, \varphi) = -N\epsilon \sum_{n=1}^{N-1} \frac{(1 - \frac{n}{N})}{4 \left( \frac{\sin(n\varphi/2)}{\sin(\varphi/2)} \right)^3} \left( 3 \cos(2\theta + \varphi) + \cos(n\varphi) \right)$$

$$\begin{aligned}
\frac{\partial}{\partial \theta} E_{\text{magn}}(\theta, \varphi) &= -N\epsilon \sum_{n=1}^{N-1} \frac{(1 - \frac{n}{N})}{4 \left( \frac{\sin(n\varphi/2)}{\sin(\varphi/2)} \right)^3} \left( -6 \sin(2\theta + \varphi) \right) \\
&= 0 \\
\Rightarrow \sum_{n=1}^{N-1} \frac{(1 - \frac{n}{N})}{4 \left( \frac{\sin(n\varphi/2)}{\sin(\varphi/2)} \right)^3} \times \sin(2\theta + \varphi) &= 0 \\
\Rightarrow \sin(2\theta + \varphi) = 0 \quad \Rightarrow \quad \theta &= \frac{k\pi}{2} - \frac{\varphi}{2}
\end{aligned}$$

To ensure that at this angle the energy is minimum, we look at the second derivative of the energy,

$$\begin{aligned}
\frac{\partial^2}{\partial \theta^2} E_{\text{magn}}(\theta = \frac{k\pi}{2} - \frac{\varphi}{2}) &= -N\epsilon \sum_{n=1}^{N-1} \frac{(1 - \frac{n}{N})}{4 \left( \frac{\sin(n\varphi/2)}{\sin(\varphi/2)} \right)^3} \times \left( -12 \cos(2k\pi) \right) > 0 \\
&\Rightarrow \theta_{\text{min}} = \frac{k\pi}{2} - \frac{\varphi}{2},
\end{aligned} \tag{A.5}$$

this leads to  $\theta = -\frac{\varphi}{2}$ , i.e. the magnetic dipoles orient in tangential direction with respect to the curvature circle, the tangential orientation is also valid for more general shapes of chains of magnetic dipoles as shown recently in [112]. In this case, the energy is given by

$$E_{\text{magn}} = -N\epsilon \sum_{n=1}^{N-1} \frac{(1 - \frac{n}{N})}{4 \left( \frac{\sin(n\varphi/2)}{\sin(\varphi/2)} \right)^3} \left( 3 + \cos(n\varphi) \right). \tag{A.6}$$

Next, we use the Taylor expansion for small curvature,

$$\begin{aligned}
E_{\text{magn}} &= -N\epsilon \sum_{n=1}^{N-1} \frac{(1 - \frac{n}{N})}{4 \left( \frac{\sin(\frac{n\varphi}{2})}{\sin(\frac{\varphi}{2})} \right)^3} (3 + \cos(n\varphi)) \\
&= -N\epsilon \sum_{n=1}^{N-1} \frac{(1 - n/N)}{4 \sin^3(\frac{n\varphi}{2})} \sin^3(\frac{\varphi}{2}) (3 + \cos(n\varphi)) \\
&\approx -\frac{N\epsilon}{4} \sum_{n=1}^{N-1} \frac{(1 - \frac{n}{N})}{\left( (\frac{n\varphi}{2})^3 - \frac{1}{2}(\frac{n\varphi}{2})^5 \right)} \times \left( (\frac{\varphi}{2})^3 - \frac{1}{2}(\frac{\varphi}{2})^5 \right) \times \left( 3 + 1 - \frac{(n\varphi)^2}{2} \right) + \dots \\
&\approx -\frac{N\epsilon}{4} \sum_{n=1}^{N-1} \frac{(1 - \frac{n}{N})}{n^3} \times \left( 1 + \frac{1}{2}(\frac{n\varphi}{2})^2 + (\frac{1}{2}(\frac{n\varphi}{2})^2)^2 \right) \times \left( 1 - \frac{1}{2}(\frac{\varphi}{2})^2 \right) \times \left( 4 - \frac{(n\varphi)^2}{2} \right) + \dots \\
&\approx -\frac{N\epsilon}{4} \sum_{n=1}^{N-1} \frac{(1 - \frac{n}{N})}{n^3} \times \left( 4 - 2(\frac{\varphi}{2})^2 \right) \\
&= -N\epsilon \sum_{n=1}^{N-1} \frac{(1 - \frac{n}{N})}{n^3} \times \left( 1 - \frac{1}{2}(\frac{\varphi}{2})^2 \right).
\end{aligned} \tag{A.7}$$

In this equation,  $\varphi$  is a function of the curvature,  $l/R$ ,

$$\sin(\frac{\varphi}{2}) = \frac{l}{R} \Rightarrow \varphi = 2 \arcsin(\frac{l}{2R}) \approx \frac{l}{R} + \frac{1}{3}(\frac{l}{R})^3 + \dots,$$

$$\begin{aligned}
E_{\text{magn}} &\approx -N\epsilon \sum_{n=1}^{N-1} \frac{(1 - \frac{n}{N})}{n^3} \times \left( 1 - \frac{1}{2}(\frac{l}{2R})^2 \right) \\
&= E_{\text{lin}} \left( 1 - \frac{1}{2}(\frac{l}{2R})^2 \right),
\end{aligned} \tag{A.8}$$

Here the first term is the linear chain energy and the second term represents the contribution from bending with a magnetic bending rigidity of

$$\kappa_{\text{magn}} = \frac{\epsilon l}{4} \sum_{n=1}^{N-1} \frac{(1 - \frac{n}{N})}{n^3} \approx \frac{\epsilon l}{4} \zeta(3) \simeq 0.3\epsilon l. \tag{A.9}$$

### A.1.3 Nearest–neighbor Interactions

If we consider only nearest–neighbor interactions, only the term with  $n = 1$  remains in Eq. (A.8). This leads to

$$E^{\text{nn}} \approx -N\epsilon \left(1 - \frac{1}{N}\right) + \frac{1}{8}N\epsilon \left(1 - \frac{1}{N}\right) \left(\frac{l}{R}\right)^2. \quad (\text{A.10})$$

with the energy  $E_{\text{lin}}$  of the linear chain given by Eq. (3.4) and the magnetic bending rigidity

$$\kappa_{\text{magn}}^{\text{nn}} = \frac{\epsilon l}{4} \left(1 - \frac{1}{N}\right). \quad (\text{A.11})$$

### A.1.4 Energy difference between linear chain and closed ring

In section 2.3.3, we discussed the energy difference between a straight chain and a closed ring. Here, we elaborate on the derivation of the Eq. (A.10) which demonstrates the decay of the difference between energies of these two configurations with the increase in the number of particles.

$$E_{\text{lin}} = -N\epsilon \sum_{n=1}^{N-1} \frac{(1 - n/N)}{n^3},$$

$$E_{\text{ring}} = -N\epsilon \sum_{n=1}^{N-1} \frac{(1 - n/N)}{4 \left(\frac{\sin(\frac{n\pi}{N})}{\sin(\frac{\pi}{N})}\right)^3} \left(3 + \cos\left(\frac{2}{N}\right) + 3\right).$$

Using the Taylor expansions for  $\cos(\frac{2\pi n}{N})$  and  $\left(\frac{\sin(\frac{n\pi}{N})}{\sin(\frac{\pi}{N})}\right)^3$ , we obtain

$$E_{\text{ring}} - E_{\text{lin}} \approx -N\epsilon \sum_{n=1}^{n=N-1} \frac{(1 - n/N)}{n^3} \left(1 - \frac{n^2 \pi^2}{2N^2}\right) - 1$$

$$= -\frac{\pi^2 \epsilon}{2N} \sum_{n=1}^{N-1} \frac{1 - n/N}{n}. \quad (\text{A.12})$$

## A.2 Effect of the temperature on the rigidity of magnetosome chains

In chapter 2, we studied the bending stiffness of magnetosome chains. We calculated analytically the contribution of magnetic interactions to the bending rigidity at  $T = 0^\circ\text{K}$ . In this appendix, we look at the effect of the temperature on the bending rigidity and on the persistence length of magnetosome chains.

To that end, we apply the model of linear and bent magnetosome chain structures, introduced in chapter 2, and combine this model with Monte Carlo simulations at different temperatures  $30^\circ\text{K}$ ,  $300^\circ\text{K}$  and  $3000^\circ\text{K}$ . As results of our simulation, we obtain for each temperature the magnetic interaction energies of linear and bent structures of the magnetosome chain. Placing these energies into the Eq. (A.8), the bending energy contribution and the corresponding bending rigidity are calculated. Subsequently, we use the Eq. (2.8) to obtain the persistence length for each temperature.

Fig. A.1 presents the results of our simulations for bending rigidity and persistence length of a magnetosome chain at different temperatures as a function of the bending curvature,  $\frac{l}{R}$ . In our simulations, we consider a magnetosome chain of 20 magnetite particles with radius  $r = 25$  nm and the membrane thickness 5 nm.  $l$  is the distance between neighbouring magnetosome particles and  $R$  is the radius of the curve on which magnetosome particles are fixed.

Our results indicate that the bending rigidity is not strongly affected by the temperature. However, as expected, the persistence length increases with the decrease of the temperature. In other words, the magnetosome chain becomes more straight under decreasing the temperature (cooling).

Negative values in Fig. A.1 arise due to the thermal fluctuations of magnetic moments at higher temperatures. At these temperatures, thermal fluctuations oppose the alignment of magnetic dipoles to the axis of the linear chain and as a result, the energy of the linear chain structure may not be the minimum energy and lower than the energy of the bent chain structure and the negative bending energy and bending

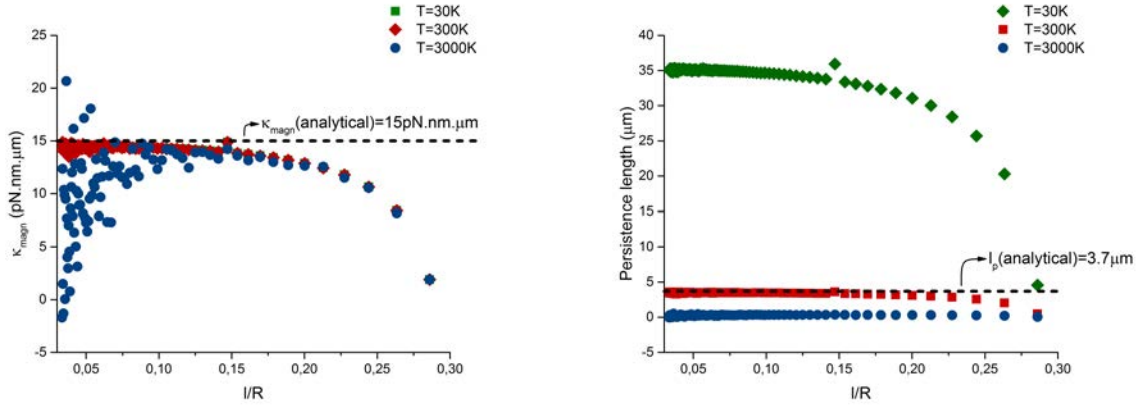


Figure A.1: Bending rigidity (left) and persistence length (right) of the magnetosome chain as a function of  $\frac{l}{R}$  for temperatures 30°K, 300°K and 3000°K. The dashed lines demonstrate the values of the bending rigidity and the persistence length at  $T=0^\circ$  derived from analytical calculations in chapter 2.

rigidity emerge.



# Appendix B

## Supplementary discussions of chapter 3

### B.1 Critical angle of rupture

In section , we obtained at the critical angle where  $E_{binding} > E_{elasticity}$  and as a result, the particle unbinds. In this appendix, we derive this critical angle in more detail.

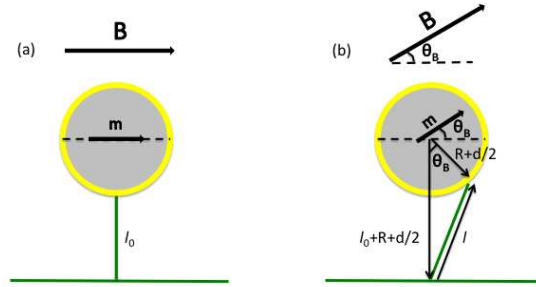


Figure B.1: The torque exerted by the external field pulls the linker of the particle to the filament with relaxed length  $l_0$  to the length  $l$ .

$$E_{elasticity} = +\frac{1}{2}k_l(l - l_0)^2$$

$$l^2 = \left(R + \frac{d}{2}\right)^2 + \left(l_0 + R + \frac{d}{2}\right)^2 + 2l_0\left(R + \frac{d}{2}\right)\cos(\theta)$$

$E_{binding} > E_{elasticity}$  leads to,

$$\begin{aligned} & \left( \left( R + \frac{d}{2} \right)^2 + \left( l_0 + R + \frac{d}{2} \right)^2 + 2l_0 \left( R + \frac{d}{2} \right) \cos(\theta) \right)^{\frac{1}{2}} - l_0 \geq \left( -\frac{2E_{binding}}{k_l} \right) \\ \Rightarrow \quad \cos(\theta) & \geq \frac{R + \frac{d}{2}}{2\left( R + \frac{d}{2} + l_0 \right)} + \frac{R + \frac{d}{2} + l_0}{2\left( R + \frac{d}{2} \right)} - \frac{\left( \sqrt{-\frac{2E_{binding}}{k_l}} + l_0 \right)^2}{2\left( R + \frac{d}{2} \right) \times \left( R + \frac{d}{2} + l_0 \right)} \end{aligned}$$

## B.2 Magnetosome chains under weak external fields

In this appendix, we present the behaviour of different energy contributions in magnetosome chain during application of an external field with the strength  $B = 35$  mT which is lower than the threshold needed for the chain disruption. In this case, the strength of the magnetic field–dipole interaction is not sufficient to rotate the dipoles to the angle where the particles begin to repel each other and therefore the magnetosome chain does not break into smaller pieces.

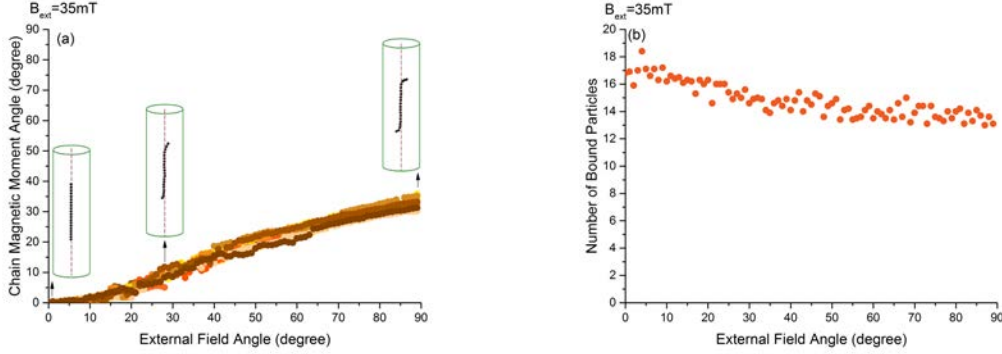


Figure B.2: Figure (a) shows the orientation of the chain magnetic moment in different angles of the external field. Figure (b) presents the change in the average number of magnetosome particles bound to the filament during the application of the external. In each plot, different colours represent 10 trajectories extracted from Monte Carlo simulations.

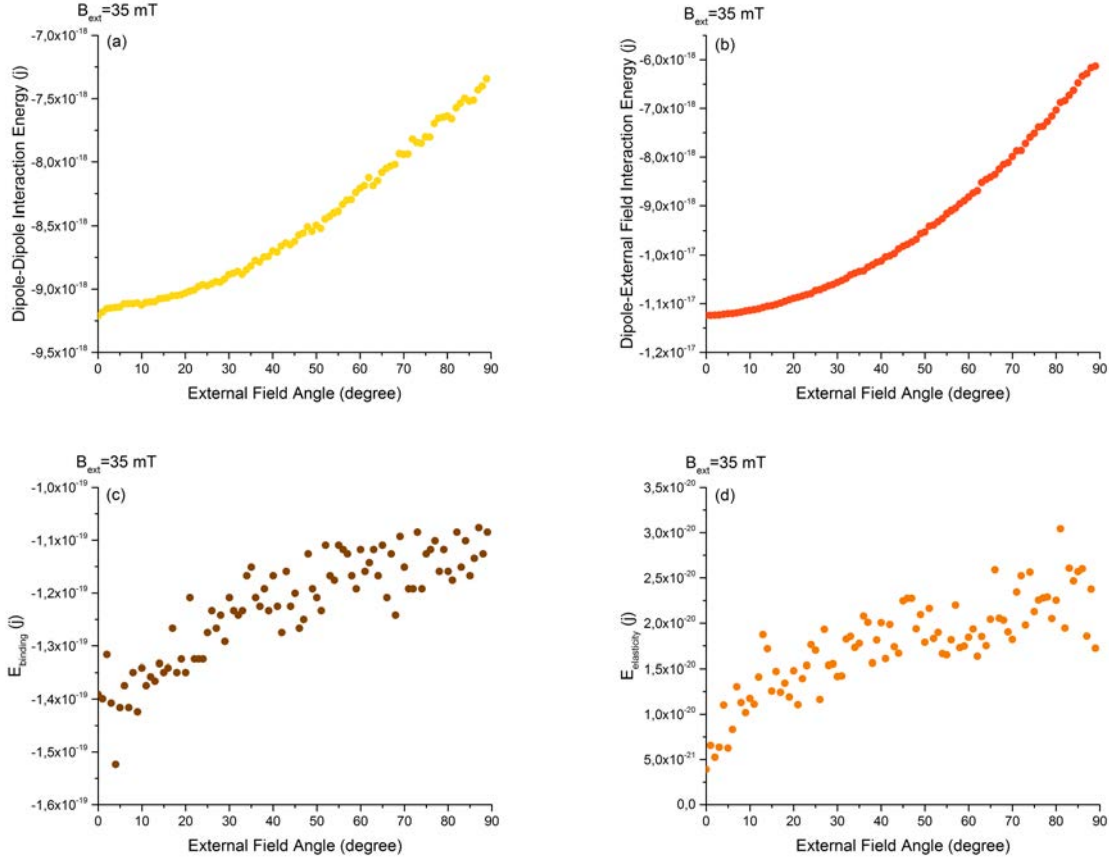


Figure B.3: The external field of 35mT disorients the dipoles from their initial linear orientation along the filament and therefore the dipole–dipole interaction increases. Changing the angle of the external field to higher angles increases the elasticity of the attached particles. As the strength of the external field is below the threshold needed to rotate the dipoles to the critical point of rupture where dipoles begin to repel each other, in contrast to the case of higher external field strengths, the chain is not disrupted and dipole–dipole interactions, the external field–dipole interactions and the elastic energy of the linkers do not decrease back to the lower values.

### B.3 Dipole–dipole magnetic force

The force emanating from dipole–dipole interactions between two magnetic dipoles  $\mathbf{m}_i$  and  $\mathbf{m}_j$  is

$$\mathbf{F}_{dd} = \frac{3\mu_0}{4\pi r_{ij}^5} \left( (\mathbf{m}_i \cdot \mathbf{r}_{ij})\mathbf{m}_j + (\mathbf{m}_j \cdot \mathbf{r}_{ij})\mathbf{m}_i + (\mathbf{m}_i \cdot \mathbf{m}_j)\mathbf{r}_{ij} - \frac{5(\mathbf{m}_i \cdot \mathbf{r}_{ij})(\mathbf{m}_j \cdot \mathbf{r}_{ij})}{r_{ij}^2}\mathbf{r}_{ij} \right), \quad (\text{B.1})$$

where  $\mu_0 = 4\pi \times 10^{-7} \text{NA}^{-2}$  is the vacuum permeability and the  $\mathbf{r}_{ij}$  is the distance vector between dipoles, with  $r_{ij} = |\mathbf{r}_{ij}|$ .

For two fixed dipoles with angle  $\theta$  relative to the direction of the vector  $\mathbf{r}_{ij}$  and  $m_i = m_j = m$ , the Eq. (B.1) takes the form bellow,

$$\mathbf{F}_{\text{dd}} = \frac{3\mu_0 m^2}{4\pi r_{ij}^4} (2\cos(\theta) + 1 - 5\cos^2(\theta)) \hat{r}_{ij}. \quad (\text{B.2})$$

Fig. B.4 shows the behaviour of the dipole–dipole force in different orientations of the dipoles relative to the direction of the vector connecting them. From  $0^\circ$  to  $\sim 46^\circ$ , the two dipoles attract each other but as the angle rises to higher values dipoles begin to repel each other.

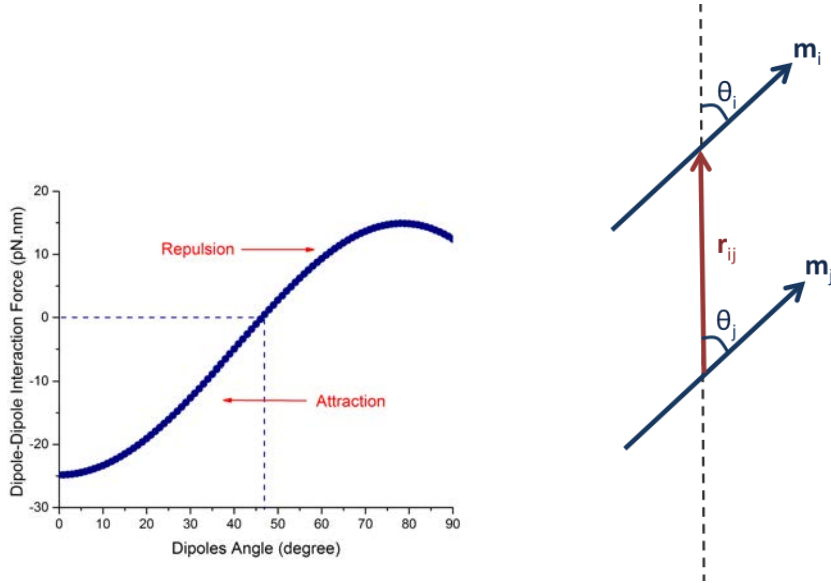


Figure B.4: Plot presents the change in the force between two dipoles from repulsion to attraction with increasing the angles of the dipoles relative to the direction of the vector connecting them.

## B.4 Energy contributions in a magnetosome chain of greigite particles

In section 3.4.2, we explained how the process of chain disruption and the resulting structure differ in the case of lower dipole–dipole interactions. We presented the change in the behaviour of the chain magnetic moment in different angles of the external field of  $B = 50\text{mT}$  relative to the direction of the filament.

Here, we show how the number of bound particles to the filament and different energy contributions alter during the application of the external field,  $B = 50\text{mT}$ , in different angles of the field relative to the direction of the filament. Fig. B.6 indicates that early after the critical point the dipoles follow the external field freely and consequently the external field–dipole interaction energy and the dipole–dipole interaction energy fall and do not change anymore.

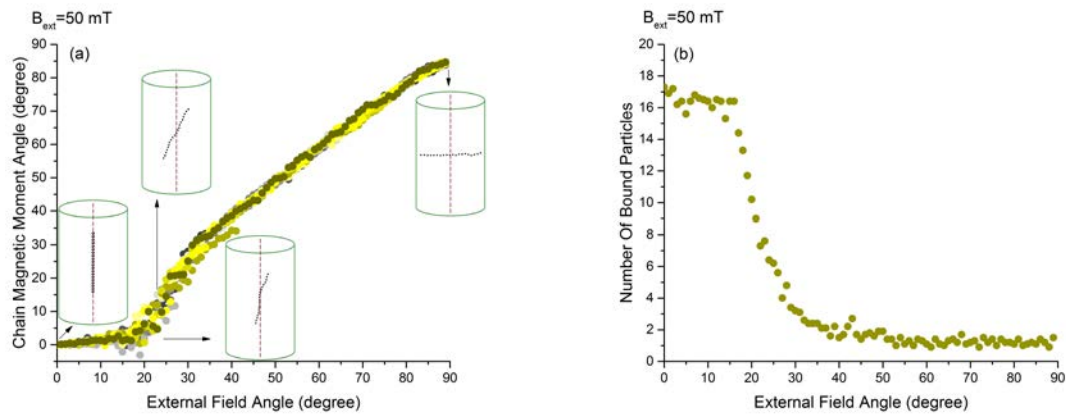


Figure B.5: Due to feeble dipole–dipole interactions, early after the critical point, dipoles align with the external field (a), the elasticity of linkers to the filament increases and as a result they break and the number of bound particles (b) drops.

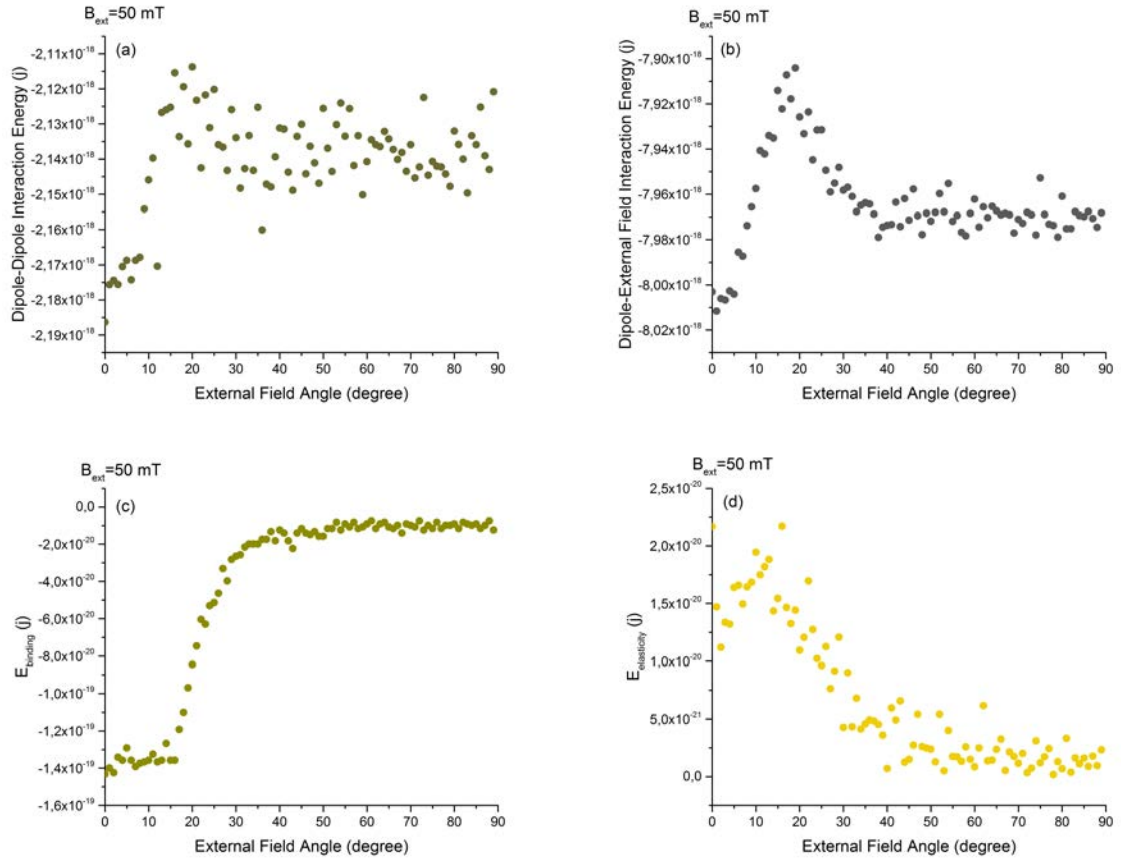


Figure B.6: The behaviour of dipole–dipole interactions (a), external magnetic field–dipole interactions (b), binding (c) and elastic (d) energies for a chain with  $N = 20$  greigite particles in different angles of the external magnetic field of  $B = 50 \text{ mT}$  relative to the direction of the filament.

# Appendix C

## Supplementary discussions of chapter 4

### C.1 Derivatives of the total energy

Derivatives of the total energy of the particle  $i$  in respect to its polar and azimuthal angles  $\theta_i$  and  $\varphi_i$

- First derivative with respect to  $\theta_i$  :

$$\begin{aligned}\partial_{\theta_i} E^i &= \partial_{\theta_i} E_{\text{dd}}^i + \partial_{\theta_i} E_{\text{B}}^i, \\ \partial_{\theta_i} E_{\text{dd}}^i &= -\frac{\mu_0}{4\pi} \sum_{j=1}^N \frac{m^2}{r_{ij}^3} (-2 \cos(\theta_j) \sin(\theta_i) - \cos(\theta_i) \cos(\varphi_i - \varphi_j) \sin(\theta_j)), \quad (\text{C.1})\end{aligned}$$

$$\partial_{\theta_i} E_{\text{B}}^i = -mB (\cos(\theta_i) \cos(\varphi_B - \varphi_i) \sin(\theta_B) - \cos(\theta_B) \sin(\theta_i)).$$

- First derivative with respect to  $\varphi_i$  :

$$\begin{aligned}\partial_{\varphi_i} E^i &= \partial_{\varphi_i} E_{\text{dd}}^i + \partial_{\varphi_i} E_{\text{B}}^i, \\ \partial_{\varphi_i} E_{\text{dd}}^i &= -\frac{\mu_0}{4\pi} \sum_{j=1}^N \frac{m^2}{r_{ij}^3} (\sin(\theta_i) \sin(\theta_j) \sin(\varphi_i - \varphi_j)), \quad (\text{C.2})\end{aligned}$$

$$\partial_{\varphi_i} E_{\text{B}}^i = -mB (\sin(\theta_B) \sin(\theta_i) \sin(\varphi_B - \varphi_i)).$$

- Second derivatives with respect to  $\theta_i$  :

$$\begin{aligned}\partial_{\theta_i\theta_i}E^i &= \partial_{\theta_i\theta_i}E_{\text{dd}}^i + \partial_{\theta_i\theta_i}E_{\text{B}}^i, \\ \partial_{\theta_i\theta_i}E_{\text{dd}}^i &= -\frac{\mu_0}{4\pi} \sum_{j=1}^N \frac{m^2}{r_{ij}^3} (-2 \cos(\theta_i) \cos(\theta_j) + \cos(\varphi_i - \varphi_j) \sin(\theta_i) \sin(\theta_j)), \quad (\text{C.3}) \\ \partial_{\theta_i\theta_i}E_{\text{B}}^i &= -mB (-\cos(\theta_B) \cos(\theta_i) - \cos(\varphi_B - \varphi_i) \sin(\theta_B) \sin(\theta_i)),\end{aligned}$$

$$\begin{aligned}\partial_{\theta_i\varphi_i}E^i &= \partial_{\theta_i\varphi_i}E_{\text{dd}}^i + \partial_{\theta_i\varphi_i}E_{\text{B}}^i, \\ \partial_{\theta_i\varphi_i}E_{\text{dd}}^i &= -\frac{\mu_0}{4\pi} \sum_{j=1}^N \frac{m^2}{r_{ij}^3} (\cos(\theta_i) \sin(\theta_j) \sin(\varphi_i - \varphi_j)), \quad (\text{C.4}) \\ \partial_{\theta_i\varphi_i}E_{\text{B}}^i &= -mB (\cos(\theta_i) \sin(\theta_B) \sin(\varphi_B - \varphi_i)).\end{aligned}$$

- Second derivatives with respect to  $\varphi_i$  :

$$\begin{aligned}\partial_{\varphi_i\varphi_i}E^i &= \partial_{\varphi_i\varphi_i}E_{\text{dd}}^i + \partial_{\varphi_i\varphi_i}E_{\text{B}}^i, \\ \partial_{\varphi_i\varphi_i}E_{\text{dd}}^i &= -\frac{\mu_0}{4\pi} \sum_{j=1}^N \frac{m^2}{r_{ij}^3} (\cos(\varphi_i - \varphi_j) \sin(\theta_i) \sin(\theta_j)), \quad (\text{C.5}) \\ \partial_{\varphi_i\varphi_i}E_{\text{B}}^i &= +mB (\cos(\varphi_i - \varphi_j) \sin(\theta_B) \sin(\theta_i)).\end{aligned}$$

## C.2 Resonance field at different orientations of the applied field

Due to the dependence of the magnetocrystalline anisotropy on orientation, resonance takes place in different field strength for different orientations of the applied field. Fig. C.1 shows the absorption for (a)  $\varphi_{\text{Bext}} = 45^\circ$  and (b)  $\varphi_{\text{Bext}} = 120^\circ$  for different polar angles  $\theta_{\text{Bext}} = 45^\circ$ ,  $\theta_{\text{Bext}} = 60^\circ$  and  $\theta_{\text{Bext}} = 90^\circ$ . Considering the corresponding magnetocrystalline energy for each orientation (see Fig. 4.5(c)), resonance occurs at lower field values for orientations with lower magnetocrystalline energy.



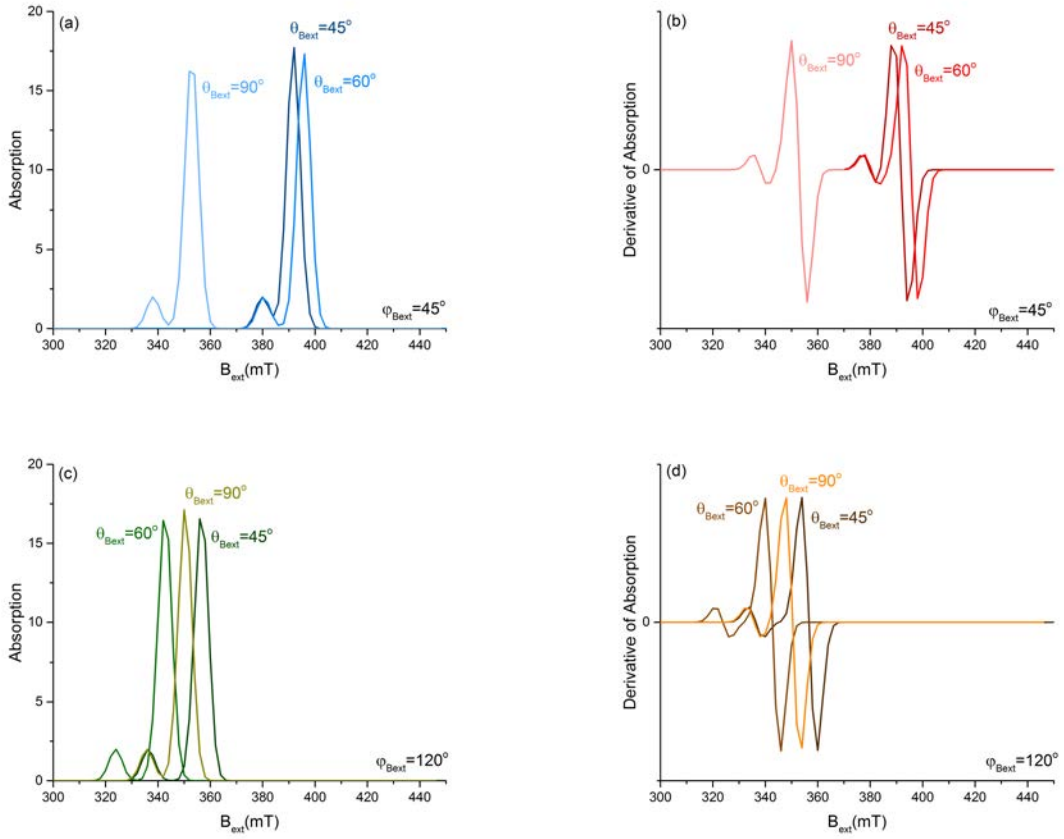


Figure C.1: Resonance spectrum for different orientation of the external field, relative to the direction of the magnetosome chain, emerges at different field strength.

### C.3 Effect of dipole–dipole interactions on the resonance field

If we look at the absorption of magnetosome chain, we observe two major peaks, Fig. 4.4(b, c). The first peak, at  $B_{ext} = 380$  mT, represents the resonance field for particles at two ends of the chain while the second peak, at  $B_{ext} = 392$  mT represents the one for the particles in the middle of the chain. The ground for the occurrence of the resonance at lower applied field for particles at two ends is that due to having one neighbour less than the particles in the middle of the chain, these particles are constrained to weaker dipole–dipole interactions. This effect of dipole–dipole interactions is also detected in the resonance field map of particles with different positions

within the chain, see Fig. C.2. In FMR simulations based on the ellipsoid model for magnetosome chains, these interactions are represented by a shape anisotropy function. This description can not account for the differences in magnetic orientations between particles, as the magnetisation is taken to be homogeneous throughout the ellipsoid [99].

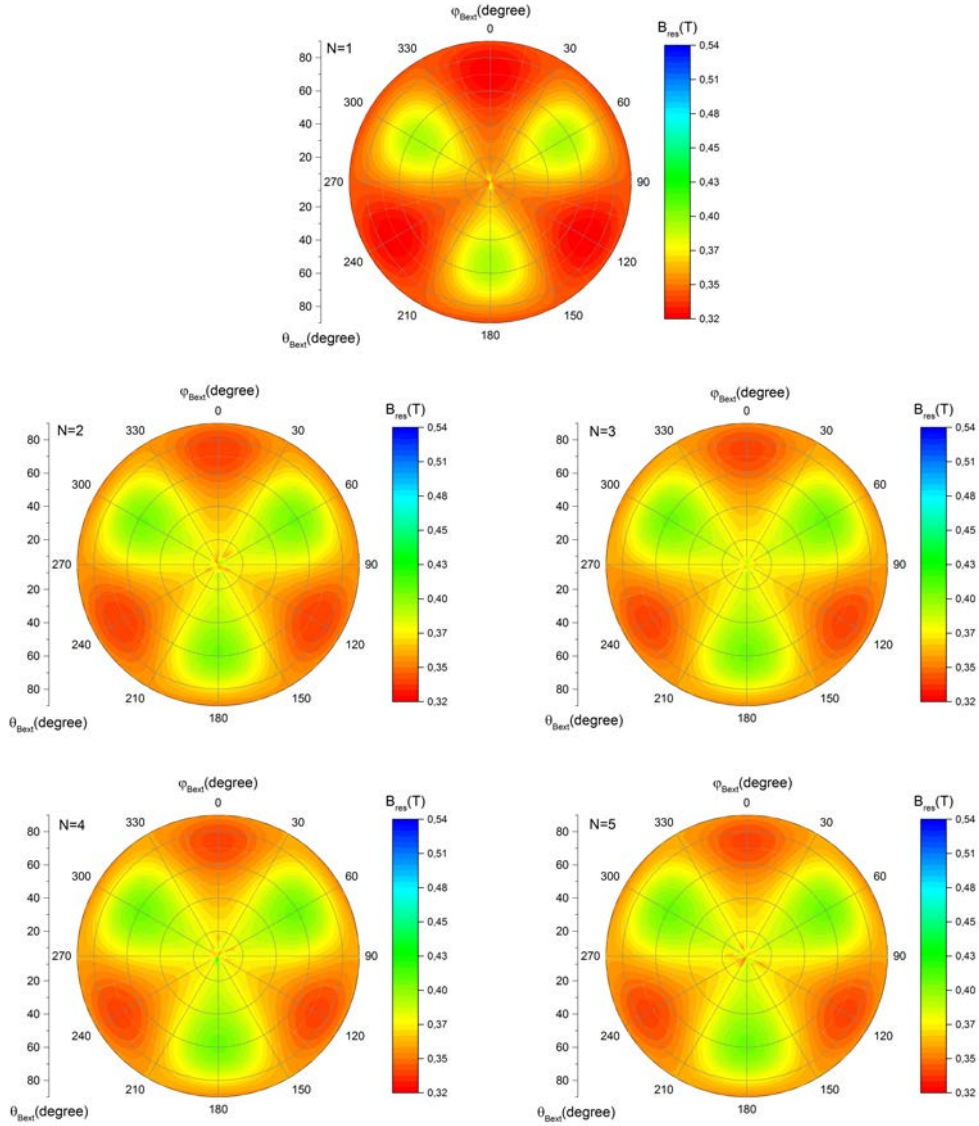


Figure C.2: The maps of the resonance field for the first five magnetosome particles at one end of a magnetosome chain of  $N = 20$  particles. The dissimilarity between the resonance field of the first particle and the rest of the particles owing to weaker dipole–dipole interactions is already noticeable between the map of two first particles. As the dipole–dipole interactions are fast decaying, there is no distinct difference between the behaviour of the resonance field of the particles in the middle. In other words, the dominant role in dipole–dipole interactions is played by two first neighbours, for more detail see chapter 2.



# Bibliography

- [1] Z. Gitai, “The new bacterial cell biology: moving parts and subcellular architecture,” *Cell*, vol. 120, pp. 577–86, Mar 2005.
- [2] J. A. Theriot, “Why are bacteria different from eukaryotes?,” *BMC Biol*, vol. 11, p. 119, 2013.
- [3] A. Komeili, H. Vali, T. J. Beveridge, and D. K. Newman, “Magnetosome vesicles are present before magnetite formation, and mama is required for their activation,” *Proc Natl Acad Sci U S A*, vol. 101, pp. 3839–44, Mar 2004.
- [4] M. Seufferheld, M. C. F. Vieira, F. A. Ruiz, C. O. Rodrigues, S. N. J. Moreno, and R. Docampo, “Identification of organelles in bacteria similar to acidocalcisomes of unicellular eukaryotes,” *J Biol Chem*, vol. 278, pp. 29971–8, Aug 2003.
- [5] A. Komeili, Z. Li, D. K. Newman, and G. J. Jensen, “Magnetosomes are cell membrane invaginations organized by the actin-like protein mamk,” *Science*, vol. 311, pp. 242–5, Jan 2006.
- [6] R. B. Frankel and D. A. Bazylinski, “How magnetotactic bacteria make magnetosomes queue up,” *Trends Microbiol*, vol. 14, pp. 329–31, Aug 2006.
- [7] R. Blakemore, “Magnetotactic bacteria.,” *Science*, vol. 190, pp. 377–379, Oct 1975.
- [8] R. P. Blakemore and R. B. Frankel, “Magnetic navigation in bacteria,” *Sci.Am.*, vol. 245, no. 6, pp. 58–62, 1981.

- [9] R. B. Frankel, “The discovery of magnetotactic/magnetosensitive bacteria,” *Chin. J. Oceanol. Limnol.*, vol. 27, pp. 1–2, February 2009.
- [10] S. Bellini, “On a unique behavior of freshwater bacteria,” *Chinese Journal of Oceanology and Limnology*, vol. 27, no. 1, pp. 3–5, 2009.
- [11] S. L. Simmons, S. M. Sievert, R. B. Frankel, D. A. Bazylinski, and K. J. Edwards, “Spatiotemporal distribution of marine magnetotactic bacteria in a seasonally stratified coastal salt pond,” *Appl. Environ. Microbiol.*, vol. 70, pp. 6230–6239, October 2004.
- [12] D. A. Bazylinski, R. B. Frankel, B. R. Heywood, S. Mann, J. W. King, P. L. Donaghay, and A. K. Hanson, “Controlled biomineralization of magnetite (Fe<sub>3</sub>O<sub>4</sub>) and greigite (Fe<sub>3</sub>S<sub>4</sub>) in a magnetotactic bacterium,” *Appl. Environ. Microbiol.*, vol. 61, pp. 3232–3239, September 1995.
- [13] R. B. Frankel, D. A. Bazylinski, M. S. Johnson, and B. L. Taylor, “Magnetotaxis in marine coccoid bacteria,” *Biophys J*, vol. 73, pp. 994–1000, Aug 1997.
- [14] D. A. Bazylinski and R. B. Frankel, “Magnetosome formation in prokaryotes,” *Nat Rev Microbiol*, vol. 2, pp. 217–30, Mar 2004.
- [15] M. Greenberg, K. Canter, I. Mahler, and A. Tornheim, “Observation of magnetoreceptive behavior in a multicellular magnetotactic prokaryote in higher than geomagnetic fields,” *Biophys. J.*, vol. 88, pp. 1496–1499, February 2005.
- [16] U. Lins, C. N. Keim, F. F. Evans, M. Farina, and P. R. Buseck, “Magnetite (Fe<sub>3</sub>O<sub>4</sub>) and greigite (Fe<sub>3</sub>S<sub>4</sub>) crystals in multicellular magnetotactic prokaryotes,” *Geomicrobiology Journal*, vol. 24, no. 1, pp. 43–50, 2007.
- [17] R. Blakemore, “Magnetotactic bacteria,” *Science*, vol. 190, no. 4212, pp. 377–379, 1975.

- [18] C. T. Lefèvre and D. A. Bazylinski, “Ecology, diversity, and evolution of magnetotactic bacteria,” *Microbiol Mol Biol Rev*, vol. 77, pp. 497–526, Sep 2013.
- [19] F. G. Rodgers, R. P. Blakemore, N. A. Blakemore, R. B. Frankel, D. A. Bazylinski, D. Maratea, and C. Rodgers, “Intercellular structure in a many-celled magnetotactic prokaryote,” *Arch. Microbiol.*, vol. 154, pp. 18–22, June 1990.
- [20] C. Jogler, M. Niebler, W. Lin, M. Kube, G. Wanner, S. Kolinko, P. Stief, A. J. Beck, D. De Beer, N. Petersen, Y. Pan, R. Amann, R. Reinhardt, and D. Schüler, “Cultivation-independent characterization of ‘candidatus magnetobacterium bavaricum’ via ultrastructural, geochemical, ecological and metagenomic methods,” *Environ Microbiol*, vol. 12, pp. 2466–78, Sep 2010.
- [21] F. Popp, J. P. Armitage, and D. Schüler, “Polarity of bacterial magnetotaxis is controlled by aerotaxis through a common sensory pathway,” *Nat Commun*, vol. 5, p. 5398, 2014.
- [22] B. L. Cox, R. Popa, D. A. Bazylinski, B. Lanoil, S. Douglas, A. Belz, D. L. Engler, and K. H. Nealson, “Organization and elemental analysis of p-, s-, and fe-rich inclusions in a population of freshwater magnetococci,” *Geomicrobiol. J.*, vol. 19, pp. 387–406, Jul-Aug 2002.
- [23] L. Liang, R. Rinaldi, and H. Schober, *Neutron applications in earth, energy and environmental sciences*. Neutron scattering applications and techniques, New York: Springer, 2009.
- [24] R. B. Frankel, R. P. Blakemore, F. F. DE Araujo, D. M. Esquivel, and J. Danon, “Magnetotactic bacteria at the geomagnetic equator,” *Science*, vol. 212, pp. 1269–70, Jun 1981.
- [25] R. P. Blakemore, R. B. Frankel, and A. J. Kalmijn, “South-seeking magnetotactic bacteria in the southern-hemisphere,” *Nature*, vol. 286, no. 5771, pp. 384–385, 1980.

- [26] C. B. Flies, H. M. Jonkers, D. de Beer, K. Bosselmann, M. E. Böttcher, and D. Schüler, “Diversity and vertical distribution of magnetotactic bacteria along chemical gradients in freshwater microcosms,” *FEMS Microbiol Ecol*, vol. 52, pp. 185–95, Apr 2005.
- [27] C. T. Lefèvre, A. Bernadac, K. Yu-Zhang, N. Pradel, and L.-F. Wu, “Isolation and characterization of a magnetotactic bacterial culture from the mediterranean sea,” *Environ Microbiol*, vol. 11, pp. 1646–57, Jul 2009.
- [28] T. T. Moench and W. A. Konetzka, “A novel method for the isolation and study of a magnetotactic bacterium,” *Arch Microbiol*, vol. 119, pp. 203–12, Nov 1978.
- [29] C. B. Flies, J. Peplies, and D. Schüler, “Combined approach for characterization of uncultivated magnetotactic bacteria from various aquatic environments,” *Appl Environ Microbiol*, vol. 71, pp. 2723–31, May 2005.
- [30] D. Schüler, “The biomineralization of magnetosomes in magnetospirillum gryphiswaldense,” *Int Microbiol*, vol. 5, pp. 209–14, Dec 2002.
- [31] D. Schüler, *Magnetoreception and magnetosomes in bacteria*, vol. 3 of *Microbiology monographs*. Berlin: Springer, 2007.
- [32] D. L. Balkwill, D. Maratea, and R. P. Blakemore, “Ultrastructure of a magnetotactic spirillum,” *J Bacteriol*, vol. 141, pp. 1399–408, Mar 1980.
- [33] T. Matsuda, J. Endo, N. Osakabe, A. Tonomura, and T. Ariei, “Morphology and structure of biogenic magnetite particles,” *Nature*, vol. 302, no. 5907, pp. 411–412, 1983.
- [34] S. Mann, R. B. Frankel, and R. P. Blakemore, “Structure, morphology and crystal-growth of bacterial magnetite,” *Nature*, vol. 310, no. 5976, pp. 405–407, 1984.
- [35] Y. A. Gorby, T. J. Beveridge, and R. P. Blakemore, “Characterization of the bacterial magnetosome membrane,” *J Bacteriol*, vol. 170, pp. 834–41, Feb 1988.



- [36] A. Scheffel, M. Gruska, D. Faivre, A. Linaroudis, J. M. Plitzko, and D. Schüler, “An acidic protein aligns magnetosomes along a filamentous structure in magnetotactic bacteria,” *Nature*, vol. 440, pp. 110–4, Mar 2006.
- [37] R. B. Frankel, R. P. Blakemore, and R. S. Wolfe, “Magnetite in freshwater magnetotactic bacteria,” *Science*, vol. 203, pp. 1355–6, Mar 1979.
- [38] S. Mann, N. H. C. Sparks, R. B. Frankel, D. A. Bazylinski, and H. W. Jannasch, “Biom mineralization of ferrimagnetic greigite ( $\text{Fe}_3\text{S}_4$ ) and iron pyrite ( $\text{FeS}_2$ ) in a magnetotactic bacterium,” *Nature*, vol. 343, pp. 258–261, January 1990.
- [39] D. A. Bazylinski, A. J. Garratt-Reed, and R. B. Frankel, “Electron microscopic studies of magnetosomes in magnetotactic bacteria,” *Microsc Res Tech*, vol. 27, pp. 389–401, Apr 1994.
- [40] S. Mann, N. H. Sparks, and R. G. Board, “Magnetotactic bacteria: microbiology, biom mineralization, palaeomagnetism and biotechnology,” *Adv Microb Physiol*, vol. 31, pp. 125–81, 1990.
- [41] M. R. McCartney, U. Lins, M. Farina, P. R. Buseck, and R. B. Frankel, “Magnetic microstructure of bacterial magnetite by electron holography,” *Eur. J. Mineral.*, vol. 13, pp. 685–689, Jul-Aug 2001.
- [42] M. Farina, B. Kachar, U. Lins, R. Broderick, and H. L. Debarros, “The observation of large magnetite ( $\text{Fe}_3\text{O}_4$ ) crystals from magnetotactic bacteria by electron and atomic-force microscopy,” *J. Microsc.-Oxf.*, vol. 173, pp. 1–8, January 1994.
- [43] U. Lins, M. R. McCartney, M. Farina, R. B. Frankel, and P. R. Buseck, “Crystal habits and magnetic microstructures of magnetosomes in coccoid magnetotactic bacteria,” *An Acad Bras Cienc*, vol. 78, pp. 463–74, Sep 2006.
- [44] S. Spring, U. Lins, R. Amann, K. H. Schleifer, L. C. Ferreira, D. M. Esquivel, and M. Farina, “Phylogenetic affiliation and ultrastructure of uncultured magnetic bacteria with unusually large magnetosomes,” *Arch Microbiol*, vol. 169, pp. 136–47, Feb 1998.

- [45] A. Aharoni, *Introduction to the theory of ferromagnetism*, vol. 109. Oxford University Press, 2000.
- [46] R. B. Frankel, “Magnetic guidance of organisms,” *Annu Rev Biophys Bio*, vol. 13, pp. 85–103, 1984.
- [47] D. Faivre and D. Schüler, “Magnetotactic bacteria and magnetosomes,” *Chem Rev*, vol. 108, pp. 4875–98, Nov 2008.
- [48] R. B. Proksch, T. E. Schaffer, B. M. Moskowitz, E. D. Dahlberg, D. A. Bazylinski, and R. B. Frankel, “Magnetic force microscopy of the submicron magnetic assembly in a magnetotactic bacterium,” *Appl. Phys. Lett.*, vol. 66, pp. 2582–2584, May 1995.
- [49] R. E. Dunin-Borkowski, M. R. McCartney, R. B. Frankel, D. A. Bazylinski, M. Posfai, and P. R. Buseck, “Magnetic microstructure of magnetotactic bacteria by electron holography,” *Science*, vol. 282, pp. 1868–1870, December 1998.
- [50] R. B. Frankel and R. P. Blakemore, “Navigational compass in magnetic bacteria,” *J. Magn. Magn. Mater.*, vol. 15-8, no. JAN-, pp. 1562–1564, 1980.
- [51] R. Nadkarni, S. Barkley, and C. Fradin, “A comparison of methods to measure the magnetic moment of magnetotactic bacteria through analysis of their trajectories in external magnetic fields,” *PLoS One*, vol. 8, no. 12, p. e82064, 2013.
- [52] X. Zhu, X. Ge, N. Li, L.-F. Wu, C. Luo, Q. Ouyang, Y. Tu, and G. Chen, “Angle sensing in magnetotaxis of magnetospirillum magneticum amb-1,” *Integr Biol (Camb)*, vol. 6, pp. 706–13, Jul 2014.
- [53] A. P. Philipse and D. Maas, “Magnetic colloids from magnetotactic bacteria: chain formation and colloidal stability,” *Langmuir*, vol. 18, no. 25, pp. 9977–9984, 2002.

- [54] E. Katzmann, F. D. Müller, C. Lang, M. Messerer, M. Winklhofer, J. M. Plitzko, and D. Schüler, “Magnetosome chains are recruited to cellular division sites and split by asymmetric septation,” *Mol Microbiol*, vol. 82, pp. 1316–29, Dec 2011.
- [55] A. Koernig, J. Dong, M. Bennet, M. Widdrat, J. Andert, F. D. Mueller, D. Schueler, S. Klumpp, and D. Faivre, “Probing the mechanical properties of magnetosome chains in living magnetotactic bacteria,” *Nano Lett.*, vol. 14, pp. 4653–4659, August 2014.
- [56] R. Messina, L. Abou Khalil, and I. Stankovic, “Self-assembly of magnetic balls: From chains to tubes,” *Phys. Rev. E*, vol. 89, p. 011202(R), January 2014.
- [57] V. P. Shcherbakov, M. Winklhofer, M. Hanzlik, and N. Petersen, “Elastic stability of chains of magnetosomes in magnetotactic bacteria,” *Eur. Biophys. J. Biophys. Lett.*, vol. 26, no. 4, pp. 319–326, 1997.
- [58] A. Cebers, “Flexible magnetic filaments,” *Curr. Opin. Colloid Interface Sci.*, vol. 10, pp. 167–175, October 2005.
- [59] V. P. Shcherbakov and M. Winklhofer, “Bending of magnetic filaments under a magnetic field,” *Phys. Rev. E*, vol. 70, p. 061803, December 2004.
- [60] S. Klumpp and D. Faivre, “Interplay of magnetic interactions and active movements in the formation of magnetosome chains,” *PLoS One*, vol. 7, no. 3, p. e33562, 2012.
- [61] E. Alphandéry, Y. Ding, A. T. Ngo, Z. L. Wang, L. F. Wu, and M. P. Pileni, “Assemblies of aligned magnetotactic bacteria and extracted magnetosomes: what is the main factor responsible for the magnetic anisotropy?,” *ACS Nano*, vol. 3, pp. 1539–47, Jun 2009.
- [62] E. Katzmann, A. Scheffel, M. Gruska, J. M. Plitzko, and D. Schüler, “Loss of the actin-like protein mamk has pleiotropic effects on magnetosome formation and chain assembly in magnetospirillum gryphiswaldense,” *Mol Microbiol*, vol. 77, pp. 208–24, Jul 2010.

- [63] A. Wei, T. Kasama, and R. E. Dunin-Borkowski, “Self-assembly and flux closure studies of magnetic nanoparticle rings,” *J. Mater. Chem.*, vol. 21, pp. 16686–16693, 2011.
- [64] Y. Xiong, J. Ye, X. Gu, and Q.-w. Chen, “Synthesis and assembly of magnetite nanocubes into flux-closure rings,” *J. Phys. Chem. C*, vol. 111, pp. 6998–7003, May 2007.
- [65] S. P. Li, D. Peyrade, M. Natali, A. Lebib, Y. Chen, U. Ebels, L. D. Buda, and K. Ounadjela, “Flux closure structures in cobalt rings,” *Phys Rev Lett*, vol. 86, pp. 1102–5, Feb 2001.
- [66] J. F. Stoz, S. B. R. Chang, and J. L. Kirschvink, “Magnetotactic bacteria and single-domain magnetite in hemipelagic sediments,” *Nature*, vol. 321, pp. 849–851, June 1986.
- [67] C. Goubault, P. Jop, M. Fermigier, J. Baudry, E. Bertrand, and J. Bibette, “Flexible magnetic filaments as micromechanical sensors,” *Phys. Rev. Lett.*, vol. 91, p. 260802, December 2003.
- [68] S. L. Biswal and A. P. Gast, “Mechanics of semiflexible chains formed by poly(ethylene glycol)-linked paramagnetic particles,” *Phys. Rev. E*, vol. 68, p. 021402, August 2003.
- [69] L. D. Landau, E. M. Lifshitz, A. M. Kosevich, and L. P. Pitaevskii, *Theory of elasticity*, vol. v. 7. Oxford: Pergamon Press, 3rd english ed., revised and enlarged by e.m. lifshitz, a.m. kosevich, and l.p. pitaevskii ed., 1986.
- [70] C. Jogler and D. Schüler, “Genomics, genetics, and cell biology of magnetosome formation,” *Annu Rev Microbiol*, vol. 63, pp. 501–21, 2009.
- [71] J. L. Barrat and J. F. Joanny, “Theory of polyelectrolyte solutions,” *Adv chem phys*, vol. 94, pp. 1–66, 1996.

- [72] D. Vella, E. du Pontavice, C. L. Hall, and A. Goriely, “The magneto-elastica: from self-buckling to self-assembly,” *Proc. R. Soc. A-Math. Phys. Eng. Sci.*, vol. 470, p. 20130609, February 2014.
- [73] M. Rubinstein and R. H. Colby, *Polymer physics*. Oxford: Oxford University Press, 2003.
- [74] N. A. Usov, M. L. Fdez-Gubieda, and J. M. Barandiaran, “Magnetostatic interactions in various magnetosome clusters,” *J. Appl. Phys.*, vol. 113, p. 023907, January 2013.
- [75] C. P. Bean and J. D. Livingston, “Superparamagnetism,” *Journal of Applied Physics*, vol. 30, no. 4, pp. S120–S129, 1959.
- [76] R. W. Chantrell, A. Bradbury, J. Popplewell, and S. W. Charles, “Particle cluster configuration in magnetic fluids,” *J. Phys. D-Appl. Phys.*, vol. 13, no. 7, pp. L119–L122, 1980.
- [77] W. J. Wen, F. Kun, K. F. Pal, D. W. Zheng, and K. N. Tu, “Aggregation kinetics and stability of structures formed by magnetic microspheres,” *Phys. Rev. E*, vol. 59, pp. R4758–R4761, May 1999.
- [78] H. B. Lavender, K. A. Iyer, and S. J. Singer, “Global orientational order in model polar clusters,” *J. Chem. Phys.*, vol. 101, pp. 7856–7867, November 1994.
- [79] N. Vandewalle and S. Dorbolo, “Magnetic ghosts and monopoles,” *New J. Phys.*, vol. 16, p. 013050, January 2014.
- [80] S. L. Tripp, R. E. Dunin-Borkowski, and A. Wei, “Flux closure in self-assembled cobalt nanoparticle rings,” *Angew Chem Int Ed Engl*, vol. 42, pp. 5591–3, Nov 2003.
- [81] T. Yanagida, M. Nakase, K. Nishiyama, and F. Oosawa, “Direct observation of motion of single f-actin filaments in the presence of myosin,” *Nature*, vol. 307, pp. 58–60, 01 1984.

- [82] F. Gittes, B. Mickey, J. Nettleton, and J. Howard, “Flexural rigidity of microtubules and actin-filaments measured from thermal fluctuations in shape,” *J. Cell Biol.*, vol. 120, pp. 923–934, February 1993.
- [83] A. Ott, M. Magnasco, A. Simon, and A. Libchaber, “Measurement of the persistence length of polymerized actin using fluorescence microscopy,” *Phys Rev E*, vol. 48, pp. R1642–R1645, Sep 1993.
- [84] M. M. A. E. Claessens, M. Bathe, E. Frey, and A. R. Bausch, “Actin-binding proteins sensitively mediate f-actin bundle stiffness,” *Nat Mater*, vol. 5, pp. 748–53, Sep 2006.
- [85] K. Sneppen and G. Zocchi, *Physics in molecular biology*. Cambridge, UK: Cambridge University Press, 2005.
- [86] K. Binder and D. W. Heermann, *Monte Carlo simulation in statistical physics: an introduction*, vol. 80. Berlin: Springer-Verlag, 1988.
- [87] D. Bertsimas, J. Tsitsiklis, *et al.*, “Simulated annealing,” *Statistical science*, vol. 8, no. 1, pp. 10–15, 1993.
- [88] E. Marinari and G. Parisi, “Simulated tempering: a new monte carlo scheme,” *EPL (Europhysics Letters)*, vol. 19, no. 6, p. 451, 1992.
- [89] B. Kiani, D. Faivre, and S. Klumpp, “Elastic properties of magnetosome chains,” *New J. Phys.*, vol. 17, April 2015.
- [90] L. Chang, B. D. Rainford, J. R. Stewart, C. Ritter, A. P. Roberts, Y. Tang, and Q. Chen, “Magnetic structure of greigite (Fe<sub>3</sub>S<sub>4</sub>) probed by neutron powder diffraction and polarized neutron diffraction,” *Journal of Geophysical Research: Solid Earth*, vol. 114, 2009.
- [91] C. Kittel, *Introduction to solid state physics*. Wiley, 1986.

- [92] Baselgia, Warden, Waldner, Hutton, Drumheller, He, Wigen, and Marysko, “Derivation of the resonance frequency from the free energy of ferromagnets,” *Phys Rev B Condens Matter*, vol. 38, pp. 2237–2242, Aug 1988.
- [93] M. Ulmeanu, C. Antoniak, U. Wiedwald, M. Farle, Z. Frait, and S. Sun, “Composition-dependent ratio of orbital-to-spin magnetic moment in structurally disordered fexpt1-x nanoparticles,” *Phys. Rev. B*, vol. 69, February 2004.
- [94] H. Fischer, G. Mastrogiacomo, J. F. Loeffler, R. J. Warthmann, P. G. Weidler, and A. U. Gehring, “Ferromagnetic resonance and magnetic characteristics of intact magnetosome chains in magnetospirillum gryphiswaldense,” *Earth Planet. Sci. Lett.*, vol. 270, pp. 200–208, June 2008.
- [95] R. Egli, A. P. Chen, M. Winklhofer, K. P. Kodama, and C.-S. Horng, “Detection of noninteracting single domain particles using first-order reversal curve diagrams,” *Geochem. Geophys. Geosyst.*, vol. 11, January 2010.
- [96] R. E. Kopp, B. P. Weiss, A. C. Maloof, H. Vali, C. Z. Nash, and J. L. Kirschvink, “Chains, clumps, and strings: Magnetofossil taphonomy with ferromagnetic resonance spectroscopy,” *Earth Planet. Sci. Lett.*, vol. 247, no. 1-2, pp. 10–25, 2006.
- [97] R. E. Kopp, C. Z. Nash, A. Kobayashi, B. P. Weiss, D. A. Bazylinski, and J. L. Kirschvink, “Ferromagnetic resonance spectroscopy for assessment of magnetic anisotropy and magnetostatic interactions: A case study of mutant magnetotactic bacteria,” *J. Geophys. Res.-Solid Earth*, vol. 111, no. B12, 2006.
- [98] B. P. Weiss, S. S. Kim, J. L. Kirschvink, R. E. Kopp, M. Sankaran, A. Kobayashi, and A. Komeili, “Ferromagnetic resonance and low-temperature magnetic tests for biogenic magnetite,” *Earth Planet. Sci. Lett.*, vol. 224, no. 1-2, pp. 73–89, 2004.

- [99] M. Charilaou, M. Winklhofer, and A. U. Gehring, “Simulation of ferromagnetic resonance spectra of linear chains of magnetite nanocrystals,” *J. Appl. Phys.*, vol. 109, 2011.
- [100] A. Terwey, “Magnetic characterization of organically formed magnetite nanoparticle arrangements in magnetospirillum gryphiswaldense,” Master’s thesis, University Duisburg-Essen, 2015.
- [101] P. S. S. K. D. F. Sara Ghaisari, Michael Winklhofer, “Unraveling magnetosome organization in magnetotactic bacteria with ferromagnetic resonance spectroscopy.” Manuscript submitted for publication, 2016.
- [102] L. R. Bichford, “Ferromagnetic resonance absorption in magnetite single crystals,” *Phys Rev*, vol. 78, 1950.
- [103] A. Scheffel and D. Schüler, “The acidic repetitive domain of the magnetospirillum gryphiswaldense mamj protein displays hypervariability but is not required for magnetosome chain assembly,” *J Bacteriol*, vol. 189, pp. 6437–46, Sep 2007.
- [104] M. Charilaou, J. Kind, I. Garcia-Rubio, D. Schueler, and A. U. Gehring, “Magnetic anisotropy of non-interacting collinear nanocrystal-chains,” *Appl. Phys. Lett.*, vol. 104, 2014.
- [105] P. G. De Gennes and P. A. Pincus, “Pair correlations in a ferromagnetic colloid,” *Physik der kondensierten Materie*, vol. 11, no. 3, pp. 189–198, 1970.
- [106] T. Tlustý and S. A. Safran, “Defect-induced phase separation in dipolar fluids,” *Science*, vol. 290, pp. 1328–1331, November 2000.
- [107] J. Yuan, Y. Xu, and A. H. E. Müller, “One-dimensional magnetic inorganic-organic hybrid nanomaterials,” *Chem Soc Rev*, vol. 40, pp. 640–55, Feb 2011.
- [108] R. Dreyfus, J. Baudry, M. L. Roper, M. Fermigier, H. A. Stone, and J. Bibette, “Microscopic artificial swimmers,” *Nature*, vol. 437, pp. 862–5, Oct 2005.



- [109] N. Nakamura, K. Hashimoto, and T. Matsunaga, “Immunoassay method for the determination of immunoglobulin g using bacterial magnetic particles,” *Anal Chem*, vol. 63, pp. 268–72, Feb 1991.
- [110] M. Kuhara, H. Takeyama, T. Tanaka, and T. Matsunaga, “Magnetic cell separation using antibody binding with protein a expressed on bacterial magnetic particles,” *Anal. Chem.*, vol. 76, pp. 6207–6213, November 2004.
- [111] T. Matsunaga, Y. Higashi, and N. Tsujimura, “Drug delivery by magnetoliposomes containing bacterial magnetic particles,” *Cell Eng*, vol. 2, 1997.
- [112] C. L. Hall, D. Vella, and A. Goriely, “The mechanics of a chain or ring of spherical magnets,” *SIAM J. Appl. Math.*, vol. 73, no. 6, pp. 2029–2054, 2013.



# List of Figures

1.1	Aquaspirillum magnetotacticum cell with one single chain of magnetite particles and one single flagellum at each pole of the cell. Scale bar represent $1\mu m$ . Drawn after fig. 1(b) of [6]. . . . .	3
1.2	General features of selected magnetotactic bacteria. Each species is designated with an image in front of its name. . . . .	5
1.3	<i>Magnetococcus marinus</i> MC-1 with a single chain of magnetite particles and two tufts of flagella (bilophotrichous). Scale bar represents $0.5\mu m$ . Drawn after fig. 1(b) of [13]. . . . .	6
1.4	<i>Magnetobacterium bavaricum</i> with several parallel chains of magnetite particles and one polar tuft of flagella. Scale bar represent $1\mu m$ . Drawn after fig. 1(b) of [20]. . . . .	7
1.5	A bar magnet is placed close to the drop. The bacteria swim towards the magnet and accumulate at the edge of the drop. . . . .	8
1.6	Schematic drawing of how polar magneto-aerotaxis directs cells to the preferred oxygen concentration at the oxic-anoxic interface (OATZ). NH, Northern hemisphere; SH, Southern hemisphere; $B_{geo}$ , geomagnetic field. . . . .	9
2.1	a) Sketch of the magnetosome chain in magnetotactic bacterium: magnetic nanoparticles (gray circles) are attached to a cytoskeletal filament (green line), enveloped in membrane (red lines). b) Geometric parameters of magnetosome particles with radius $r$ and magnetic moment $\mathbf{m}$ . . . . .	17

2.2	Bent magnetosome chain: (a) Sketch of the geometry: The chain is bent onto a circle with radius $R$ and a corresponding bending angle $\varphi$ . The magnetic moments are oriented in an angle $\theta$ with respect to the line connecting neighboring magnetosomes. (b) In the equilibrium configuration, $\theta = -\varphi/2$ , i.e., the magnetic moments align tangentially on the bending circle. . . . .	19
2.3	Persistence length as a function of particle size: Values are calculated for a magnetosome chain of 20 spherical magnetite particles at minimal distances ( $\ell = 2r + d$ ) with or without an enclosing membrane. Squares are for the case with a membrane of thickness 5 nm ( $d = 10\text{nm}$ ), circles for the case without a membrane ( $d = 0$ ). . . . .	22
2.4	Magnetic energy of a chain as a function of the bending curvature given by the inverse of the ratio of the distance between nearest neighbors and the curvature radius ( $\ell/R$ ) or equivalently, the curvature angle $\varphi$ (normalized to the angle for the closed ring configuration). The larger circle at the highest curvature shown indicates the closed ring configuration. The dashed line indicates the harmonic approximation, the arrows marks the barrier between the linear and close-ring configuration. The results shown here are for a chain of 20 particles. . . . .	23
2.5	Linear and closed ring configurations of a chain of magnetic nanoparticles interacting only magnetically (no filament): (a) Sketch of the closed ring geometry. (b) Magnetic energy for the linear and the closed-ring configurations as functions of the number of particles. The closed ring configuration has lower energy for chains with four and more particles. . . . .	25

2.6	Bending of a magnetosome chain: (a) Magnetic and elastic bending energy as a function of the curvature $\ell/R$ for different values of the filament bending stiffness $\kappa_{\text{fil}}$ . The uppermost curve is for the critical value of $\kappa_{\text{fil}}$ , for which the linear and the closed–ring configuration have the same energy. (b) State diagram indicating the lowest–energy configuration as a function of the ratio of the elastic and magnetic bending rigidities, $\kappa_{\text{fil}}/\kappa_{\text{magn}}$ , and the number of magnetic particles. (c) Height of the energy barrier separating the linear–chain and closed–ring configuration as a function of the ratio of the bending rigidities. The vertical red line indicates the critical bending rigidity, $\kappa_{\text{fil}}^*$ , above which the linear chain is the most stable configuration. . . . .	28
2.7	Schematic picture for possible structures of magnetosome filaments: a) A single long filament extending from one cell pole to the other, b) a bundle of long filaments, c) a long bundle consisting of shorter filaments.	29
3.1	Local minimum structures observed in the Monte Carlo computer simulation of 20 randomly distributed magnetosome particles with no binding energy to the filament (a–e). Observed structures include chains (b, c), rings (a, b and d) and handle (e). In the presence of the binding energy to the filament, particles form semi–linear structures along the filament (f–h). . . . .	37
3.2	Fraction of configurations observed in the Monte Carlo computer simulations in the absence and presence of different values of the binding potential to the filament. In each case configurations were extracted from 100 runs of the simulations. Simulations classified as Other structures include open rings (observed in the case of $E_b = 0k_B T$ ) and a single ring accompanied by two chains (in the case of $E_b = 4.0k_B T$ ). .	38

3.3	Final configuration of magnetosome particles for different values of the binding energy to the filament and the external magnetic field strength. The external field is fixed to an angle $90^\circ$ , relative to the direction of the filament. The color coding indicates the magnetosome configuration quantified by the number of chains (average of 5 simulations, rounded to integers). The number in each circle indicates the number of particles bound to the filament (also averaged over 5 simulations and rounded to integers.) . . . . .	39
3.4	Schematic view of a magnetosome particle (shown in blue frame) connected to the filament in the presence of dipole–dipole interaction and an external magnetic field with the angle $\theta_B$ relative to the direction of the filament. At the threshold angle of $\theta_B \simeq 27^\circ$ , the binding energy rises higher than the elastic energy and therefore the binding to the filament is not anymore an advantage. . . . .	41
3.5	Response of the chain magnetisation to a rotation of the external field: $a_1$ , $b_1$ and $c_1$ show the change in the orientation of the chain magnetic moment in different angles and strengths of the external field. How the average number of magnetosome particles bound to the filament changes during the rupture is presented for each field strength in $a_2$ , $b_2$ and $c_2$ . In each plot, different colours represent 10 trajectories extracted from Monte Carlo simulations. . . . .	43
3.6	(a) The external field critical angles for chain rupture: As field strength increases, the magnetosome chain ruptures at lower values of the external field angle. (b) Chain magnetic moment angle at first and second critical angles of the external field as a function of the field strength. The figure shows the independence of this angle from the field strength.	44
3.7	Figure shows the change in the orientation of the magnetic moment of a magnetosome chain with $N = 20$ greigite particles in different angles of an external magnetic field of 50mT. . . . .	45

3.8	Behaviour of the dipole–dipole interactions energy between magnetosome particles (a), the external magnetic field–dipole interaction energy (b) interaction energies of magnetosome particles, the binding (c) and elastic energies (d) of the linkers of the particles to the filament in the magnetosome chain under an external magnetic field of 50mT for different angles of the external magnetic field relative to the direction of the filament. . . . .	46
3.9	Plots represent the change in the behaviour of the magnetosome chain during the disruption with an external magnetic field, from 0 to $90 \times 10^{+7}$ MCS, and after elimination of the external field, from $90 \times 10^{+7}$ MCS to $180 \times 10^{+7}$ MCS. While the magnetosome chain regains its linear structure on the filament, the magnetic moments of the particles align to the direction of the filament (a) and particles rebind to the filament therefore the number of particles bound to the filament increases again (b) and the binding energy falls to its minimum values (c). Decrease in the elastic energy to the initial value (d) indicates that the linkers of the particles to the filaments reform with their relaxed length. MCS refers to Monte Carlo Steps. . . . .	47
3.10	The plot depicts the recovery of the magnetosome chain after treatment with an external field aligned with the direction of the filament. MCS refers to Monte Carlo Steps. . . . .	48
4.1	Schematic view of (a) the magnetosome chain and (b) the cartesian coordinate system. . . . .	52
4.2	Map of resonance field for $0^\circ < \theta_{B_{ext}} < 90^\circ$ and $0^\circ < \varphi_{B_{ext}} < 360^\circ$ for a magnetosome particle in the middle of a magnetosome chain with $N = 20$ particles. $\theta_{B_{ext}}$ and $\varphi_{B_{ext}}$ are polar and azimuthal angles of the applied field relative to the direction of the chain, z–axis. The resonance field shows an uniaxial symmetry around the z–axis. . . .	57

- 4.3 Calculated FMR spectra for magnetosome chains: (a, c) show the absorption spectra. (b, d) Derivatives of the absorption spectra as measured experimentally. Upper and lower plots show the same spectra but with different linewidth. Y axis in both plots has an arbitrary unit. 59
- 4.4 (a) The map of the resonance field for  $0^\circ < \theta_{B_{ext}} < 90^\circ$  and  $0^\circ < \varphi_{B_{ext}} < 360^\circ$  for a magnetosome particle with magnetocrystalline anisotropy. The map shows the formation of a three-fold symmetry after incorporating the magnetocrystalline anisotropy energy into the system. The plot present the data for the particle in the middle of a magnetosome chain with  $N = 20$  particles. (b, c) Applying the gaussian function, absorption peaks at  $B_{ext} = 380$  mT and at  $B_{ext} = 392$  mT are observed. 60
- 4.5 On top: (a) External magnetic field–dipole interactions energy, (b) dipole–dipole interactions energy and (c) magnetocrystalline anisotropy energy for a chain 20 magnetosome particles under an external field of 280 mT. On bottom: (d) External magnetic field–dipole interactions energy and (e) dipole–dipole interactions energy for a chain of 20 magnetosome particles without the magnetocrystalline anisotropy and under an external field of 280 mT. In the presence of the magnetocrystalline anisotropy, the uniaxiality observed in the energies converts into a three-fold symmetry. . . . . 61
- 4.6 On top: Resonance field as a function of the azimuthal angle  $\varphi_{B_{ext}}$  with (a) and without (b) the magnetocrystalline anisotropy. On bottom: Resonance field at different polar angles with (c) and without (d) magnetocrystalline anisotropy. Due to numerical limitations, Resonance field values at  $0^\circ$  and  $180^\circ$  are not calculated. . . . . 63



4.7	FMR spectra of a magnetosome chain with gaps in the arrangement of magnetosome particles: (a) Map of the resonance field for a magnetosome particle in a chain with gaps between particles. The corresponding arrangement is shown in (b). (c, d) Resonance spectra. For Comparison, the resonance spectra for a chain without gaps is also shown. . . . .	64
4.8	(a) The map of the resonance field for a random magnetosome particle in a cluster of $N = 20$ magnetosome particles with magnetocrystalline anisotropy. (b) Resonance spectra for 20 magnetosome particles in a cluster configuration. The resonance occurs at $B_{ext} = 376$ and $B_{ext} = 384$ mT for the cluster configuration of magnetosome particle. . . . .	66
A.1	Bending rigidity (left) and persistence length (right) of the magnetosome chain as a function of $\frac{l}{R}$ for temperatures 30°K, 300°K and 3000°K. The dashed lines demonstrate the values of the bending rigidity and the persistence length at $T=0^\circ$ derived from analytical calculations in chapter 2. . . . .	80
B.1	The torque exerted by the external field pulls the linker of the particle to the filament with relaxed length $l_0$ to the length $l$ . . . . .	81
B.2	Figure (a) shows the orientation of the chain magnetic moment in different angles of the external field. Figure (b) presents the change in the average number of magnetosome particles bound to the filament during the application of the external. In each plot, different colours represent 10 trajectories extracted from Monte Carlo simulations. . . . .	82

B.3	The external field of 35mT disorients the dipoles from their initial linear orientation along the filament and therefore the dipole–dipole interaction increases. Changing the angle of the external field to higher angles increases the elasticity of the attached particles. As the strength of the external field is below the threshold needed to rotate the dipoles to the critical point of rupture where dipoles begin to repel each other, in contrast to the case of higher external field strengths, the chain is not disrupted and dipole–dipole interactions, the external field–dipole interactions and the elastic energy of the linkers do not decrease back to the lower values. . . . .	83
B.4	Plot presents the change in the force between two dipoles from repulsion to attraction with increasing the angles of the dipoles relative to the direction of the vector connecting them. . . . .	84
B.5	Due to feeble dipole–dipole interactions, early after the critical point, dipoles align with the external field (a), the elasticity of linkers to the filament increases and as a result they break and the number of bound particles (b) drops. . . . .	85
B.6	The behaviour of dipole–dipole interactions (a), external magnetic field–dipole interactions (b), binding (c) and elastic (d) energies for a chain with $N = 20$ greigite particles in different angles of the external magnetic field of $B = 50\text{mT}$ relative to the direction of the filament. . . . .	86
C.1	Resonance spectrum for different orientation of the external field, relative to the direction of the magnetosome chain, emerges at different field strength. . . . .	89

C.2	The maps of the resonance field for the first five magnetosome particles at one end of a magnetosome chain of $N = 20$ particles. The dissimilarity between the resonance field of the first particle and the rest of the particles owing to weaker dipole–dipole interactions is already noticeable between the map of two first particles. As the dipole–dipole interactions are fast decaying, there is no distinct difference between the behaviour of the resonance field of the particles in the middle. In other words, the dominant role in dipole–dipole interactions is played by two first neighbours, for more detail see chapter 2. . . . .	91
-----	--	----



## Acknowledgements

I would like to express my sincere gratitude to my family, friends and colleagues for their support throughout my PhD.

I am grateful to my supervisor, Prof. Dr Stefan Klumpp, for the opportunity to work with him, for his scientific accompaniment, for his patience and for the many possibilities that he opened up to me during my PhD. I learned a lot from him.

I would also like to thank Dr. Damien Faive at Max Planck Institute of Colloids and Interfaces, for always being welcoming and encouraging during the time I collaborated with his group.

Many thanks also to Aparna, Mathieu and Sara for all the fruitful discussions we have had over the past four years.

Last but not least, I am grateful to my parents, my sisters, Jan and Sourenna for their precious support. Sourenna, you walked me step by step through my PhD. Without your support, it would not have been possible.